

Worlds Next Door. IV. Mapping the Late Stages of Giant Planet Evolution with a Precise Dynamical Mass and Luminosity for ϵ Ind Ab

ANIKET SANGHI ^{1,*} WILLIAM THOMPSON ² JAMES MANG ^{3,*} JERRY W. XUAN ^{4,†} DIMITRI MAWET ^{1,5}
JEAN-BAPTISTE RUFFIO ⁶ YAPENG ZHANG ^{1,†} JASON J. WANG ^{7,8} CAROLINE V. MORLEY ³ ERIC NIELSEN ⁹
WILLIAM ROBERSON ⁹ ELISABETH MATTHEWS ¹⁰ AARYNN L. CARTER ¹¹ IAN J. M. CROSSFIELD,¹²
MATHILDE MALIN ^{11,13} BJÖRN BENNEKE ⁴ ALEXIS BIDOT ¹¹ ANDRÁS GÁSPÁR ¹⁴ CARRIE HE,⁴
KATELYN HORSTMAN ¹ ALEXANDER MADUROWICZ ¹¹ CHRISTIAN MAROIS ^{2,15} REBECCA OPPENHEIMER ¹⁶ AND
MARSHALL PERRIN ¹¹

¹*Cahill Center for Astronomy and Astrophysics, California Institute of Technology, 1200 E. California Boulevard, MC 249-17, Pasadena, CA 91125, USA*

²*NRC Herzberg Astronomy and Astrophysics, 5071 West Saanich Road, Victoria, BC, V9E 2E7, Canada*

³*Department of Astronomy, University of Texas at Austin, Austin, TX 78712, USA*

⁴*Department of Earth, Planetary, and Space Sciences, University of California, Los Angeles, CA 90095, USA*

⁵*Jet Propulsion Laboratory, California Institute of Technology, Pasadena, CA 91109, USA*

⁶*Department of Astronomy & Astrophysics, University of California, San Diego, La Jolla, CA 92093, USA*

⁷*Center for Interdisciplinary Exploration and Research in Astrophysics (CIERA), Northwestern University, 1800 Sherman Avenue, Evanston, IL, 60201, USA*

⁸*Department of Physics and Astronomy, Northwestern University, 2145 Sheridan Road, Evanston, IL 60208, USA*

⁹*Department of Astronomy, New Mexico State University, 1320 Frenger Mall, Las Cruces, NM 88003, USA*

¹⁰*Max-Planck-Institut für Astronomie, Königstuhl 17, D-69117 Heidelberg, Germany*

¹¹*Space Telescope Science Institute, 3700 San Martin Drive, Baltimore, MD 21218, USA*

¹²*Department of Physics and Astronomy, University of Kansas, Lawrence, KS, USA*

¹³*Department of Physics & Astronomy, Johns Hopkins University, 3400 N. Charles Street, Baltimore, MD 21218, USA*

¹⁴*Steward Observatory, University of Arizona, Tucson, AZ 85721, USA*

¹⁵*Department of Physics and Astronomy, University of Victoria, 3800 Finnerty Road, Elliot Building, Victoria, BC V8P 5C2, Canada*

¹⁶*American Museum of Natural History, New York, NY, USA*

ABSTRACT

We present new JWST/NIRCam 4–5 μm (F410M, F430M) and JWST/MIRI 18–25 μm (F1800W, F2100W, F2550W) imaging detections of the nearby (3.6 pc) cold (275 K) gas giant exoplanet ϵ Ind Ab. The F2550W detection of ϵ Ind Ab constitutes the longest wavelength image of an exoplanet acquired to date. Combining three decades of radial velocity monitoring, Gaia-Hipparcos absolute astrometry, and relative astrometry from direct imaging (including the new NIRCam astrometry), we conduct a comprehensive re-analysis of ϵ Ind Ab’s orbit and obtain a dynamical mass $M_{\text{Ab}} = 6.5_{-0.6}^{+0.7} M_{\text{Jup}}$. Using ϵ Ind Ab’s NIRCam and MIRI photometry, we assemble the first 4–25 μm spectral energy distribution (SED) of a cold gas giant outside the Solar System. The NIRCam photometry supports a metal-enriched atmosphere for ϵ Ind Ab based on analysis with atmospheric model grids, consistent with predictions from the giant planet mass-metallicity relation. While the current data do not provide definitive evidence for or against the presence of water ice clouds, we tentatively find that the H₂O vapor absorption-dominated F2550W photometry is systematically brighter ($> 1\sigma$, but $< 2\sigma$) than predictions from cloud-free/rainout chemistry models and better explained by a cloudy model. We calculate a bolometric luminosity of $\log L_{\text{bol}}/L_{\odot} = -7.23 \pm 0.03$ dex by directly integrating ϵ Ind Ab’s SED. Combining this with the planet’s dynamical mass and age (3.5 ± 1.0 Gyr), we demonstrate excellent agreement with evolutionary model predictions in a new regime of low luminosities, low masses, and old ages. Our results establish ϵ Ind Ab as a benchmark system for planetary evolution studies and set the stage for the detailed atmospheric characterization of this frigid extrasolar world.

Corresponding author: Aniket Sanghi

Email: asanghi@caltech.edu

Keywords: James Webb Space Telescope (2291) — Coronagraphic imaging (313) — Extrasolar gaseous giant planets (509) — Exoplanet Atmospheres (487) — Exoplanet evolution (491)

1. INTRODUCTION

The direct detection and characterization of extrasolar Jupiter-analog gas giants is central to developing our understanding of their formation and evolution (e.g., N. Madhusudhan 2019; M. Ikoma & H. Kobayashi 2025; I. A. G. Snellen 2025), placing the Solar System in the broader exoplanetary context through comparative planetology studies (e.g., C. Gelino & M. Marley 2000; H. Ge et al. 2019; D. J. Coulter et al. 2022), and investigating their influence on the formation and long-term habitability of Earth-like worlds (e.g., M. Noble et al. 2002; S. N. Raymond 2006; N. Georgakarakos et al. 2018; K. I. Antoniadou & A.-S. Libert 2018; Z. Kong et al. 2024). Indeed, over the past two decades, the technique of high-contrast imaging has successfully combined high-order adaptive optics systems, starlight suppression technologies (e.g., small inner-working-angle coronagraphs), and innovative post-processing strategies to assemble a remarkable sample of young (< 1 Gyr) gas giants for detailed atmospheric characterization studies (B. P. Bowler 2016; T. Currie et al. 2023).

Prior to the launch of JWST, nearly all direct imaging detections were made at near-infrared wavelengths (*JHK* and *L* bands, $\approx 1\text{--}4\ \mu\text{m}$), where a significant fraction of the bolometric flux of young, hot (~ 1000 K) gas giants is emitted. However, mature gas giants (\sim Gyr ages) are significantly colder ($\lesssim 300$ K) and exhibit orders of magnitude more favorable contrast in the mid-infrared wavelengths ($> 10\ \mu\text{m}$), from a combination of being near the peak of the planet’s thermal emission but in the Rayleigh-Jeans tail of the host star (e.g., D. S. Spiegel & A. Burrows 2012). These wavelengths are extremely challenging to access from the ground due to the rapidly increasing thermal background beyond $4\ \mu\text{m}$, though notable efforts were made with the VLT/NEAR experiment, which demonstrated the potential for detection of low mass planets in the *N* band ($10\text{--}12.5\ \mu\text{m}$, M. Kasper et al. 2017, 2019; K. Wagner et al. 2021; P. Pathak et al. 2021; G. Viswanath et al. 2021). Now, JWST’s unparalleled thermal infrared sensitivity ($4\text{--}25\ \mu\text{m}$, J. Rigby et al. 2023) has opened the doors to the direct detection of gas giants more similar in age and temperature to Jupiter and Saturn in our own Solar System (e.g., E. C. Matthews et al. 2024; C. Beichman et al. 2025; A. Sanghi et al. 2025; R. Bowens-Rubin et al. 2025; D. C. B. Gagliuffi et al. 2025; A. Sanghi et al. 2026). The nearest stars are the most favorable targets in this endeavor, since planet flux $f_p \propto d^{-2}$ and

the planet’s on-sky angular separation (for fixed physical separation) $\rho \propto d^{-1}$, where d is distance to the system.

At a distance of ~ 3.6 pc, ϵ Ind A (K5V, $0.78 M_{\odot}$, Table 1) is one of the nearest Sun-like stars to Earth and a Tier A target in the search for habitable Exo-Earths with NASA’s planned Habitable Worlds Observatory (E. Mamajek & K. Stapelfeldt 2024; L. D. Feinberg et al. 2026). The star’s age is estimated to be 3.5 ± 1.0 Gyr, similar to our Solar System’s age of ~ 4.6 Gyr, based on activity indicators (M. Chen et al. 2022). Early imaging discovered a co-moving brown dwarf companion ϵ Ind B at a separation of ~ 1460 au (R.-D. Scholz et al. 2003). Follow-up high angular resolution near-infrared imaging with VLT NAOS/CONICA revealed that the companion was in fact a binary, consisting of the T1 and T6 dwarfs ϵ Ind Ba and ϵ Ind Bb, respectively (M. J. McCaughrean et al. 2004). Long term radial velocity (RV) monitoring of the system identified a trend that could not be explained by the brown dwarf binary or secular acceleration of the system (M. Endl et al. 2002; M. Zechmeister et al. 2013), thereby pointing to the presence of an additional companion in the system. The combination of RV and Hipparcos-Gaia absolute astrometry suggested that the additional companion was a cold Jupiter, ϵ Ind Ab ($\sim 3 M_{\text{Jup}}$, F. Feng et al. 2019, 2023). Subsequent JWST/MIRI coronagraphic observations at $10.65\ \mu\text{m}$ and $15.5\ \mu\text{m}$ (and reprocessing of archival VLT/NEAR observations) provided the first direct detection of ϵ Ind Ab, but found it at a location inconsistent with the RV and astrometry orbit prediction (E. C. Matthews et al. 2024). The inconsistency was attributed to biases from modeling RVs covering a limited time span and the dynamical mass was revised to $\sim 7 M_{\text{Jup}}$ (F. Feng et al. 2025). The mid-infrared photometry indicate that ϵ Ind Ab has an effective temperature ~ 275 K, making it one of the coldest exoplanets imaged to date. Additionally, E. C. Matthews et al. (2024) found that the non-detection of the planet between $3.5\text{--}5.0\ \mu\text{m}$ in previous ground-based imaging suggested an unknown source of flux suppression, possibly from high metallicity and/or carbon-to-oxygen ratio. ϵ Ind Ab’s proximity, wide angular separation ($3''\text{--}4''$), and measured dynamical mass make it a prime benchmark target for detailed atmospheric characterization with JWST.

In this paper, we present new JWST/NIRCam $4\text{--}5\ \mu\text{m}$ (F410M, F430M) and JWST/MIRI $18\text{--}25\ \mu\text{m}$ (F1800W, F2100W, F2550W) imaging detections of ϵ Ind Ab, which, together, enable us to assemble the first $4\text{--}25\ \mu\text{m}$ spectral energy distribution of a cold gas giant exoplanet. The paper is organized as follows. Section 2 summarizes the observational sequences executed with JWST, the data reduction, and procedures to estimate companion astrometry and photometry. Section 3 re-

* NSF Graduate Research Fellow

† 51 Pegasi b Fellow

Table 1. Stellar Properties of ϵ Ind A

Property	Value	Ref.
$\alpha_{2016.0}$ ($^{\circ}$)	330.8724 ± 0.0687	1
$\delta_{2016.0}$ ($^{\circ}$)	-56.7973 ± 0.0655	1
$\mu_{\alpha^*}^a$ (mas yr $^{-1}$)	3966.661 ± 0.086	1
μ_{δ} (mas yr $^{-1}$)	-2536.192 ± 0.092	1
ϖ (mas)	274.8431 ± 0.0956	1
Distance (pc)	$3.648^{+0.022}_{-0.009}$	2
SpT	K5V	3
Mass (M_{\odot})	0.782 ± 0.023	4
Radius (R_{\odot})	0.713 ± 0.006	2, 4, 5
Age (Gyr)	$3.48^{+0.78}_{-1.03}$	6
T_{eff} (K)	4700 ± 65	4
[Fe/H] (dex)	-0.17 ± 0.03	4
$v \sin i$ (km/s)	2.0	5
$\log(R'_{HK})$ (dex)	-4.72	7
P_{rot} (d)	$-35.732^{+0.006}_{-0.003}$	8
RUWE _{DR3}	1.148	1

^aProper motion in R.A. includes a factor of $\cos \delta$.

References—(1) Gaia Collaboration et al. (2023); (2) O. L. Creevey et al. (2023); (3) C. A. O. Torres et al. (2006); (4) M. S. Lundkvist et al. (2024); (5) A. D. Rains et al. (2020); (6) M. Chen et al. (2022); (7) G. Pace (2013); (8) F. Feng et al. (2019).

considers the orbit of ϵ Ind Ab with the addition of the new high-precision NIRCcam astrometry and revises the planet’s dynamical mass. Section 4 compares ϵ Ind Ab’s SED to that of Y dwarf WISE 0855, presents an initial reconnaissance of ϵ Ind Ab’s atmospheric properties (metallicity, water clouds, disequilibrium chemistry), and calculates the planet’s bolometric luminosity. Section 5 conducts comprehensive consistency tests between ϵ Ind Ab’s measured fundamental properties and predictions from evolutionary models. Finally, Section 6 lists our conclusions. Appendices A, B, and C present the MIRI reference library, lessons learned about RV + HGCA modeling from ϵ Ind Ab, and the posteriors for all orbit models considered in this work, respectively.

2. OBSERVATIONS AND DATA REDUCTION

2.1. JWST/NIRCcam Imaging

2.1.1. Executed Sequences

We obtained F200W (1.755–2.227 μm), F410M (3.865–4.301 μm), and F430M (4.167–4.398 μm) JWST/NIRCcam imaging of ϵ Ind A on UT 2025 August 28 as part of Cycle 4 program GO 8714 (PI: J. Xuan, Co-PI: A. Sanghi, J. B. Ruffio, Y. Zhang). We chose two-roll angular differential imaging (ADI: M. C. Liu 2004; C. Marois et al. 2006) to detect the giant planet ϵ Ind Ab given its wide separation ($>3''$). No reference stars were observed. The observations were

carried out between UT 2025 August 28 03:56:22 and 06:10:59 in a non-interruptible sequence for a total of ≈ 2.2 hours (including observatory overheads) simultaneously with the F200W/F410M filter combination followed by the F200W/F430M filter combination, and using the MASK430R coronagraph at telescope V3 position angles 2.54° and 13.49° ($\approx 11^{\circ}$ roll). We used the SHALLOW4 readout pattern with 10 groups per integration and 23 integrations per exposure for all observations. The total exposure time on ϵ Ind A is 80.4 minutes in F200W and 40.2 minutes in F410M and F430M across the two-roll sequence.

2.1.2. Data Processing

The uncalibrated Stage 0 (*uncal.fits) data products were acquired from the Barbara A. Mikulski Archive for Space Telescopes (MAST¹⁷) and processed with spaceKLIP (J. Kammerer et al. 2022; A. L. Carter et al. 2023; A. Carter et al. 2025), a community developed pipeline for high contrast imaging with JWST. spaceKLIP wraps the jwst pipeline (H. Bushouse et al. 2025) for basic data processing steps with modifications for coronagraphic imaging reduction. Data reduction via spaceKLIP for our observations implements best-practices discussed in various works (J. Kammerer et al. 2022; A. L. Carter et al. 2023; K. Franson et al. 2024; D. C. B. Gagliuffi et al. 2025) and, more specifically, closely follows D. C. B. Gagliuffi et al. (2025). We used spaceKLIP v2.1, via github commit #11df3a1, and jwst v1.19.1; the calibration files were from CRDS v12.1.11 and the jwst_1413.pmap CRDS context¹⁸. The data were fit “up the ramp” using the “Likely” algorithm described in (T. D. Brandt 2024a,b) and transformed from Stage 0 images into Stage 2 (*calints.fits) images, using a jump threshold of 4 and 4 pseudo-reference pixels on all sides of the subarrays. The $1/f$ noise was mitigated using a median filter computed along each column. We skipped dark current subtraction (A. L. Carter et al. 2023). Pixels flagged by the jwst pipeline as well as 5σ outliers detected using sigma clipping were replaced with a 2-dimensional interpolation based on a 9-pixel kernel. We also identified additional pixels affected by cosmic rays by flagging pixels with significant temporal flux variations across integrations and replaced them by their temporal median. Subsequently, the images were blurred above the Nyquist sampling criterion, using a Gaussian with a FWHM of 2.55 for the F410M/LW detector, 2.30 for the F430M/LW detector, and 2.78 for the F200W/SW detector. These values ensure that sharp features in the data do not create artifacts when Fourier shifts are applied to the undersampled images. The position of the star behind the coronagraph was estimated

¹⁷ The data described here may be obtained from the MAST archive at [10.17909/nqx2-yw28](https://archive.stsci.edu/mast).

¹⁸ <https://jwst-crds.stsci.edu/>

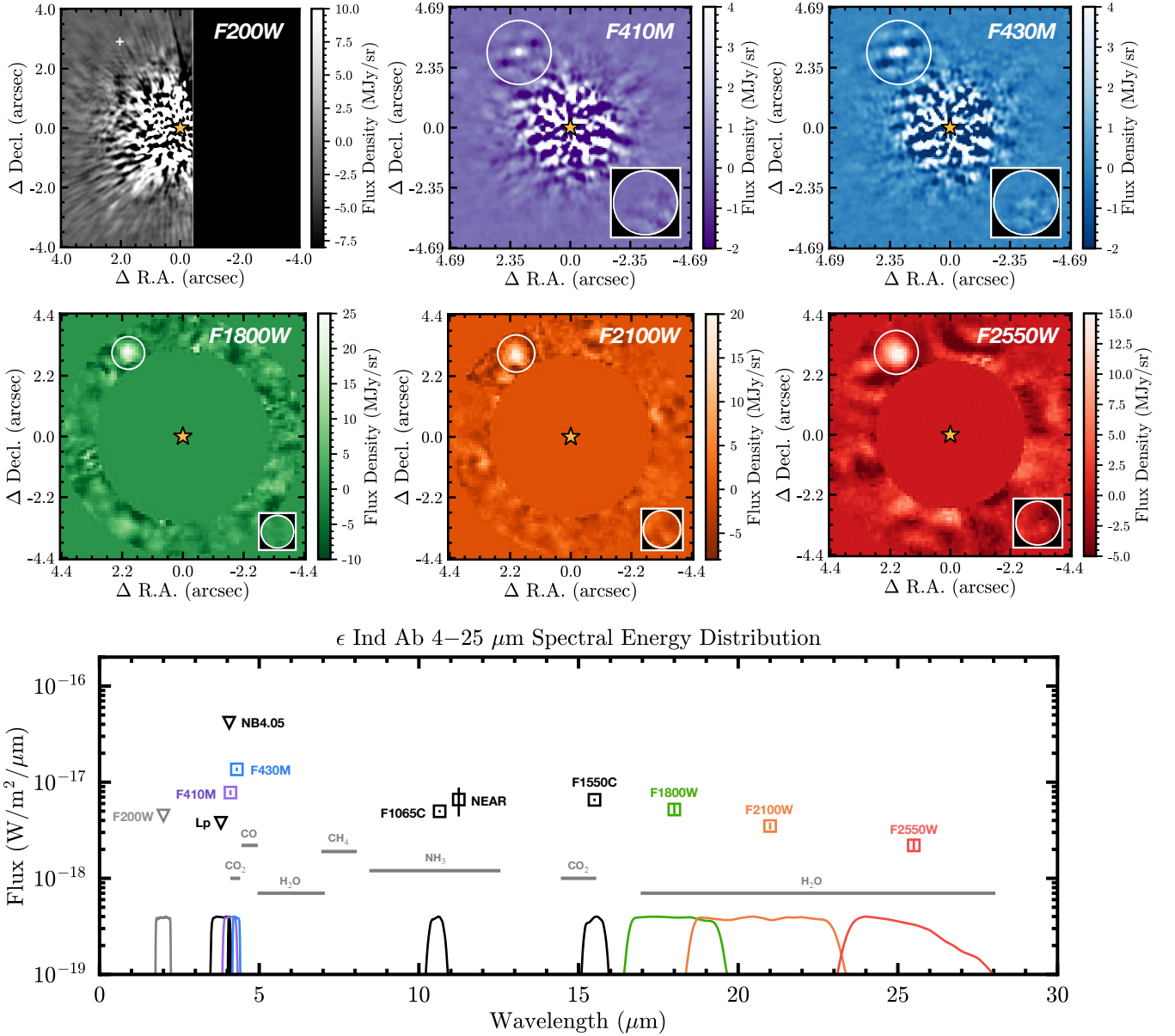


Figure 1. Gallery of PSF-subtracted images centered on ϵ Ind A in NIRCcam coronagraphic (top row) and MIRI non-coronagraphic (center row) imaging filters. All images are oriented North up and East left. Exoplanet ϵ Ind Ab is detected in all filters except F200W (expected location marked with a ‘+’). An inset image (bottom right corner) shows the residuals in the aperture centered on ϵ Ind Ab after the best-fit planet forward model is subtracted. The aperture encompasses the six-lobed structure of the planet PSF in the NIRCcam images and has a radius = 1 FWHM in the MIRI images. The F2550W image of ϵ Ind Ab is the longest wavelength image of an exoplanet taken to date. The bottom panel shows the complete 4–25 μm spectral energy distribution of ϵ Ind Ab. Boxes with error bars represent the measured photometry and inverted triangles represent upper limits, with the filter profiles plotted below (no filter profile available for VLT/NEAR). Solid gray horizontal lines mark the dominant opacity source in the corresponding wavelength region.

by fitting a model coronagraphic point spread function (PSF) from `webbpsf_ext` to the first science integration. All subsequent images were shifted by this initial offset. Images were cross-correlated to the first science integration, and these small shifts were applied to each integration to center the entire observing sequence to the first science integration. The position of ϵ Ind A behind the mask differed by ≈ 18 mas between the two rolls.

We carry out PSF subtraction with `spaceKLIP`, which uses the Karhunen-Loève Image Projection (KLIP: R. Soummer et al. 2012) algorithm implemented in `pyKLIP` (J. J. Wang et al. 2015) to model and subtract the host star PSF. Using `annulus=1`, `subsections=1`, and `numbasis=1` and comparing the companion contrast to the annular contrast, ϵ Ind Ab is detected at signal-to-noise ratios (S/Ns) of 17.9 and 25.4 in F410M and F430M (Figure 1), respectively. The planet is not recovered in F200W (Figure 1). Besides a known background source in the South-East direction at $\approx 11''$ separation (also seen in Spitzer images, E. C. Matthews et al. 2024), no other significant sources are detected in the full-frame images.

2.1.3. Astrometry and Photometry

To measure the astrometry and photometry of ϵ Ind Ab, we use the KLIP forward modeling (KLIP-FM: L. Pueyo 2016) framework implemented in `spaceKLIP` and `pyKLIP`. This approach accounts for measurement biases introduced in the primary subtraction procedures. A flexible forward model is generated and then fit to a given source in a post-processed image within a Bayesian framework (J. J. Wang et al. 2016). We employ the `emcee` affine-invariant Markov Chain Monte Carlo (MCMC) ensemble sampler (D. Foreman-Mackey et al. 2013) to simultaneously fit the planet separation, position angle, and flux. The PSF model is produced by `stpsf` (M. D. Perrin et al. 2012, 2014). A total of 50 walkers over 5×10^5 total steps (10000 per walker) are used to sample the posteriors of the three model parameters. We discard the first 5000 steps of each chain as burn-in. To account for correlated speckle noise, we model the noise distribution via a Gaussian process with a Matérn ($\nu = 3/2$) kernel (J. J. Wang et al. 2016). The measurements in detector units are transformed into physical units accounting for coronagraph transmission, filter zero points, and system distance.

The astrometric and photometric uncertainties are computed as the standard deviation of the MCMC chains. Additionally, the adopted uncertainties incorporate a systematic uncertainty of 0.05 pixel on the star-behind-mask position along each axis (for astrometry, J. H. Girard et al. 2024) and 0.01 mag on the stellar magnitude (for photometry). The stellar magnitude in all filters is estimated from stellar spectra drawn from the posteriors obtained by E. C. Matthews et al. (2024, see their Extended Data Fig. 7 for the best-fit spectrum) after fitting ground- and space-based photometry

of ϵ Ind A. The resulting planet astrometry and photometry are shown in Table 2.

We measure the 5σ upper limit in F200W through PSF injection-recovery. Synthetic sources generated with `stpsf` are injected at the same separation as ϵ Ind Ab across seven position angles (75° to 165° in steps of 15°). The S/N of each injected source is then measured by comparing contrast at the injected location to annular contrast, masking the position of ϵ Ind Ab and the region outside the detector field-of-view (FOV; the star is offset in the short-wavelength channel, see Figure 1). The injected flux is adjusted to produce a S/N of 5σ . The mean injected flux across all position angles is taken as the 5σ upper limit (Table 2).

2.2. JWST/MIRI Imaging

2.2.1. Executed Sequences and Archival Data

We obtained F1800W (16.519–19.502 μm), F2100W (18.477–23.159 μm), and F2550W (23.301–26.733 μm) JWST/MIRI imaging of ϵ Ind A on UT 2025 September 4 as part of Cycle 4 program GO 8714 (PI: J. Xuan, Co-PI(s): A. Sanghi, J. B. Ruffio, Y. Zhang). The observations were conducted in the MIRI MRS simultaneous imaging mode¹⁹ during dedicated background observations for spectroscopy of ϵ Ind Ab (Obs #5). This mode enables simultaneous data collection by both the MIRI imager and medium resolution spectrometer. The observations were carried out between UT 2025 September 4 04:00:53 and 07:26:05 for a total of ≈ 3.5 hours (including observatory overheads) sequentially in the F1800W, F2100W, and F2550W filters. A 4-point cycling dither pattern was employed for each filter to enable accurate background subtraction (the choice of the dither pattern was optimized for the MRS dedicated backgrounds). We used the FULL subarray ($74'' \times 113''$) and the FASTR1 readout pattern with 5 groups per integration (the minimum recommended) and 53 integrations per exposure for all observations. The choice of subarray is not optimal as it saturates the PSF core in each filter and the first Airy ring in F1800W. However, the smaller subarrays (SUB64, SUB128, SUB256, BRIGHTSKY) all result in the star and planet outside their FOV in at least one of the four dither positions. Given ϵ Ind Ab's wide angular separation ($\approx 3''.5$), the saturation was deemed acceptable. The total exposure time on ϵ Ind A is 58.9 minutes in each filter combining the four dither sequence.

Since the MIRI images of ϵ Ind A were acquired in MIRI MRS simultaneous imaging mode as a bonus at no additional cost, it was not possible to conduct dedicated reference star observations or obtain two roll angles. To enable PSF subtraction, we constructed a PSF library for each MIRI filter using publicly available archival MIRI imaging observations on MAST. This is motivated

¹⁹ <https://jwst-docs.stsci.edu/jwst-mid-infrared-instrument/miri-operations/miri-mrs-simultaneous-imaging>

Table 2. Astrometry and Photometry of ϵ Ind Ab

Instrument	Filter	Date	ρ ($''$)	θ ($^\circ$)	m_* (Vega mag)	Δ (Vega mag)	m_b (Vega mag)	Flux ($\text{Wm}^{-2}\mu\text{m}^{-1}$)	Flux (Jy)	Ref.
JWST/NIRCam	F200W	2025-08-28	2.187 ± 0.008	> 18.06	> 20.25	$< 4.5 \times 10^{-18}$	$< 6.0 \times 10^{-6}$	1
VLT/NaCo	L'	2018-10-12	2.142 ± 0.007	> 15.66	> 17.80	$< 3.78 \times 10^{-18}$	$< 1.83 \times 10^{-5}$	2, 3
		2018-10-26								
		2018-11-03								
		2018-11-04								
VLT/NaCo	NB4.05	2008-10-31	2.115 ± 0.008	> 12.78	> 14.89	$< 4.16 \times 10^{-17}$	$< 2.28 \times 10^{-4}$	2, 4
		2008-09-02								
JWST/NIRCam	F410M	2025-08-28	3.551 ± 0.003	34.97 ± 0.05	2.131 ± 0.007	14.58 ± 0.06	16.71 ± 0.06	$(7.8 \pm 0.5) \times 10^{-18}$	$(4.37 \pm 0.28) \times 10^{-5}$	1
JWST/NIRCam	F430M	2025-08-28	3.551 ± 0.003	34.97 ± 0.05	2.154 ± 0.008	13.75 ± 0.05	15.90 ± 0.05	$(1.36 \pm 0.06) \times 10^{-17}$	$(8.4 \pm 0.4) \times 10^{-5}$	1
VLT/VISIR	NEAR	2019-09-14	4.820 ± 0.164	42.5 ± 2.5	... ^a	... ^a	... ^a	$(6.6 \pm 2.2) \times 10^{-18}$	$(2.8 \pm 0.9) \times 10^{-4}$	2
		2019-09-15								
		2019-09-17								
JWST/MIRI	F1065C	2023-07-03	4.095 ± 0.010	38.17 ± 0.44	2.209 ± 0.008	10.93 ± 0.03	13.14 ± 0.03	$(4.98 \pm 0.15) \times 10^{-18}$	$(1.88 \pm 0.06) \times 10^{-4}$	2
JWST/MIRI	F1550C	2023-07-03	4.114 ± 0.010	37.39 ± 0.43	2.173 ± 0.007	9.04 ± 0.03	11.21 ± 0.03	$(6.55 \pm 0.20) \times 10^{-18}$	$(5.25 \pm 0.16) \times 10^{-4}$	2
JWST/MIRI	F1800W	2025-09-04	3.64 ± 0.09	34.4 ± 1.5	2.166 ± 0.008	8.64 ± 0.14	10.81 ± 0.14	$(5.2 \pm 0.7) \times 10^{-18}$	$(5.6 \pm 0.8) \times 10^{-4}$	1
JWST/MIRI	F2100W	2025-09-04	3.54 ± 0.07	33.6 ± 1.2	2.160 ± 0.008	8.47 ± 0.08	10.63 ± 0.08	$(3.5 \pm 0.3) \times 10^{-18}$	$(5.2 \pm 0.4) \times 10^{-4}$	1
JWST/MIRI	F2550W	2025-09-04	3.61 ± 0.12	32.6 ± 1.9	2.198 ± 0.008	8.05 ± 0.15	10.25 ± 0.15	$(2.2 \pm 0.3) \times 10^{-18}$	$(4.8 \pm 0.7) \times 10^{-4}$	1

References—(1) This Work; (2) E. C. Matthews et al. (2024); (3) G. Viswanath et al. (2021); (4) M. Janson et al. (2009).

^aFilter zero point not available.

NOTE— ρ is the planet's separation in arcseconds, θ is the planet's position angle measured in degrees East of North, m_* is the stellar apparent magnitude, Δ is the planet contrast with respect to the star, m_b is the planet's apparent magnitude.

by past success in both ground- and space-based high-contrast imaging applications (E. Choquet et al. 2016; W. J. Xuan et al. 2018; A. Sanghi et al. 2022; C. Xie et al. 2022; A. Sanghi et al. 2024). We selected observations where a bright PSF (not saturated to a greater extent than ϵ Ind A) could be extracted with a sufficient FOV (accounting for the dither pattern) to perform reference star differential imaging (RDI) out to $\approx 4''5$. No further selection cuts were applied due to the limited number of observations available. The full list of datasets used for the archival PSF reference library are presented in Appendix A.

2.2.2. Data Processing

The calibrated Stage 1 (*cal.fits) data products (both ϵ Ind A and selected archival reference observations) were acquired from MAST²⁰ and processed to Stage 3 (*stage3_asn_skysub.i2d.fits) with MAGIC (<https://github.com/kevin218/Magic>, e.g., R. Bowens-Rubin et al. 2025), a custom pipeline developed to address the non-uniform background structure in the MIRI flat-field. The Stage 2 background subtraction procedure in MAGIC follows an approach adapted from an STScI JWWebinar demo²¹, which applied a custom method utilizing multiple dithers per source. The Stage 3 reduction is identical to the `jwst` pipeline. We used MAGIC v1.0 and `jwst` v1.19.1; the calibration files were from CRDS v12.1.11 and the `jwst_1413.pmap` CRDS context.

We carry out PSF subtraction with `vip_hci` (C. A. Gomez Gonzalez et al. 2017; V. Christiaens et al. 2023), which uses the KLIP algorithm to model and subtract the host star PSF. In addition to the archival MIRI PSF library described in the previous section, we include synthetic `stpsf` models in our reference library. For each filter, we generate a set of 81 synthetic PSFs dithered across a grid of $[-2, 2]$ pixels in steps of 0.5 pixels. First, the ϵ Ind A PSF is centered on the frame by registering it to a `stpsf` model using the `chi2_shift` function in `image_registration` (masking the saturated core). The centers of the archival MIRI PSFs are determined visually in SAO DS9. Second, all PSFs are cropped about their center to a frame size of 81×81 pixels ($8''91 \times 8''91$ FOV) in F1800W and F2100W, and 101×101 pixels ($11''11 \times 11''11$ FOV) in F2550W. Third, we performed annular KLIP reductions (`pca_annular`) at the radial separation of ϵ Ind Ab (from NIRCAM astrometry) for various annular subtraction geometries parameterized by annulus size (`asize`), number of sections (`n_segments`), position angle of the first section (`theta_init`), and radial distance to the center of the annulus (`rad`). ϵ Ind Ab is robustly de-

tected in all three MIRI filters at its expected separation and position angle (Figure 1). The reductions presented use `asize`={2, 2, 2.5} FWHM²², `n_segments`={6, 8, 1} `theta_init`={0°, 40°, 0°}, `rad`={35, 34, 35} pixels, and {20, 17, 13} principal components for {F1800W, F2100W, F2550W}, detecting the planet at S/N = {7.7, 14.3, 7.5}, respectively. The F2550W detection of ϵ Ind Ab constitutes the longest wavelength image of an exoplanet taken to date.

2.2.3. Astrometry and Photometry

Astrometric and photometric measurements of ϵ Ind Ab are extracted using the negative fake companion injection (NEGFC) method (A. M. Lagrange et al. 2010; C. Marois et al. 2010). We apply NEGFC to our observations using `vip_hci`'s `firstguess` function. First, we generate a `stpsf` model with the appropriate MIRI filter, using the closest-in-time on-sky OPD map to the observations, and including detector effects. The `stpsf` model in each filter is normalized to the exit pupil of the optical system so that the sum of the PSF is 1.0 in an infinite aperture. We inject the model PSF at the NIRCAM measured position for varying *negative* flux values, perform PSF subtraction, and minimize a figure of merit in a {0.5, 0.5, 1} FWHM radius aperture at the location of injection for {F1800W, F2100W, F2550W} to obtain a first estimate of the planet's flux. The initial parameter estimates are input to a simplex Nelder–Mead minimization algorithm (J. A. Nelder & R. Mead 1965, implemented with argument `simplex = True`), which provides a more accurate estimate of the planet's separation, position angle, and flux. We minimize two figures of merit: (1) the reduced χ^2 and (2) the residual sum of squares (RSS). The two solutions (found to be consistent with each other) are averaged to obtain the final astrometry and photometry (Table 2).

For the astrometric uncertainty, we assume the radial and tangential directions are independent and calculate their uncertainties as FWHM/(S/N) (e.g., Y. Zhou et al. 2021). As discussed in §2.2.2, because of core saturation, ϵ Ind A was centered on the frame using the unsaturated PSF wings and by comparison with an `stpsf` model. This model does not perfectly represent the observed PSF. We thus adopt a centering uncertainty of 0.5 pixels (≈ 50 mas) and add it in quadrature to the above. The photometric uncertainty is dominated by speckle noise, which is estimated as the standard deviation of the integrated flux in non-overlapping 1 FWHM radius apertures at the separation of ϵ Ind Ab (D. Mawet et al. 2014). The astrometric and photometric uncertainties estimated using the above methods are conservative. We also implemented `vip_hci`'s nested sampling-based injection-recovery approach to directly estimate the un-

²⁰ The data described here may be obtained from the MAST archive at [10.17909/nqx2-yw28](https://archive.stsci.edu/mast).

²¹ https://github.com/spacetelescope/jwebbinar_prep/blob/jwebbinar31/jwebbinar31/miri/Pipeline_demo_subtract_imager_background-platform.ipynb

²² <https://jwst-docs.stsci.edu/jwst-mid-infrared-instrument/miri-performance/miri-point-spread-functions>

certainty from the posterior distributions for separation, position angle, and flux and found similar or slightly smaller values.

3. ORBITAL PROPERTIES

The JWST imaging search for ϵ Ind Ab (E. C. Matthews et al. 2024) was guided by evidence of a planet from a combined analysis of RV and absolute astrometry (F. Feng et al. 2019, 2023). However, the location of the imaged planet was discrepant with the original orbit prediction. This highlighted the challenge of modeling the orbits of wide separation companions, particularly when the RV time series consists of observations by several different instruments with independent offsets. Lessons learned are discussed in Appendix B. In this section, we combine three decades of radial velocity monitoring, Gaia-Hipparcos absolute astrometry, and relative astrometry from direct imaging (including our new NIR-Cam detection) to perform a comprehensive re-analysis of ϵ Ind Ab’s orbit. Though the orbit was recently revised by F. Feng et al. (2025), we find significant differences in our solution and discuss the reasons for the same.

3.1. Radial Velocity Data

We use publicly available radial velocity (RV) data on ϵ Ind A from the Data & Analysis Center for Exoplanets (DACE²³) platform. This includes 73 RVs from the Long Camera (LC) and 55 RVs from the Very Long Camera (VLC) of the Coudé Echelle Spectrometer at the European Southern Observatory (ESO, M. Zechmeister et al. 2013). The High Accuracy Radial-velocity Planet Searcher (HARPS) spectrograph has collected 4500+ RVs of ϵ Ind A (T. Trifonov et al. 2020). We binned data points collected by HARPS within a single night in DACE before using them in our analysis. This gives us 106 RVs from the pre-2015 upgrade (HARPS03), 38 RVs from the post-2015 upgrade (HARPS15), and 50 RVs from the post-2020 shutdown (HARPS20) period. The data above are treated as three separate instruments to account for any baseline shifts. We also use measurements from the Very Large Telescope (VLT) Echelle SPectrograph for Rocky Exoplanets and Stable Spectroscopic Observations (ESPRESSO, F. Pepe et al. 2021). A technical intervention was conducted in 2019 (F. Pepe et al. 2021) and we accordingly model the available data as two separate instruments. There are 48 ESPRESSO RVs available pre-2019 intervention and 70 ESPRESSO RVs available post-2019 intervention. Finally, we incorporate 164 RVs from the Ultraviolet and Visual Echelle Spectrograph (UVES, F. Feng et al. 2019). This gave us a total of 604 data points, from 8 independent instruments, covering a period of 29 years from November 3, 1992 to September 22, 2021.

²³ <https://dace.unige.ch/daceTeam/>

For all of the above, we use the RVs on DACE ignoring the ≈ 1.8 m/s/yr acceleration caused by the proper motion (secular acceleration). The RVs are not corrected for the changing light travel-time between ϵ Ind A and the Earth due to Earth’s motion around the Sun and ϵ Ind A’s changing distance from Earth. We handle both terms directly in our orbit model.

3.2. Relative Astrometry Data

We incorporate the relative astrometry of ϵ Ind Ab from previously published 2019 VLT/NEAR and 2023 JWST/MIRI F1550C observations (the F1065C astrometry is unreliable, E. C. Matthews et al. 2024) in addition to our new 2025 JWST/NIRCam measurement (Table 2). Together, the imaging observations (with detections) have a baseline of ≈ 6 years.

3.3. Absolute Astrometry Data

We include absolute astrometry of ϵ Ind A from Hipparcos and Gaia’s Third Data Release (DR3) in our orbit modeling. We use the Hipparcos proper motion from the DR3 Hipparcos-Gaia Catalog of Accelerations (HGCA: T. D. Brandt 2021), calculated from a mix of the ESA (1997) and F. van Leeuwen (2007) Hipparcos data releases, and calibrated against the Gaia DR3 velocity reference frame. We also include the Gaia DR3 proper motion and Gaia-Hipparcos long-term proper motion and uncertainties from the HGCA. We undo the non-linear corrections (γ term in Eq. 21 and 22 in T. D. Brandt 2018) incorporated by the HGCA to account for secular acceleration and curvature in the R.A. and Decl. coordinate system, in favor of handling this motion inside our model. Note that the above corrections ensure accurate cross-calibration between the Hipparcos and Gaia reference frames (see §5.1 in T. D. Brandt 2021); the Hipparcos and Gaia DR3 proper motions reported *at their respective epochs* are already corrected for secular acceleration using the systemic RV during the data reduction procedure (see Table 1.2.3 in ESA (1997)²⁴ and §3.1 in L. Lindegren et al. (2021)).

3.4. Model Implementation

We implemented our orbit model in the Julia-based (J. Bezanson et al. 2012) Octofitter framework (W. Thompson et al. 2023) and sample using stabilized variational nonreversible parallel tempering (N. Surjanovic et al. 2022; S. Syed et al. 2022) implemented in Pigeons.jl (N. Surjanovic et al. 2023). We jointly model the RVs, Hipparcos and Gaia absolute astrometry, and relative astrometry. The complete model incor-

²⁴ Note that F. van Leeuwen (2007) did not make the correction to the proper motion derived in their re-reduction. However, the magnitude of the correction is negligibly small (< 0.05 mas/yr⁻² in each coordinate direction) over the Hipparcos baseline and does not impact orbit fits.

Table 3. ϵ Ind Ab Orbit Modeling Parameters and Adopted Priors

Parameter	Description	Unit	Prior
M_A	Primary Mass	M_\odot	$\mathcal{N}(0.782, 0.023)$
M_b	Secondary Mass	M_{Jup}	$\mathcal{U}(0.01, 20)$
ϖ	Parallax	mas	$\mathcal{N}(274.8431, 0.0956)$
μ_{α^*}	Proper Motion (R.A.)	mas/yr	$\mathcal{U}(3965.661, 3967.661)$
μ_δ	Proper Motion (Decl.)	mas/yr	$\mathcal{U}(-2537.192, -2535.192)$
γ_*	Systemic RV	km/s	$\mathcal{N}(-40.035, 1)$
a	Semi-major Axis	au	$\mathcal{U}(1, 100), \mathcal{U}(\log 1, \log 100)^a$
e	Eccentricity	...	$\mathcal{U}(0, 0.999)$
i	Sky Inclination	...	Sine
ω	Argument of Periastron	rad	$\mathcal{U}(0, 2\pi)$
Ω	Longitude of Ascending Node	rad	$\mathcal{U}(0, 2\pi)$
θ	Position Angle at Reference Epoch	rad	$\mathcal{U}(0, 2\pi)$
B	GP Amplitude	m/s	$\mathcal{U}(0.00001, 2000000)$
C	GP Amplitude Ratio	...	$\mathcal{U}(0.00001, 200)$
L	GP Decay Timescale	days	$\mathcal{U}(2, 2000)$
P_{rot}	GP Rotation Period	days	$\mathcal{U}(1, 100)$
m	RV Slope	m/s/yr	$\mathcal{N}(0, 1)$
γ_{LC}	CES (LC) Zero Point	m/s	$\mathcal{U}(-100, 100)$
γ_{VLC}	CES (VLC) Zero Point	m/s	$\mathcal{U}(-100, 100)$
γ_{HARPS03}	HARPS03 Zero Point	m/s	$\mathcal{U}(-100, 100)$
γ_{HARPS15}	HARPS15 Zero Point	m/s	$\mathcal{U}(-100, 100)$
γ_{HARPS20}	HARPS20 Zero Point	m/s	$\mathcal{U}(-100, 100)$
γ_{ESPR18}	ESPR18 Zero Point	m/s	$\mathcal{U}(-100, 100)$
γ_{ESPR19}	ESPR19 Zero Point	m/s	$\mathcal{U}(-100, 100)$
γ_{UVES}	UVES Zero Point	m/s	$\mathcal{U}(-100, 100)$
σ_{LC}	CES (LC) Jitter	m/s	$\mathcal{U}(\log 0.01, \log 100)$
σ_{VLC}	CES (VLC) Jitter	m/s	$\mathcal{U}(\log 0.01, \log 100)$
σ_{HARPS03}	HARPS03 Jitter	m/s	$\mathcal{U}(\log 0.01, \log 100)$
σ_{HARPS15}	HARPS15 Jitter	m/s	$\mathcal{U}(\log 0.01, \log 100)$
σ_{HARPS20}	HARPS20 Jitter	m/s	$\mathcal{U}(\log 0.01, \log 100)$
σ_{ESPR18}	ESPR18 Jitter	m/s	$\mathcal{U}(\log 0.01, \log 100)$
σ_{ESPR19}	ESPR19 Jitter	m/s	$\mathcal{U}(\log 0.01, \log 100)$
σ_{UVES}	UVES Jitter	m/s	$\mathcal{U}(\log 0.01, \log 100)$

^aThe flat prior is used for “observable-based” prior model fits and the log-flat prior is used for the “uniform” prior model fit.

porating every listed data source has a total of 33 different parameters. The majority of these are instrument-specific nuisance parameters, which we marginalize over when presenting results. The full list of parameters and our adopted priors are listed in Table 3.

Non-linear effects in all of the above data such as secular acceleration and the changing light travel-time between ϵ Ind A and Earth are accounted for within the `Octofitter` model, identical to [W. Thompson et al. \(2025\)](#). To be conservative, we nonetheless include a linear trend for the RV datasets in our model. A single slope parameter (m) is shared between all RV datasets (system-wide parameter). Additionally, we use a separate RV offset/zero point (γ) and jitter (σ) for each instrument. Stellar activity is known to induce RV variability over multiple time-scales in the case of ϵ Ind A consistent with the star’s rotation period of ≈ 36 days

and magnetic cycle ([F. Feng et al. 2019](#); [M. S. Lundkvist et al. 2024](#)). We modeled the activity signal from the star using a Gaussian process (GP) with a quasi-periodic kernel. The GP, with parameters B , C , L , and P_{rot} (similar to ϵ Eridani in [R. M. Roettenbacher et al. \(2022\)](#); [W. Thompson et al. \(2025\)](#)), is implemented in our model using the `Celerite` ([D. Foreman-Mackey et al. 2017](#)) framework through the `Celerite.jl` package. We fit a single GP to the complete RV timeseries (system-wide parameters). We also conduct an orbit fit without a GP for comparison.

Given the low phase coverage of the relative astrometry, we use the framework of “observable-based” priors introduced in [K. K. O’Neil et al. \(2019\)](#) and imple-

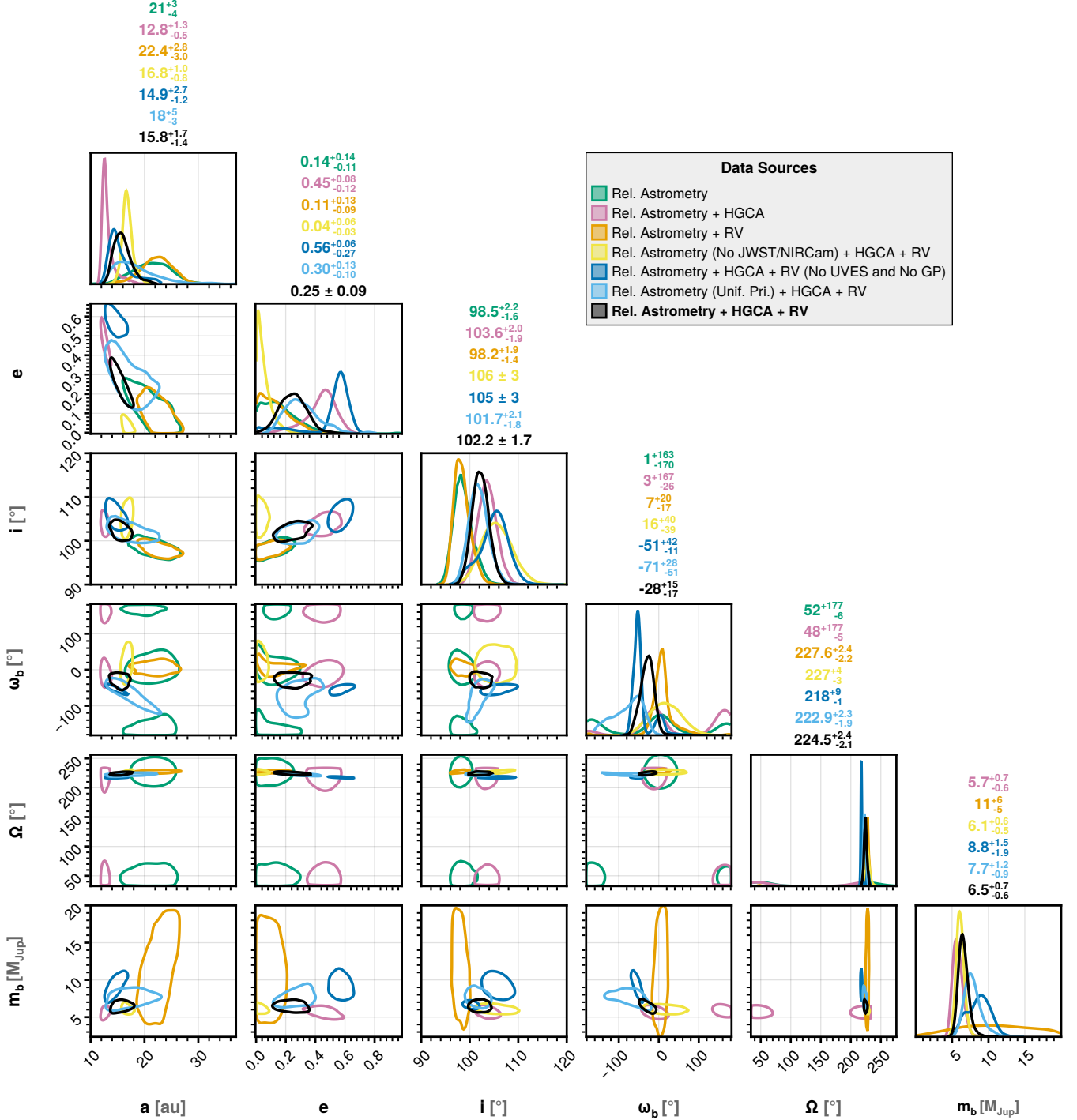


Figure 2. A comparison between posteriors from the seven converged (out of eight) orbit models considered for ϵ Ind Ab, listed in the legend. All contours in the corner plot encompass the volume contained within the 1σ 2D Gaussian equivalent. The final adopted model is in black and yields a dynamical mass $6.5^{+0.7}_{-0.6} M_{\text{Jup}}$. A key takeaway is that the new JWST/NIRCam astrometry provides evidence for a moderately eccentric orbit (yellow vs black posteriors).

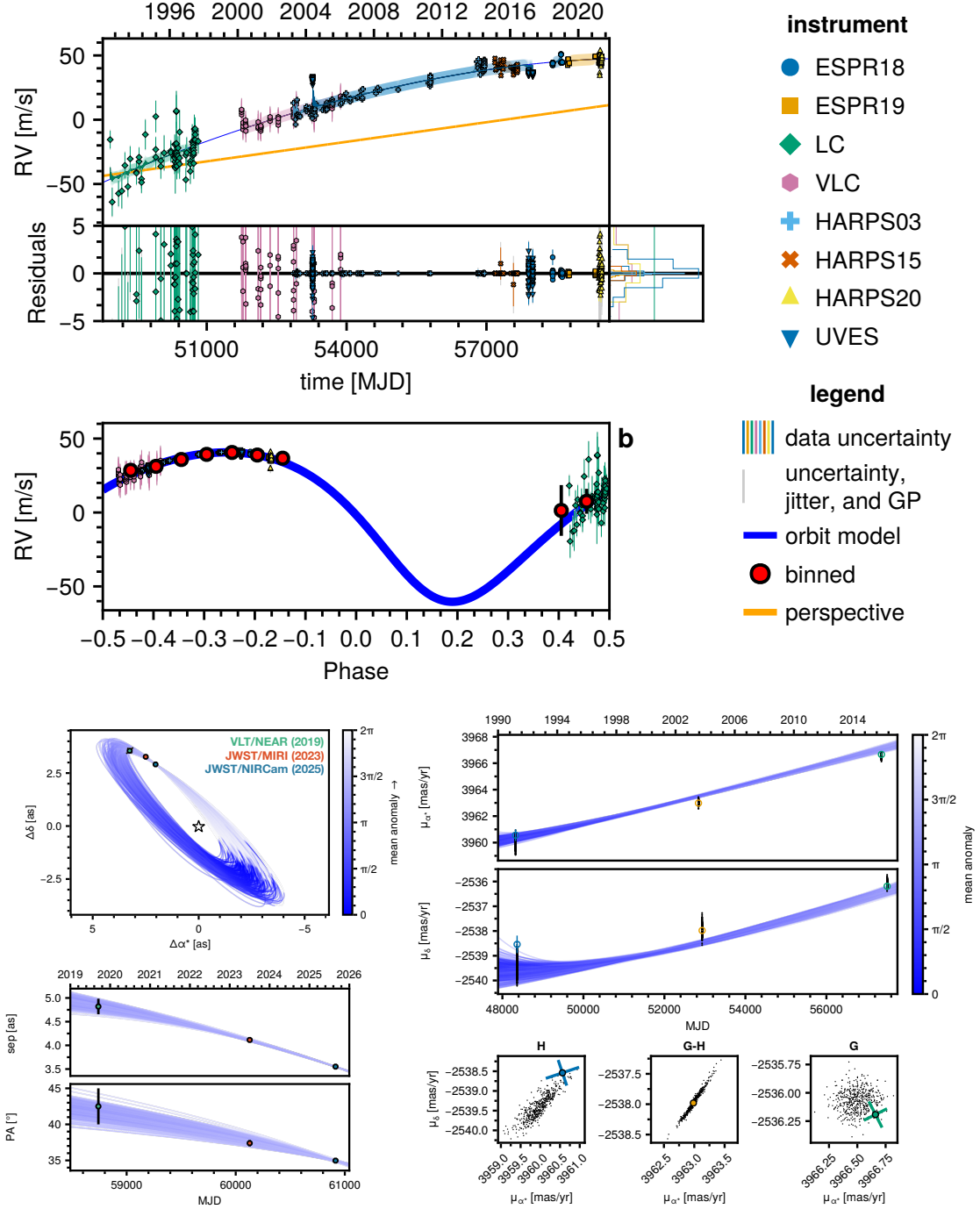


Figure 3. Summary of orbit fit for the complete relative astrometry + RV + HGCA model. *Top:* The top sub-panel shows the full RV timeseries with the model fit (dark blue) and residuals. Data from distinct instruments are represented with different colors and symbols. An orange line shows the effect of secular acceleration. The colored line connecting the points is the GP model and the colored band shows the uncertainty from the GP model. The bottom sub-panel shows the phase-folded model RV curve in blue. The binned data are shown as red points. *Bottom left:* The top sub-panel shows 250 randomly sampled sky-projected orbits with the measured relative astrometry. A mean anomaly of zero corresponds to periastron passage. The bottom sub-panel shows the corresponding projected separation and position angle vs time for the sampled orbits. *Bottom right:* The top sub-panel shows 500 random samples of the proper motion (PM) in R.A. and Decl. vs time with measurements from HGCA. The bottom sub-panel shows the covariances between R.A. and Decl. velocity at each PM epoch. The “H” epoch is the net PM at the Hipparcos epoch calibrated to the DR3 velocity reference by the HGCA, “G-H” is the long-term PM derived from the HGCA, and “G” is the Gaia DR3 PM.

mented in `Octofitter`²⁵. The prior is based on uniformity in orbital observables rather than in orbital parameters, and has the impact of reducing bias towards high eccentricity orbits and those where periastron passage occurs near the observed planet position (C. R. Do Ó et al. 2023). We also conduct an orbit fit with the “uniform” (standard) priors for comparison. All orbit models assume a single planet.

3.5. List of Models

Whenever we sample from a model that ignores a certain dataset, we remove the related instrument-specific nuisance parameters. By default, all fits use observable-based priors for the relative astrometry and include a GP in the RV model, unless specified otherwise. The models we consider are:

1. Relative astrometry only
2. Relative astrometry + HGCA
3. Relative astrometry + RV
4. Relative astrometry (No JWST/NIRCam) + HGCA + RV
5. Relative astrometry + HGCA + RV (No GP)
6. Relative astrometry + HGCA + RV (No UVES and No GP)
7. Relative astrometry (Uniform Priors) + HGCA + RV
8. Relative astrometry + HGCA + RV

We consider model #8 as our complete, fiducial model. We sample each model until the log-evidence converges between sampling rounds and the R diagnostic (A. Gelman & D. B. Rubin 1992; A. Vehtari et al. 2021) is ≈ 1 to at least two or more decimal places. For most models, this required 15 sampling rounds with `Octofitter`.

3.6. Results

We report parameter constraints both using credible intervals (CI) and highest density intervals (HDI), with the \pm notation used to indicate the median and 16%/84% quantiles, and the [lower, upper] notation to indicate the 75% HDI interval, similar to W. Thompson et al. (2025). We use 75% to emphasize the arbitrariness of the specific probability mass fraction. Tables for the above summarizing the posteriors of each model are presented in Appendix C. Figure 2 compares the different models tested against the fiducial model. Figure 3 visualizes the best-fit orbit obtained using the fiducial model.

3.6.1. Reliability of the UVES Data and Need for GP

Orbit fits for ϵ Ind Ab in the literature find a turnover in the RV trend with the inclusion of the HARPS20 data (E. C. Matthews et al. 2024; F. Feng et al. 2025). However, our best-fit model shows that the RV turnover has not been observed yet. The reason for this is a slope difference between the (UVES, HARPS15) and ESPRESSO data. The orbit fits of F. Feng et al. (2019, 2023); F. Philipot et al. (2023); E. C. Matthews et al. (2024); F. Feng et al. (2025) do not include the two sets of new ESPRESSO RVs. In those cases, the (UVES, HARPS15) data anchors the offset of the HARPS20 time series. Internally, both the UVES and HARPS15 time series have an average negative (downward) slope. It is then not surprising that previous orbit models found a turnover. However, it is apparent in Figure 3 that the downward slope of the (UVES, HARPS15) data is incompatible with the ESPRESSO data. The latter shows that ϵ Ind A’s RV is still trending upward (Figure 3). Indeed, we find that the orbit fit with all the data without using a GP (model #5) did not converge to a solution.

The inconsistency in slope between the (UVES, HARPS15) and ESPRESSO datasets is likely due to stellar activity. In an analysis of the long-term HARPS time series and corresponding activity indicators, F. Feng et al. (2019) find significant signals at periods of 2500 days and 278 days, related to the star’s magnetic cycle, and at periods of 11 days, 18 days, and 36 days, related to the star’s rotation period (alias, half period, and full period, respectively). Figure 4 shows that our fiducial model (#8), including a GP to mitigate stellar activity signals, provides a significantly better fit to the data (and can explain the UVES, HARPS15, and ESPRESSO RVs simultaneously) compared to a fit without the GP (excluding UVES, which has the strongest impact because of its long time baseline, to ensure convergence; model #6). Further, the GP period parameter P_{rot} converges to 18 ± 1 days, equal to the half-rotation period, which F. Feng et al. (2019) found to be more significant than the full rotation period in activity indicators, possibly due to spots. This consistency indicates that the GP is indeed modeling an activity signal in the RVs.

Together, this shows that using a GP in modeling the RVs of ϵ Ind A is physically-motivated and improves the reliability of the fit to the full RV time series. In particular, we emphasize that inclusion of the full UVES time series without a GP model will yield incorrect orbit estimates. Comparing results between the fiducial model (with GP) and the model without UVES and without a GP (model #6), we find consistent values for all parameters within 1σ – 2σ . However, the median eccentricity obtained without using a GP ($e = 0.56$) is $2\times$ higher than if a GP is used ($e = 0.25$). The two results are formally consistent because the eccentricity posterior in the fit without the GP is not Gaussian and has a long tail towards low eccentricities. As such, given the pre-

²⁵ <https://seffal.github.io/Octofitter.jl/stable/rel-astrom-obs/>

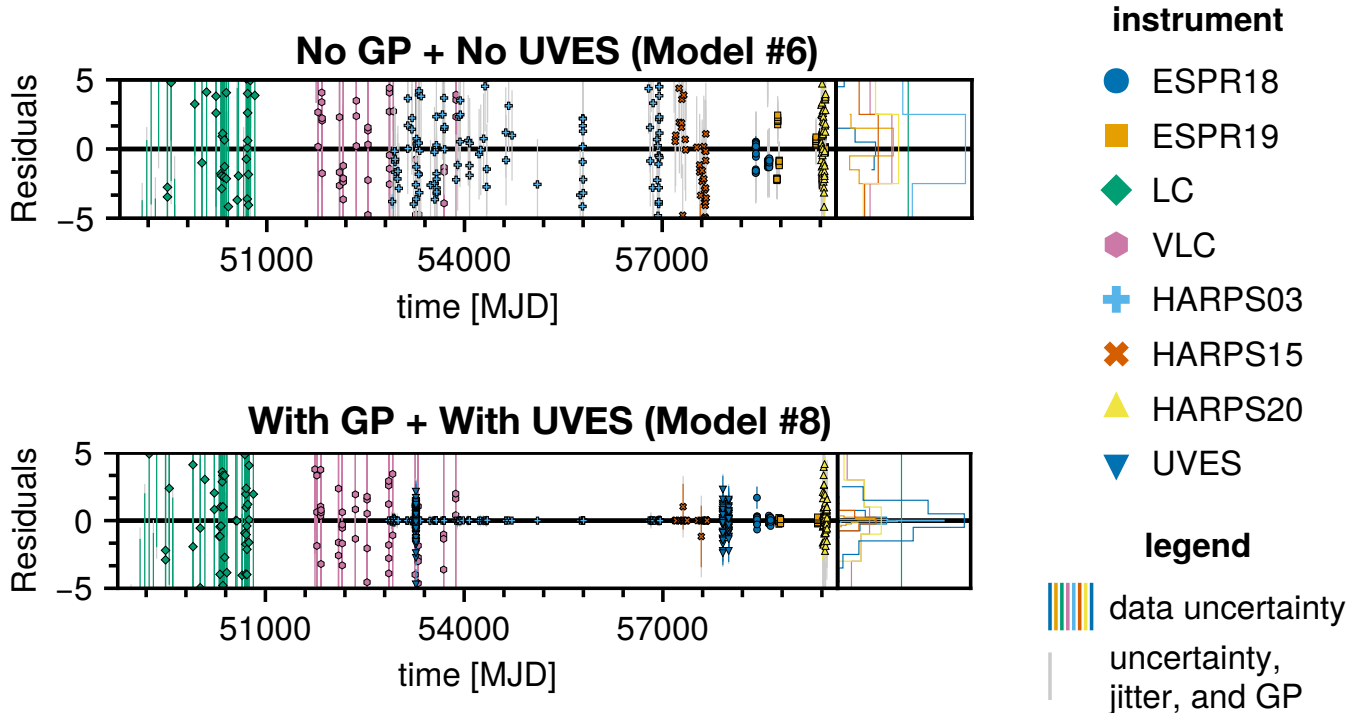


Figure 4. A comparison of the RV residuals obtained after fitting models without (top) and with (bottom) a GP, for the maximum posterior orbit. The GP explains variations in the RV time series and improves the residuals.

vious discussion on the motivation for using a GP, we caution that the high eccentricity in the fit without a GP is likely biased.

3.6.2. Observable-based Priors vs Uniform Priors

Comparing results between the fiducial model (#8) with observable-based priors (K. K. O’Neil et al. 2019) and the model with uniform priors (#7), we find that all the orbital parameters are consistent within 1σ – 2σ . This can be visually seen as an overlap between the respective 1σ contours in Figure 2 and indicates that our conclusions are robust to the choice of priors for the relative astrometry. The parameter uncertainties for the uniform prior fit are similar or larger than those for the observable-based prior fit.

3.6.3. Evidence for Moderate Orbital Eccentricity

The orbital eccentricity of ϵ Ind Ab is of particular interest as it is a key dynamical tracer of the planet’s formation and evolutionary history (B. P. Bowler et al. 2020; V. Nagpal et al. 2023; C. R. Do Ó et al. 2023). While previous orbit fits (E. C. Matthews et al. 2024; F. Feng et al. 2025) suggested a higher, non-zero, eccentricity (~ 0.4), the estimate was biased because of the impact of stellar activity on the RVs (see §3.6.1). In fact, an orbit fit to the relative astrometry (excluding the new JWST/NIRCam epoch) + HGCA + RV (model #4) converges to a circular orbit solution for the planet (75% highest density interval is $e = [0.00, 0.08]$;

also see Figure 2). Including the new JWST/NIRCam epoch in the orbit fit (model #8) results in a moderate, non-zero, orbital eccentricity $e = 0.25 \pm 0.09$, though the data are consistent with a circular orbit within the 3σ uncertainty range. It is worth noting that the relative astrometry + HGCA only fit (model #2) finds the highest eccentricity among all models considered (not including the case without a GP, see §3.6.1), $e = 0.45^{+0.08}_{-0.12}$. This suggests that there may be some tension between the RV dataset and the absolute astrometry from the HGCA. Continued RV monitoring of the system, with the goal of capturing the turnover, can help better constrain the eccentricity of the planet.

4. ATMOSPHERIC PROPERTIES

4.1. Comparison to WISE 0855

WISE J085510.83-071442.5 (also referred to as WISE 0855) is an isolated, late Y dwarf with a temperature of ~ 285 K and is the coldest brown dwarf discovered to date (K. L. Luhman 2014; A. J. Skemer et al. 2016). We compare ϵ Ind Ab’s photometry with synthetic photometry derived from the NIRSpec PRISM (K. L. Luhman et al. 2023) and MIRI MRS (H. Kühnle et al. 2025) spectrum of WISE 0855 (Figure 5). The F1800W–F1550C color serves as a good indicator of effective temperature as the spectral energy distribution is well-approximated by a blackbody at these wavelengths (Figure 5). We find a similar F1800W–F1550C color for ϵ Ind Ab ($m_{F1800W-F1550C} = 0.25$ mag) and

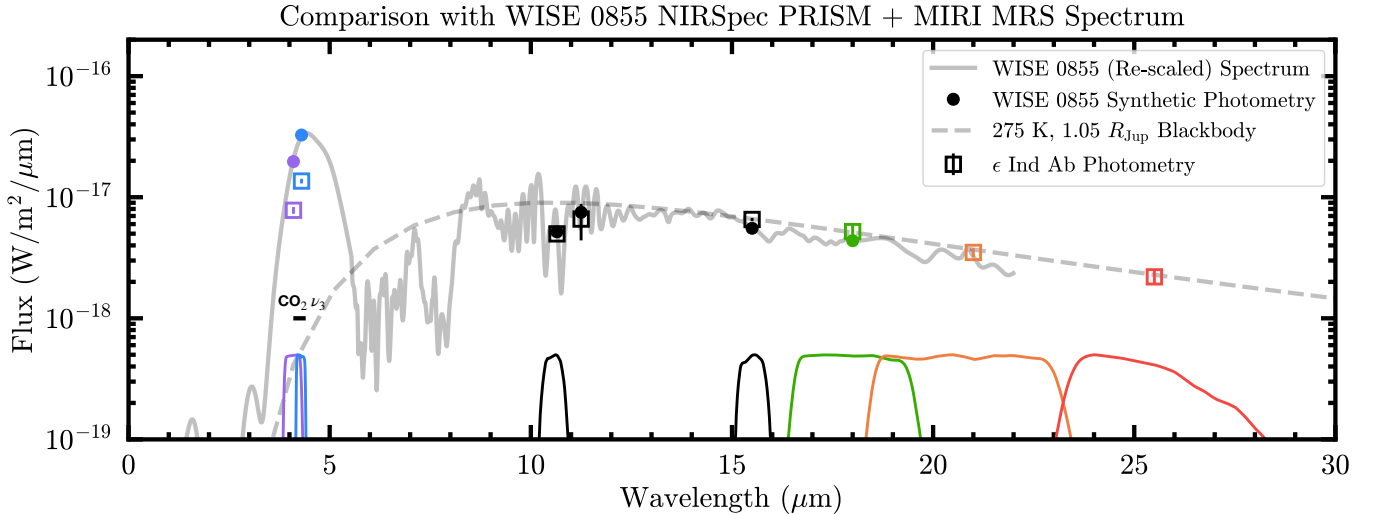


Figure 5. Comparison between ϵ Ind Ab’s and ~ 285 K brown dwarf WISE 0855’s spectral energy distributions. The colored open boxes with error bars represent ϵ Ind Ab’s measured photometry. WISE 0855’s spectrum (flux re-scaled to match the distance to ϵ Ind A and binned to $R \sim 50$) is shown in solid gray and the corresponding synthetic photometry is shown as colored filled circles. A reference blackbody spectrum is shown in dashed gray. The filter profiles are plotted below the photometry (no profile available for VLT/NEAR, constant transmission assumed between ≈ 10 – 12.5 μm). The 4.1 – 4.3 μm CO_2 absorption region is marked with a solid horizontal black line.

WISE 0855 ($m_{\text{F1800W-F1550C}} = 0.26$ mag) showing that the two substellar objects have similar effective temperatures. This is additionally supported by the evolutionary model analysis in §5. Interestingly, ϵ Ind Ab’s NIRC-Cam F410M/F430M fluxes are $\approx 2.5\times$ fainter than those of WISE 0855 (Figure 5). The 4.1 – 4.3 μm CO_2 absorption feature dominates in the above NIRC-Cam filters and its strength depends strongly on atmospheric metallicity (K. Lodders & B. Fegley 2002; K. Zahnle et al. 2009; Z. Rustamkulov et al. 2023; W. O. Balmer et al. 2025a; J.-B. Ruffio et al. 2026; J. W. Xuan et al. 2026; A. Sanghi et al. 2026). The retrieved volume mixing ratio for CO_2 in WISE 0855’s atmosphere is extremely small, $\sim 10^{-9}$ (H. Kühnle et al. 2025). A higher atmospheric metallicity compared to WISE 0855 and, consequently, an elevated CO_2 abundance in ϵ Ind Ab’s atmosphere could explain the difference in NIRC-Cam fluxes. The atmospheric metallicity of WISE 0855 is not well-determined and H. Kühnle et al. (2025) find that different grid models yield different values. A second possibility is that water clouds in the atmosphere suppress the 4 – 5 μm flux (e.g., B. Lacy & A. Burrows 2023). Both scenarios are explored in more detail in the following section.

4.2. Self-Consistent Grid Model Analysis

In this section, we compare the 4 – 25 μm photometric spectral energy distribution of ϵ Ind Ab to precomputed grids of self-consistent radiative-convective equilibrium models. We present initial results on the atmospheric properties of ϵ Ind Ab based on the best-fitting models and derive the planet’s bolometric luminosity for comparisons with evolutionary model predictions.

4.2.1. Model Grids

We consider the following model grids for our atmospheric analysis. The specific parameter values explored by each grid are summarized in Table 4.

Sonora Elf Owl. The Sonora Elf Owl grid (S. Mukherjee et al. 2024) consists of cloud-free atmospheric models computed using PICASO 3.0 (S. Mukherjee et al. 2023), a 1D radiative-convective equilibrium climate model, that includes the effects of disequilibrium chemistry (parameterized by diffusion parameter K_{zz}) for a wide range of substellar temperatures, surface gravities, atmospheric metallicities, and C/O ratios. We use the latest version of the models presented in N. F. Wogan et al. (2025) that correctly estimate the CO_2 quenching.

Sonora Flame Skimmer. The Sonora Flame Skimmer grid (Mang et al., in prep) extends the cloud-free Sonora Elf Owl grid (S. Mukherjee et al. 2024; N. F. Wogan et al. 2025) to colder effective temperatures, lower surface gravities, and a broader range of metallicities. These models additionally incorporate rainout chemistry for H_2O , CH_4 , and NH_3 —even in cloud-free atmospheres—similar to the treatment in Sonora Bobcat. They address the underestimation of CO_2 found in the Sonora Elf Owl models (S. Mukherjee et al. 2024), which has since been revised in N. F. Wogan et al. (2025).

Custom PICASO Water Cloud Models. We generate a custom grid of cloudy (H_2O) atmospheric models using PICASO (N. E. Batalha et al. 2019; S. Mukherjee et al. 2023; J. Mang et al. 2026). PICASO now supports fully self-consistent cloudy atmosphere calculations through integration with Virga (N. Batalha et al. 2020b; N. E.

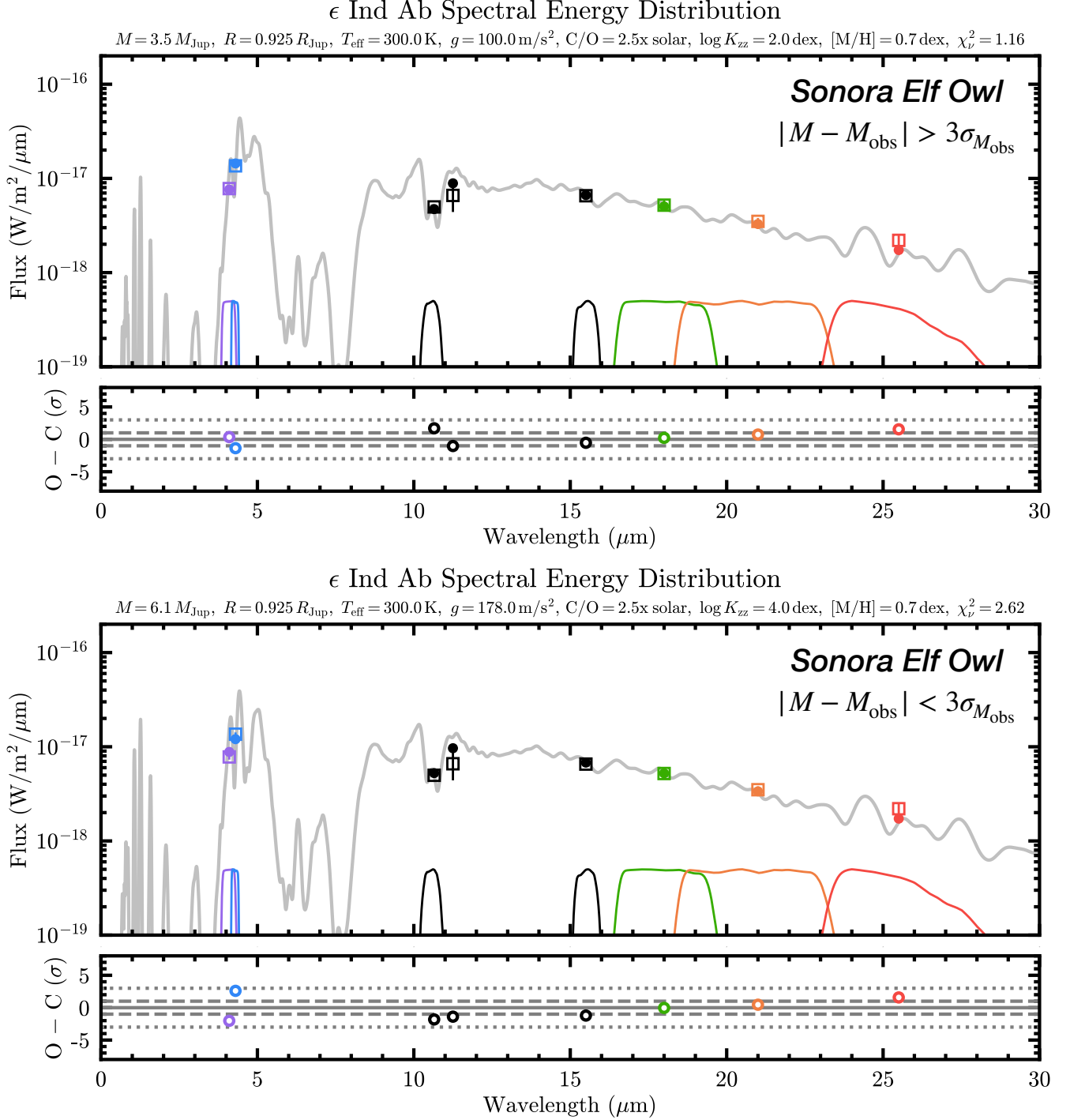


Figure 6. Atmospheric model fits with the Sonora Elf Owl grid. The top panel presents the lowest χ^2_{ν} fit from the model grid. The bottom panel presents the lowest χ^2_{ν} fit from the model grid that also predicts a mass consistent with the dynamical mass within 3σ . In each panel, the colored open boxes with error bars represent ϵ Ind Ab’s measured photometry. The model atmosphere is shown in gray (binned to $R \sim 50$) and the corresponding synthetic photometry are shown as colored filled circles. The filter profiles are plotted below the photometry (no profile available for VLT/NEAR, constant transmission assumed between ≈ 10 – $12.5 \mu\text{m}$). A sub-panel below the spectral energy distribution shows the residuals (in units of σ). Gray dashed and dotted lines mark 1σ and 3σ intervals.

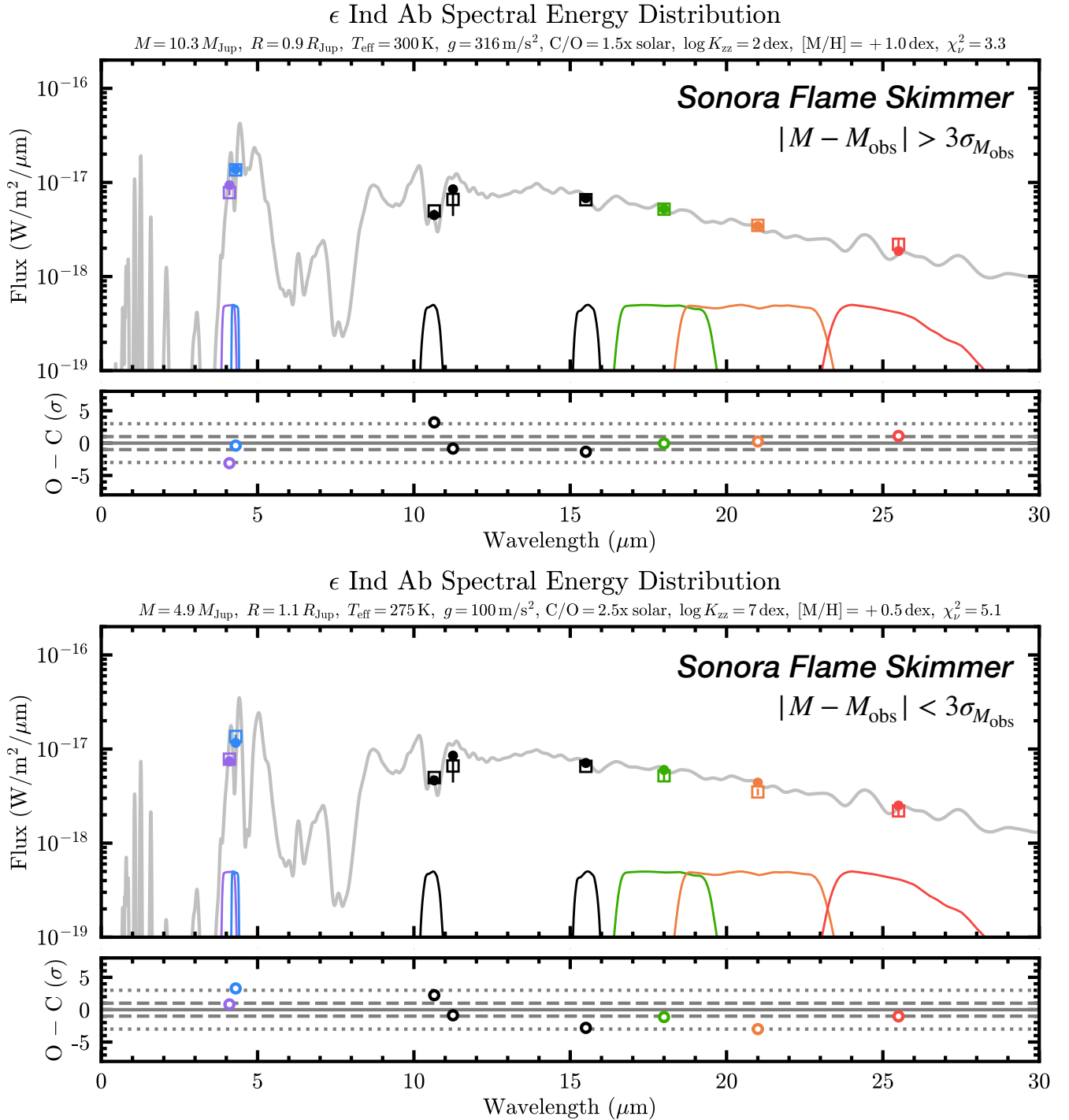


Figure 7. The overall lowest χ_{ν}^2 atmospheric model fit (top) and the lowest χ_{ν}^2 atmospheric model fit also consistent with the dynamical mass within 3σ (bottom) from the Sonora Flame Skimmer grid. The format of the individual panels is identical to that described in Figure 6.

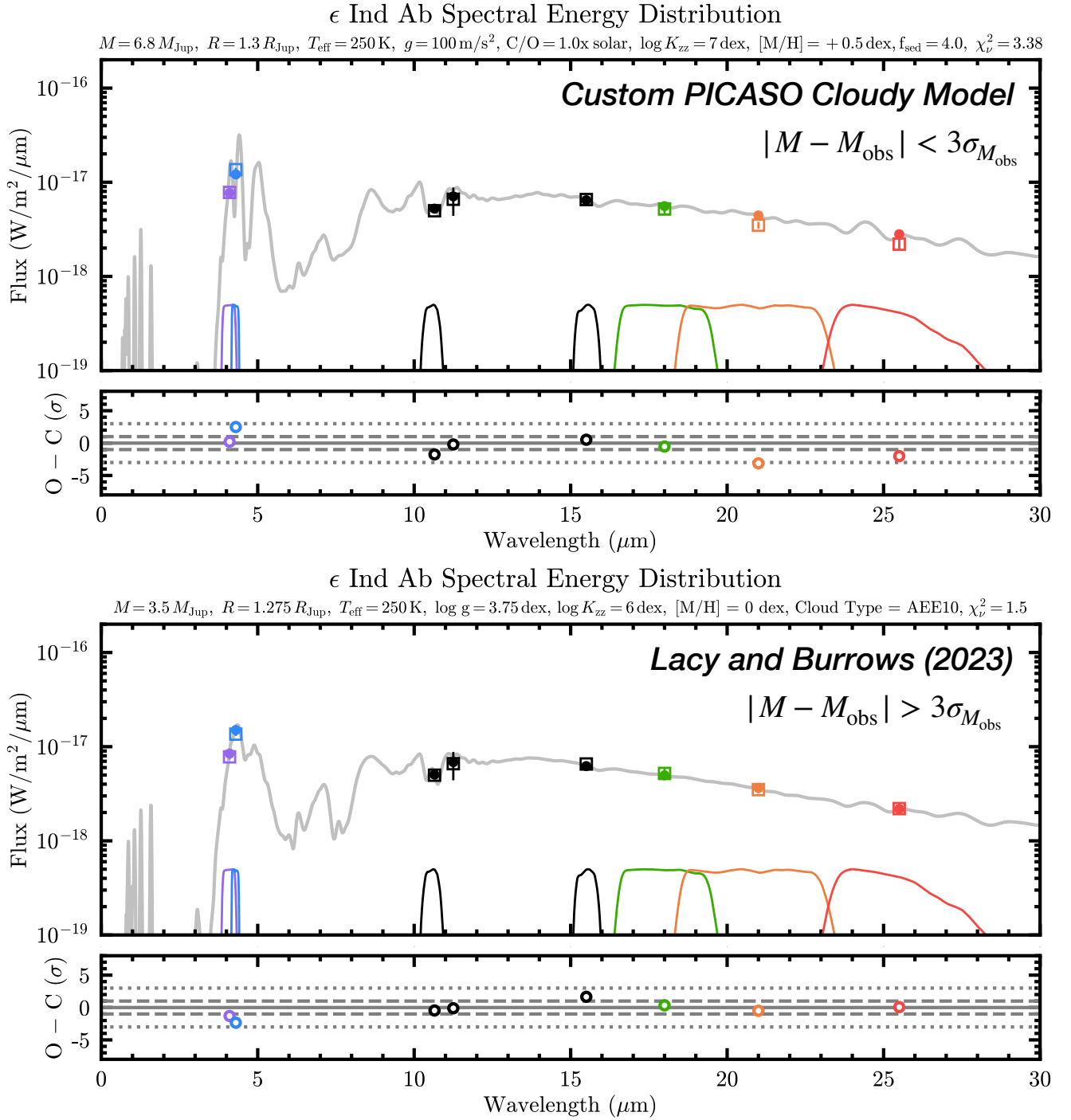


Figure 8. The lowest χ^2_{ν} atmospheric model fit from the custom PICASO water cloud models (top) and the B. Lacy & A. Burrows (2023) models (bottom). The format of the individual panels is identical to that described in Figure 6.

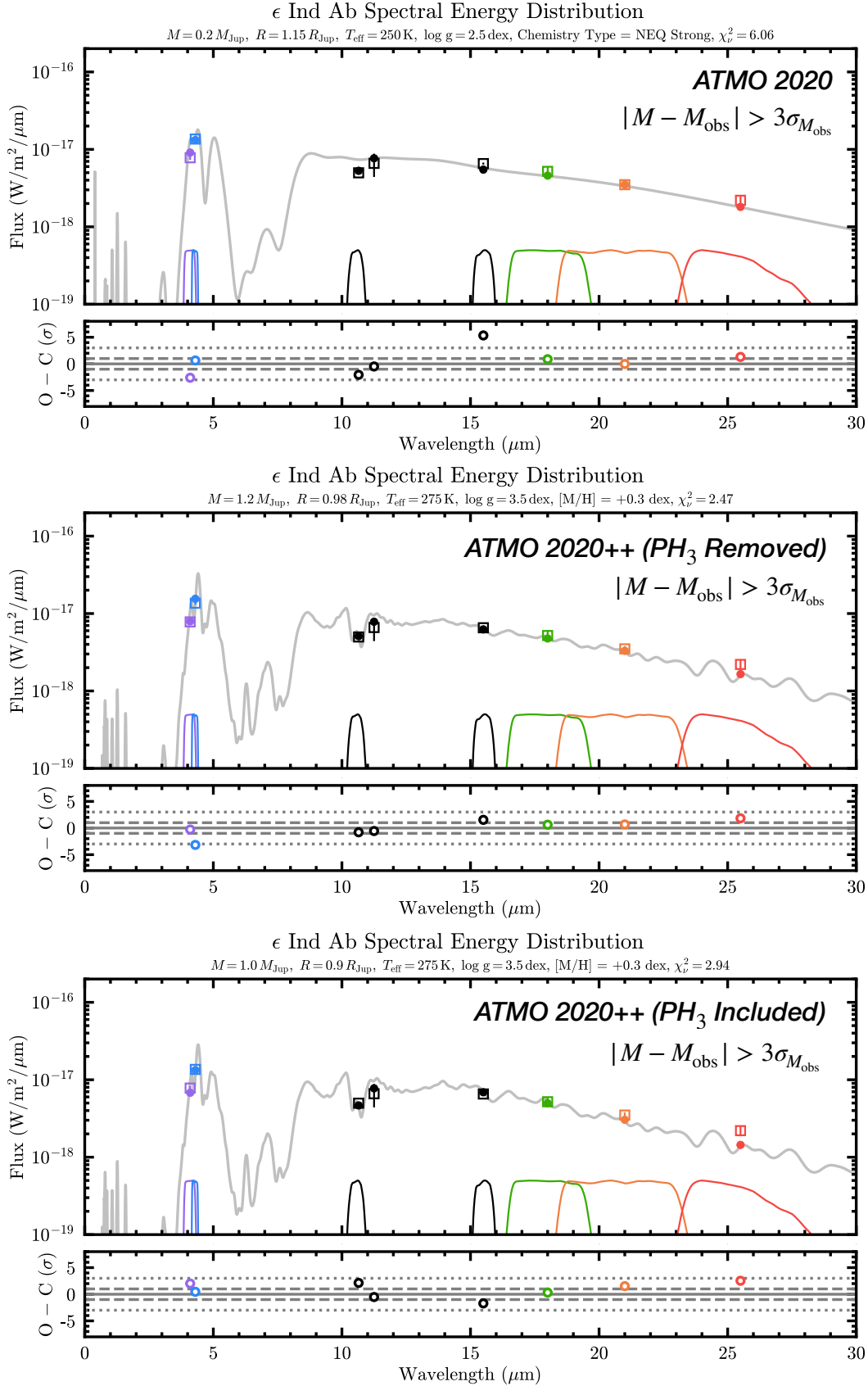


Figure 9. The lowest χ^2_{ν} atmospheric model fit from the ATMO 2020 (top), ATMO 2020++ without PH₃ (center), and ATMO 2020++ with PH₃ (bottom). The format of the individual panels is identical to that described in Figure 6.

Table 4. Atmospheric Model Grids

Parameter	Values
Sonora Elf Owl	
T_{eff} (K)	{275, 300}
g (m/s ²)	{100, 178, 316}
[M/H] (dex)	{−1.0, −0.5, 0, +0.5, +0.7, +1.0}
C/O (\times solar)	{0.5, 1.0, 1.5, 2.5}
$\log [K_{zz}$ (cm ² s ^{−1})]	{2, 4, 7, 8, 9}
Sonora Flame Skimmer	
T_{eff} (K)	{250, 275, 300}
g (m/s ²)	{100, 178, 316}
[M/H] (dex)	{−1.0, −0.5, 0, +0.5, +1.0, +1.5, +2.0}
C/O (\times solar)	{0.5, 1.0, 1.5, 2.5}
$\log [K_{zz}$ (cm ² s ^{−1})]	{0, 2, 4, 7, 8, 9}
Custom PICASO Cloudy Models	
T_{eff} (K)	{250, 275, 300}
g (m/s ²)	{100, 178, 316}
[M/H] (dex)	{0, +0.5, +1.0}
C/O (\times solar)	{1.0, 2.5}
$\log [K_{zz}$ (cm ² s ^{−1})]	{0, 2, 7, 9}
f_{sed}	{4, 6, 8}
B. Lacy & A. Burrows (2023)	
T_{eff} (K)	{250, 275, 300}
$\log [g$ (cm/s ²)]	{3.50, 3.75, 4.00, 4.25, 4.50, 4.75}
[M/H] (dex)	{−0.5, 0, +0.5}
$\log [K_{zz}$ (cm ² s ^{−1})]	{0, 6}
Cloud Type	None, E10, AEE10
ATMO 2020	
T_{eff} (K)	{250, 300}
$\log [g$ (cm/s ²)]	{2.5, 3.0, 3.5, 4.0, 4.5}
[M/H] (dex)	{−0.5, 0, +0.5}
Chemistry Type	{CEQ, NEQ Weak, NEQ Strong}
ATMO 2020++ (PH ₃ Removed)	
T_{eff} (K)	{250, 275, 300}
$\log [g$ (cm/s ²)]	{2.5, 3.0, 3.5, 4.0, 4.5}
[M/H] (dex)	{−0.5, 0, +0.3}
ATMO 2020++ (PH ₃ Included)	
T_{eff} (K)	{250, 275, 300}
$\log [g$ (cm/s ²)]	{2.5, 3.0, 3.5, 4.0, 4.5}
[M/H] (dex)	{−1.0, −0.5, 0, +0.3}

NOTE—Models with all possible combinations of listed parameters, when available (not all model grids are rectangular), are fit to the data. Chemical equilibrium models are noted above with $\log [K_{zz}$ (cm² s^{−1})] = 0 dex for convenience only.

Batalha et al. 2025; S. E. Moran et al. 2025), the Python implementation of the A. S. Ackerman & M. S. Marley (2001) cloud model. The clouds are parameterized with a sedimentation efficiency (f_{sed}) parameter. Generally, the optical thickness and vertical extent of the cloud decreases and particle size increases with increasing f_{sed} .

B. Lacy & A. Burrows (2023) Models. This grid consists of a suite of 1D radiative-convective equilibrium models computed with coolTLUSTY (I. Hubeny & T. Lanz 1995; D. Sudarsky et al. 2005; A. Burrows et al. 2008) including updated opacities and the effects of both disequilibrium chemistry and water clouds in Y dwarf atmospheres. Specifically, two water cloud types, labeled “E10” and “AEE10”, are presented. The modal cloud particle size is 10 μm in both cases. The key difference is vertical extent: the E10 clouds are vertically compact and the AEE10 clouds are vertically extended.

ATMO 2020. ATMO 2020 (M. W. Phillips et al. 2020) is a set of solar metallicity atmospheric models that incorporate the effects of non-equilibrium chemistry due to vertical mixing in the atmosphere (“NEQ Weak” and “NEQ Strong”, corresponding to different mixing strengths). Key improvements in ATMO 2020 over previous model grids include a new H-He equation of state, updated molecular opacities, and better treatment of the collisionally broadened potassium resonance doublet.

ATMO 2020++. Using the ATMO 2020 models with strong vertical mixing as a starting point, ATMO 2020++ (S. K. Leggett et al. 2021; A. M. Meisner et al. 2023; S. K. Leggett & P. Tremblin 2024a) modifies the adiabatic ideal gas index γ (and thus atmospheric temperature gradient) to account for the effect of processes responsible for producing a non-adiabatic cooling curve in giant planet and brown dwarf atmospheres. These processes include complex atmospheric dynamics (e.g., zones, spots, waves) due to rapid rotation, compositional changes due to condensation, upper atmosphere heating by cloud decks or breaking gravity waves, etc. Recent modeling with JWST data has shown that this grid provides an improved fit to Y dwarf spectra compared to the standard-adiabat models (S. K. Leggett & P. Tremblin 2023, 2024b; K. L. Luhman et al. 2023). We use both the model grids with and without PH₃.

Table 5. Atmospheric Model Fits to the Measured Planet Photometry with $\chi^2_{\nu} < 10$

T_{eff} (K)	g or $\log g$ (m s^{-2} or $\log [\text{cm s}^{-2}]$)	[M/H] (dex)	$\log K_{zz}$ or Chemistry ($\log [\text{cm}^2 \text{s}^{-1}]$)	C/O (\times solar)	Cloud Type or f_{sed}	R (R_{Jup})	M (M_{Jup})	$\log L_{\text{bol}}/L_{\odot}$ (dex)	χ^2_{ν}	$3\sigma_{M_b}$
Sonora Elf Owl										
300	178	+0.7	4 dex	2.5	...	0.925	6.1	-7.21	2.62	✓
275	178	+0.5	7 dex	2.5	...	1.025	7.5	-7.22	4.24	✓
275	178	+0.5	8 dex	2.5	...	1.025	7.5	-7.23	4.39	✓
275	100	+0.7	4 dex	1.5	...	1.1	4.9	-7.20	7.11	✓
275	178	+0.5	9 dex	2.5	...	1.05	7.9	-7.21	9.64	✓
300	100	+0.7	2 dex	2.5	...	0.925	3.5	-7.21	1.16	×
275	100	+0.5	7 dex	2.5	...	1.025	4.2	-7.22	2.17	×
300	100	+0.7	4 dex	1.5	...	0.925	3.5	-7.22	3.43	×
300	316	+1.0	2 dex	1.5	...	0.925	10.9	-7.21	4.55	×
300	100	+1.0	2 dex	1.0	...	0.95	3.6	-7.20	5.6	×
300	100	+0.5	4 dex	2.5	...	0.875	3.1	-7.25	7.15	×
300	316	+0.7	4 dex	2.5	...	0.875	9.8	-7.25	7.31	×
275	316	+0.7	7 dex	2.5	...	1.025	13.4	-7.22	8.7	×
Sonora Flame Skimmer										
275	100	+0.5	7 dex	2.5	...	1.1	4.9	-7.19	5.10	✓
275	178	+0.5	7 dex	2.5	...	1.075	8.3	-7.22	5.82	✓
300	178	+1.0	2 dex	1.5	...	0.9	5.8	-7.21	6.28	✓
275	100	+0.5	7 dex	1.5	...	1.05	4.4	-7.23	8.84	✓
275	100	+0.5	8 dex	1.5	...	1.1	4.9	-7.19	9.03	✓
300	178	+0.5	7 dex	2.5	...	0.9	5.8	-7.22	9.35	✓
300	316	+1.0	2 dex	1.5	...	0.9	10.3	-7.22	3.30	×
300	100	+1.0	2 dex	1.0	...	0.925	3.5	-7.20	5.65	×
275	178	+0.5	8 dex	2.5	...	1.1	8.7	-7.20	5.81	×
300	100	+0.5	4 dex	2.5	...	0.875	3.1	-7.24	6.07	×
300	100	+0.5	7 dex	2.5	...	0.9	3.3	-7.22	9.22	×
Custom PICASO Cloudy Models										
250	100	+0.5	7 dex	1.0	4.0	1.3	6.8	-7.21	3.38	✓
250	100	0	0 dex	1.0	8.0	1.25	6.3	-7.23	4.38	✓
250	100	+0.5	0 dex	1.0	6.0	1.275	6.6	-7.22	4.77	✓
275	178	+0.5	7 dex	2.5	6.0	1.05	7.9	-7.23	5.23	✓
250	100	0	9 dex	2.5	4.0	1.225	6.1	-7.26	5.24	✓
250	100	0	0 dex	2.5	8.0	1.275	6.6	-7.22	5.48	✓
275	178	+0.5	7 dex	2.5	8.0	1.075	8.3	-7.22	5.71	✓
250	100	0	0 dex	1.0	6.0	1.275	6.6	-7.22	7.64	✓
250	100	0	2 dex	1.0	6.0	1.275	6.6	-7.22	7.71	✓
275	100	+1.0	0 dex	2.5	6.0	1.05	4.4	-7.22	7.81	✓
250	100	0	2 dex	2.5	8.0	1.275	6.6	-7.22	8.08	✓
250	100	+0.5	2 dex	2.5	4.0	1.275	6.6	-7.22	8.48	✓
300	178	+0.5	7 dex	2.5	6.0	0.875	5.5	-7.24	9.90	✓
275	316	+1.0	0 dex	1.0	8.0	1.05	14.1	-7.22	3.55	×
250	316	0	0 dex	1.0	8.0	1.275	20.7	-7.23	4.49	×
250	316	0	0 dex	1.0	6.0	1.275	20.7	-7.24	5.53	×
275	316	+0.5	9 dex	2.5	8.0	1.05	14.1	-7.23	5.70	×
275	316	+0.5	9 dex	2.5	6.0	1.05	14.1	-7.22	6.44	×
250	316	+0.5	9 dex	1.0	8.0	1.275	20.7	-7.22	6.65	×
275	316	+0.5	9 dex	2.5	4.0	1.025	13.4	-7.25	6.76	×
250	316	0	7 dex	2.5	8.0	1.2	18.4	-7.27	7.03	×
250	178	0	0 dex	1.0	8.0	1.275	11.7	-7.22	7.12	×
250	316	0	0 dex	2.5	6.0	1.275	20.7	-7.23	7.33	×
250	316	+0.5	2 dex	2.5	4.0	1.25	19.9	-7.24	7.40	×
250	316	0	0 dex	2.5	8.0	1.275	20.7	-7.23	7.43	×

Table 5 continued

Table 5 (*continued*)

T_{eff}	g or $\log g$	[M/H]	$\log K_{zz}$ or Chemistry	C/O	Cloud Type or f_{sed}	R	M	$\log L_{\text{bol}}/L_{\odot}$	χ_{ν}^2	$3\sigma_{M_b}$
(K)	(m s^{-2} or $\log [\text{cm s}^{-2}]$)	(dex)	($\log [\text{cm}^2 \text{s}^{-1}]$)	(\times solar)		(R_{Jup})	(M_{Jup})	(dex)		
250	316	0	2 dex	1.0	6.0	1.25	19.9	-7.24	8.10	\times
275	316	+0.5	0 dex	1.0	6.0	1.0	12.7	-7.27	8.54	\times
250	316	+1.0	0 dex	1.0	8.0	1.275	20.7	-7.22	8.85	\times
300	100	+0.5	7 dex	2.5	8.0	0.9	3.3	-7.22	9.15	\times
B. Lacy & A. Burrows (2023)										
250	3.75 dex	0	6 dex	...	AEE10	1.275	3.5	-7.25	1.50	\times
275	3.75 dex	+0.5	0 dex	...	AEE10	1.05	2.4	-7.22	1.57	\times
275	4.00 dex	+0.5	0 dex	...	AEE10	1.05	4.3	-7.22	3.45	\times
275	3.50 dex	0	6 dex	...	E10	1.025	1.3	-7.24	4.60	\times
ATMO 2020										
250	2.5 dex	0	NEQ Strong	1.15	0.2	-7.30	6.06	\times
ATMO 2020++ (PH₃ Removed)										
275	3.5 dex	+0.3	0.98	1.2	-7.26	2.47	\times
250	2.5 dex	0	1.18	0.2	-7.24	4.08	\times
ATMO 2020++ (PH₃ Included)										
275	3.5 dex	+0.3	0.90	1.0	-7.28	2.94	\times
275	3.0 dex	0	0.85	0.3	-7.30	5.81	\times
300	3.5 dex	+0.3	0.75	0.7	-7.30	7.33	\times

NOTE—The atmospheric models are sorted in ascending order of their χ_{ν}^2 and divided into two categories (where applicable) based on consistency of the predicted mass with the dynamical mass ($6.5 \pm 0.7 M_{\text{Jup}}$) within 3σ , as noted in the last column ($3\sigma_{M_b}$). The overall lowest χ_{ν}^2 model fit and the lowest χ_{ν}^2 model fit consistent with the dynamical mass within 3σ are both marked as bolded entries.

4.2.2. Model Fitting

We jointly fit the F410M and F430M JWST/NIRCam flux and the F1065C, F1550C, F1800W, F2100W, and F2550W JWST/MIRI flux to all of the atmosphere models listed in Table 4 (upper limits and the NEAR photometry are not considered). The fitting procedure synthesizes model photometry in the JWST bandpasses using the transmission curve from the Spanish Virtual Observatory (SVO) filter profile service²⁶ and finds the radius (within a range of 0.5–1.5 R_{Jup} , though we note the extremes are unphysical according to evolutionary models) that minimizes the χ_{ν}^2 with respect to the measured photometry. Models that fit the observed photometry with $\chi_{\nu}^2 < 10$ are listed in Table 5. For each model, we also consider whether the predicted mass (from model surface gravity and fit radius) is consistent with the dynamical mass within 3σ . The lowest χ_{ν}^2 model fits from each atmospheric grid are visualized in Figures 6, 7, 8, and 9.

4.2.3. Atmospheric Metallicity

The atmospheric metallicity of a giant planet is a key observational probe of the relative importance of solid and gas accretion during the planet formation process (e.g., Y. Hasegawa et al. 2018; M. Ikoma & H. Kobayashi

2025). The transiting giant exoplanets follow a well-established empirical mass-metallicity relation (T. Guillot et al. 2006; N. Miller & J. J. Fortney 2011; D. P. Thorngren et al. 2016) consistent with core accretion theory. Atmospheric studies of distant imaged planets ($\gtrsim 10$ au) also find evidence of super-stellar atmospheric metallicities, suggesting that distant giants likely also accrete significant metal content (e.g., E. Nasedkin et al. 2024; W. O. Balmer et al. 2025a,b; A. Madurowicz et al. 2025; J.-B. Ruffio et al. 2026; J. W. Xuan et al. 2026).

Recently, Y. Chachan et al. (2025) revised the giant planet mass-metallicity relation based on estimates of the bulk heavy element content of 147 warm (< 1000 K) giant planets with measured masses and radii. Using the best-fit relation, $Z_p/Z_* = a/M_p + b$, where Z_p is the bulk metallicity of the planet, Z_* is the stellar metallicity, M_p is planet mass in Jupiter masses, $a = 2.6 \pm 0.3$, and $b = 3.3 \pm 0.5$, we find $Z_p/Z_* = 3.7 \pm 0.5$ for ϵ Ind Ab (for the known dynamical mass of the planet). To convert the above ratio to atmospheric metallicity [M/H], we use the method of D. Thorngren & J. J. Fortney (2019) adapted by E. Nasedkin et al. (2024, Equations 18–20). Given ϵ Ind A’s [Fe/H] = -0.17 ± 0.03 (M. S. Lundkvist et al. 2024), we find [M/H] = 0.4 ± 0.1 dex. The calculation assumes the interior is well-mixed such that the atmospheric metallicity is a good approximation of the planet’s bulk metallicity. This is not an unrealistic assumption for massive planets ($\gtrsim 2 M_{\text{Jup}}$). A similar calculation, for example, with AF Lep b ($3.75 \pm 0.50 M_{\text{Jup}}$)

²⁶ <http://svo2.cab.inta-csic.es/theory/fps/>

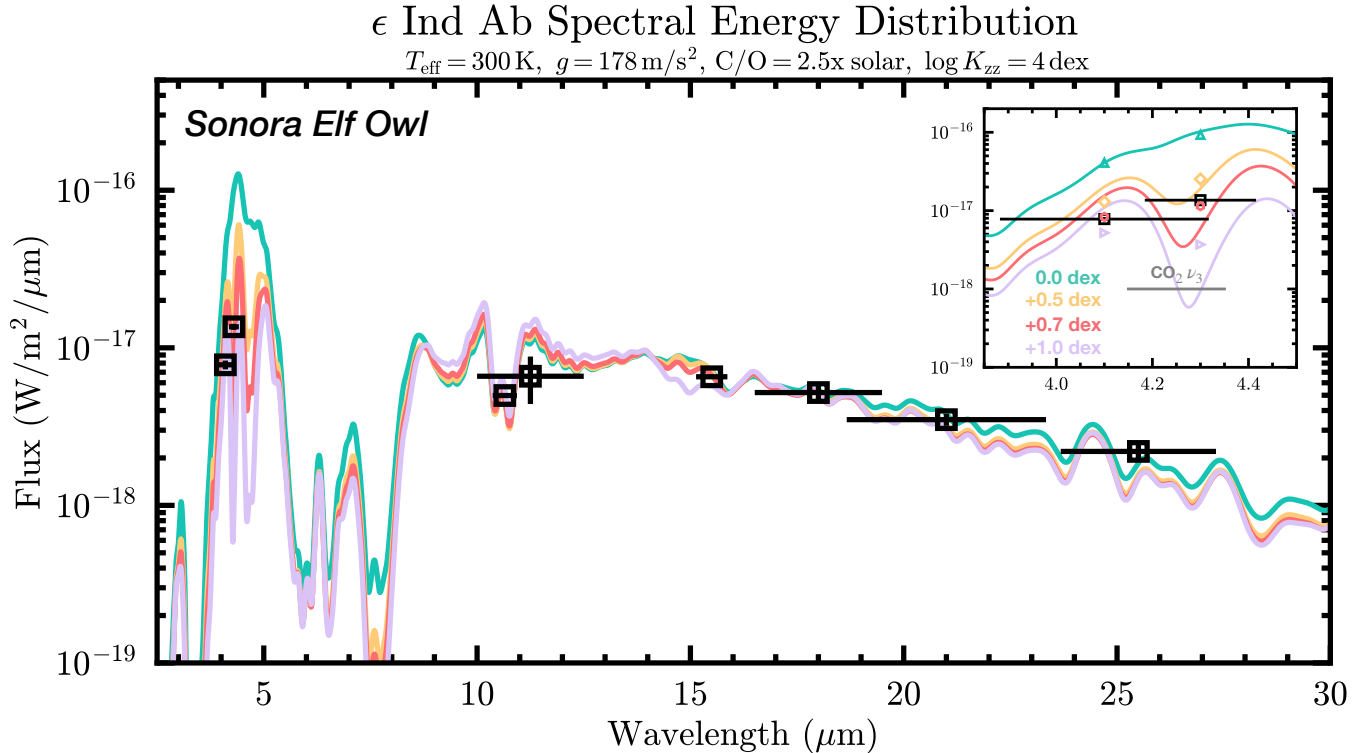


Figure 10. Example Sonora Elf Owl model spectra for varying atmospheric metallicities (colored lines, binned to $R \sim 50$), keeping parameters listed in the title fixed to the values corresponding to the lowest χ^2_ν model consistent with the dynamical mass within 3σ (bolded entry in Table 5). Each model is scaled to minimize the χ^2_ν with respect to the $> 10 \mu\text{m}$ photometry only. Black squares correspond to the measured ϵ Ind Ab photometry. The inset panel is a zoom-in view of the 4–5 μm region with synthetic F410M/F430M photometry from each model. A metal-enriched atmosphere increases the strength of the CO_2 absorption feature and can explain the observed flux suppression.

shows that the estimate is in agreement with the mass-metallicity relation (W. O. Balmer et al. 2025b).

From the atmospheric model fits, we find 45/63 of the models with $\chi^2_\nu < 10$ (Table 5) and 9/10 of the overall best-fitting (lowest χ^2_ν) models support an enhanced metallicity for ϵ Ind Ab. This is consistent with expectations from the giant planet mass-metallicity relation. The preference for a metal-enriched atmosphere can be attributed to the measured planet flux in F410M and F430M, which shows evidence for CO_2 absorption. The dependence of the strength of CO_2 absorption in the NIRCcam filters on atmospheric metallicity is visualized in Figure 10. These results highlight that atmospheric metallicity is a key parameter to consider when evaluating the NIRCcam detectability of cold gas giants (in addition to potential water clouds, see e.g., R. Bowens-Rubin et al. 2025).

4.2.4. Water Ice Clouds

Theoretical modeling suggests water vapor condenses into ice clouds in the atmospheres of the coolest extrasolar giant planets and brown dwarfs ($\lesssim 400 \text{ K}$; A. Burrows & C. M. Sharp 1999; M. S. Marley et al. 1999; A. Burrows et al. 2003; D. Sudarsky et al. 2003; A. Burrows et al. 2004; D. Sudarsky et al. 2005; C. V.

Morley et al. 2014b). As an example, water clouds are observed in Jupiter’s atmosphere (e.g., M. Sato & J. E. Hansen 1979; B. E. Carlson et al. 1992; D. Banfield et al. 1998). The presence of water clouds can suppress the emergent 4–5 μm planet flux due to their increasing optical thickness with decreasing planet temperature (e.g., C. V. Morley et al. 2014b; J. Mang et al. 2022; B. Lacy & A. Burrows 2023; J. Mang et al. 2024; R. Bowens-Rubin et al. 2025; A. Sanghi et al. 2026). Additionally, the depletion of water vapor in the upper atmosphere (through rainout or cloud formation) can modify the strength of mid-infrared water absorption bands (H. Kühnle et al. 2025). Given ϵ Ind Ab’s effective temperature is $\approx 275\text{--}300 \text{ K}$, its atmosphere is a candidate to host water ice clouds. We can frame our investigation around two possible questions.

(1) *Do the cloudy models fit the observed photometry better than the clear models?* Considering χ^2_ν for the various model fits, we find that the clear Sonora Elf Owl models better match the observed photometry compared to both the custom PICASO water cloud models and the B. Lacy & A. Burrows (2023) cloudy models (Table 5), though the difference in χ^2_ν is small

Table 6. Consistency of Best-fit Atmospheric Models with Observed ϵ Ind Ab Photometry

Model Grid	χ^2_{ν}	F410M (CO ₂)	F430M (CO ₂)	F1550C (CO ₂)	F1065C (NH ₃)	F1800W (H ₂ O)	F2100W (H ₂ O)	F2550W (H ₂ O)
Clear Models								
Sonora Elf Owl	1.16	✓ (0.3 σ)	× (−1.4 σ)	✓ (−0.5 σ)	× (1.7 σ)	✓ (0.2 σ)	✓ (0.7 σ)	× (1.5 σ)
Sonora Flame Skimmer	3.30	× (−3.1 σ)	✓ (−0.4 σ)	× (−1.3 σ)	× (3.2 σ)	✓ (−0.1 σ)	✓ (0.3 σ)	× (1.1 σ)
ATMO 2020	6.06	× (−2.6 σ)	✓ (0.6 σ)	× (5.3 σ)	× (−2.1 σ)	✓ (0.9 σ)	✓ (−0.02 σ)	× (1.3 σ)
ATMO 2020++ (PH ₃ Removed)	2.47	✓ (−0.3 σ)	× (−3.2 σ)	× (1.5 σ)	✓ (−0.8 σ)	✓ (0.6 σ)	✓ (0.7 σ)	× (1.8 σ)
ATMO 2020++ (PH ₃ Included)	2.94	× (2.0 σ)	✓ (0.5 σ)	× (−1.7 σ)	× (2.1 σ)	✓ (0.3 σ)	× (1.5 σ)	× (2.5 σ)
Water Cloud Models								
Custom PICASO Cloudy Model	3.38	✓ (0.2 σ)	× (2.5 σ)	✓ (0.5 σ)	× (−1.8 σ)	✓ (−0.5 σ)	× (−3.1 σ)	× (−2.0 σ)
B. Lacy & A. Burrows (2023)	1.50	× (−1.3 σ)	× (−2.3 σ)	× (1.7 σ)	✓ (−0.5 σ)	✓ (0.3 σ)	✓ (−0.5 σ)	✓ (0.1 σ)

NOTE—The dominant molecular absorber affecting each filter is noted in parentheses below the filter name. Models within 1 σ of the observed photometry in a given filter are marked with a ‘✓’. The difference is reported as (observed − model)/uncertainty in parentheses next to the checkmark or cross.

in the latter case. It is also worth noting that no single value of the f_{sed} parameter is strongly preferred in the model fits.

(2) *Are there systematic trends in the flux residuals for clear vs cloudy model fits?* The presence of clouds can affect the observed strength of molecular absorption features. In such a scenario, clear models may systematically under- or over-estimate the flux in certain photometric bandpasses. To investigate this, we evaluate the consistency (within 1 σ) of both the best-fit clear and cloudy models with individual filter photometry. The results are presented in Table 6.

First, we find that no single model matches all three CO₂ dominated bandpasses (F410M, F430M, and F1550C) within 1 σ . There does not appear to be a systematic trend of flux under- or over-estimation between the clear and cloudy model fits that are discrepant with the observed photometry in these bandpasses. The inconsistency (at 1 σ level) in at least one bandpass is statistically expected and also reflects the challenge of disentangling degeneracies between the effects of metallicity, disequilibrium chemistry, and clouds at these wavelengths (e.g., C. V. Morley et al. 2014b; S. Mukherjee et al. 2024; K. A. Crotts et al. 2025; D. C. B. Gagliuffi et al. 2025; A. Sanghi et al. 2026).

Second, the F1065C photometry (bandpass dominated by NH₃) is not well-fit by the majority of models. If we exclude the ATMO 2020 model (which has the worst overall fit among all grids), we observe that the inconsistent clear models systematically underestimate the F1065C flux, i.e., predict stronger NH₃ absorption than observed. The cloudy B. Lacy & A. Burrows (2023) model does improve the consistency to within 1 σ but the PICASO cloudy model overshoots and instead predicts weaker NH₃ absorption than observed. Overall, given that one of the ATMO2020++ clear models is still consistent with the observed photometry, it is un-

clear whether clouds are solely responsible for the discrepancy in F1065C photometry with the other clear models.

Third, among the H₂O dominated bandpasses, we find that the F1800W and F2100W photometry are well-fit by the majority of models but the F2550W photometry is inconsistent at the 1 σ level with all clear models (which also include models incorporating water condensation through rainout chemistry). Specifically, all the clear models systematically underestimate the F2550W flux, i.e., predict stronger H₂O absorption than observed. The custom PICASO water cloud model shows the opposite behavior, predicting weaker H₂O absorption than observed. The only model that is within 1 σ of the F2550W photometry is the cloudy B. Lacy & A. Burrows (2023) model (Figure 11).

Fourth, we consider the fit of the custom PICASO cloudy model, the Sonora Flame Skimmer (clear, with rainout chemistry), and the Sonora Elf Owl (clear, no rainout chemistry) model in more detail (Figure 11). The water clouds in the PICASO model lead to high suppression of F430M flux (stronger than observed), redistributing it to longer wavelengths and making the planet brighter than observed in F1065C, F2100W and F2550W. However, the clear Sonora Elf Owl model shows the opposite behavior, there is not enough flux suppression in the F430M filter and the planet is fainter in both F1065C and F2550W than observed. This indicates that there may be an intermediate solution, for example, one with patchy water clouds (e.g., C. V. Morley et al. 2014a,b), that can consistently explain all the photometry points. Indeed, patchy clouds may be a more realistic scenario for cold giant planets, analogous to the spatially heterogeneous band structures observed on Jupiter (B. E. Carlson et al. 1992; M. Roos-Serote et al. 2004; J. Arregi et al. 2006). The current PICASO models all assume 100% atmospheric cloud coverage fraction. We also find that the clear, rainout chemistry Sonora

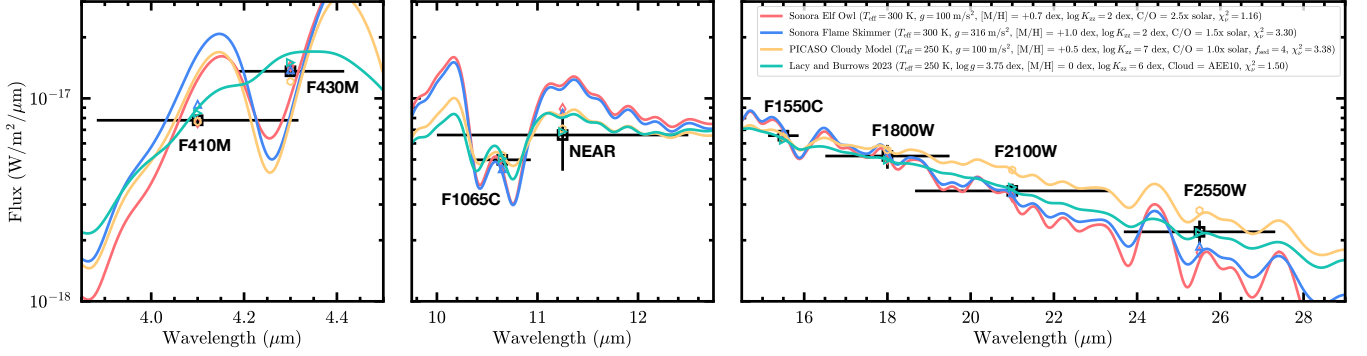


Figure 11. Comparison between the best-fit clear Sonora Elf Owl model (red), clear rainout chemistry Sonora Flame Skimmer model (blue), cloudy PICASO model (yellow), and cloudy B. Lacy & A. Burrows (2023) (green) model (binned to $R \sim 50$). Black squares correspond to the observed photometry for ϵ Ind Ab. Synthetic model photometry are marked with diamond (Sonora Elf Owl), top-facing triangle (Sonora Flame Skimmer), hexagon (PICASO), and right-facing triangle (B. Lacy & A. Burrows 2023) symbols.

Flame Skimmer model improves the fit to the F2550W photometry over the clear Sonora Elf Owl model (from 1.5σ to 1.1σ , Figure 11 and Table 6). This indicates that water condensation may play a role in the chemistry of ϵ Ind Ab’s upper atmosphere.

Finally, we highlight that the B. Lacy & A. Burrows (2023) models and the PICASO models are two independent parameterized water cloud models and differences in quality-of-fit are likely due to varying model assumptions. While the B. Lacy & A. Burrows (2023) cloudy model provides an excellent fit to the flux in the NH_3 and H_2O dominated bandpasses, it does not explain the flux in the CO_2 dominated bandpasses well.

To summarize, we consider the results from fitting self-consistent grid models to ϵ Ind Ab’s photometry inconclusive as to the presence or absence of water clouds. While trends observed with the F2550W photometry and a comparison of the best-fit Sonora Elf Owl, Sonora Flame Skimmer, and cloudy PICASO models hint at the possibility of water clouds or rainout depletion in ϵ Ind Ab’s atmosphere, we do not find any statistically incontrovertible signatures. Water clouds are not detected in a retrieval analysis of WISE 0855’s NIR-Spec+MIRI spectrum (H. Kühnle et al. 2025), which has a similar effective temperature, and plausibly similar surface gravity ($\log g = 3.5\text{--}4.5$ dex in cgs units, B. E. Miles et al. 2020), as ϵ Ind Ab. However, H. Kühnle et al. (2025) do find evidence for water depletion in WISE 0855’s upper atmosphere based on the strength of the water absorption bands in the MIRI MRS spectrum. The photometric results presented here motivate and pave the way for a similar analysis with the MIRI MRS spectrum of ϵ Ind Ab acquired as part of the same JWST observing program (#8714).

4.2.5. Disequilibrium Chemistry

There is strong evidence that disequilibrium processes impact Solar System gas giant and cool substellar at-

mospheres (e.g., B. Fegley & R. G. Prinn 1985; K. S. Noll et al. 1997; D. Saumon et al. 2006; S. K. Leggett et al. 2007; K. L. Luhman et al. 2023). The increasing strength of CO absorption in the 4–5 μm region is a signature of vertical mixing in the atmosphere (B. E. Miles et al. 2020; S. Mukherjee et al. 2024; W. O. Balmer et al. 2025a). In this case, the atmospheric model fits for ϵ Ind Ab do not find a clear preference for any single value of $\log K_{zz}$. This is not surprising as our F410M/F430M photometry do not cover the 4.5–4.8 μm CO feature. The JWST/NIRSpec spectrum of ϵ Ind Ab, acquired as part of the same program (#8714), and to be presented in a future paper, should provide better constraints on $\log K_{zz}$.

4.2.6. Bolometric Luminosity of ϵ Ind Ab

The multi-wavelength photometry of ϵ Ind Ab enables a calculation of the planet’s bolometric flux (F_{bol}) by directly integrating the complete near- to mid-infrared spectral energy distribution (SED) (e.g., J. C. Filipazzo et al. 2015; A. Sanghi et al. 2023). Combining the bolometric flux with the known parallactic distance (d) yields the bolometric luminosity ($L_{\text{bol}} = F_{\text{bol}} \cdot 4\pi d^2$). We note that the uncertainty in the parallactic distance is at least an order of magnitude smaller than the uncertainty in F_{bol} , which is discussed below.

The F_{bol} derived from a photometric SED relies on the use of atmosphere models to estimate flux contributed at wavelengths not covered by the photometry. The two sources of uncertainty in F_{bol} are the observational uncertainties in the photometry and the model-contributed uncertainty. The model-contributed uncertainty arises from variations in the flux (not covered by the photometry) calculated from distinct models that can explain the observed photometry (model spectra have no intrinsic uncertainty). In the case of ϵ Ind Ab, we can account for both uncertainty sources by estimating the bolometric flux using all atmosphere models that fit the observed photometry with $\chi^2_{\nu} < 10$ (Table 5). This choice of the

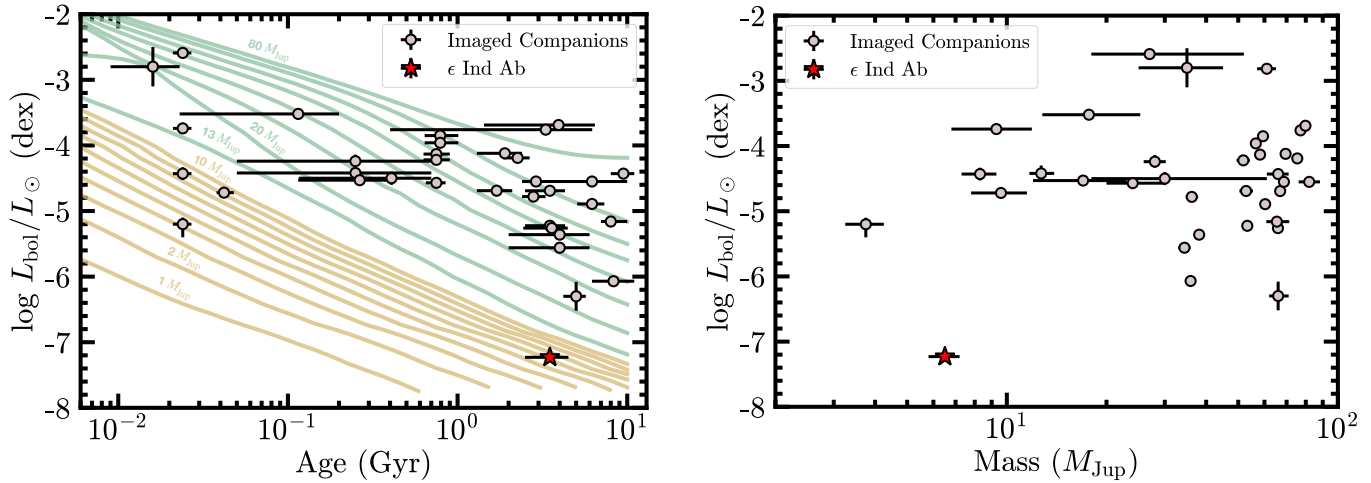


Figure 12. Imaged substellar companions with dynamical masses, bolometric luminosities, and age constraints. Based on data compiled by Y. Li et al. (2025, see their Table 8). We show the bolometric luminosity vs age (left) with isomass cooling tracks from the G. Chabrier et al. (2023) evolutionary models and the bolometric luminosity vs mass (right). ϵ Ind Ab uniquely populates a previously unexplored parameter space of low mass, low luminosity, and old age.

χ^2_ν threshold translates to a requirement that, on average, the synthetic model photometry is within $\approx 3\sigma$ of the measured value. Thus, this method incorporates the observed photometric uncertainties. By calculating F_{bol} using models spanning the seven different grids considered (Table 4) that satisfy the above criterion, we are also accounting for the model-contributed uncertainty.

Given a model spectrum fit to the data with $\chi^2_\nu < 10$, the bolometric flux is determined by directly integrating the model spectrum across its full wavelength range. The model coverage on the short wavelength end is sufficient ($\gtrsim 0.1 \mu\text{m}$) to capture the flux contribution accurately (the flux of the planet rapidly drops shortward of $4 \mu\text{m}$). However, on the long wavelength end, several models cut-off at $\lambda \sim 30 \mu\text{m}$. To estimate the flux in the tail, we integrate a blackbody spectrum with the same effective temperature and radius as the fit model spectrum from the cut-off wavelength to an arbitrarily large wavelength ($10^6 \mu\text{m}$). This is a good approximation as we are in the Rayleigh-Jeans limit at these wavelengths. The two contributions are added to obtain F_{bol} and thus, L_{bol} (noted in Table 5). We adopt the mean and standard deviation of the individual L_{bol} estimates as our final measurement, $\log L_{\text{bol}}/L_\odot = -7.23 \pm 0.03$ dex (corresponds to $\approx 7\%$ uncertainty in L_{bol}), where $L_\odot = 3.828 \times 10^{26}$ W (E. E. Mamajek et al. 2015).

While the estimated L_{bol} is not independent of the atmosphere models, we highlight that the observed JWST photometry captures a significant fraction, $\approx 40\%$, of the total flux. The model contribution is $\approx 30\%$ between $4.4\text{--}10.3 \mu\text{m}$, $\approx 20\%$ between $12\text{--}15 \mu\text{m}$, and $\approx 10\%$ in the tail beyond $28 \mu\text{m}$. The overall consistency of L_{bol} calculated using different atmosphere models, as indicated by the small L_{bol} uncertainty, shows that the

estimate is robust for comparisons to predictions from evolutionary models in the following section.

5. EVOLUTIONARY MODEL ANALYSIS

Evolutionary models are a critical and widely-used tool to infer substellar fundamental properties from observables. Our new dynamical mass ($M_{\text{obs}} = 6.5 \pm 0.7 M_{\text{Jup}}$) and bolometric luminosity ($L_{\text{obs}} = -7.23 \pm 0.03$, expressed as $\log L_{\text{bol}}/L_\odot$), combined with existing estimates of the stellar age ($t_{\text{obs}} = 3.5 \pm 1.0$ Gyr), make ϵ Ind Ab the first planet to serve as a model benchmark in a new regime of low luminosities (cold temperatures) and old ages (Figure 12). Two evolutionary model grids covering the (mass, age, luminosity) of ϵ Ind Ab are considered for the following analysis.

Sonora Bobcat. Sonora Bobcat (M. S. Marley et al. 2021) builds upon the heritage D. Saumon & M. S. Marley (2008) “hybrid” evolutionary models and includes a number of advancements such as accounting for metals in the equation of state (EOS) to enable calculation of models for $[\text{M}/\text{H}] = \{-0.5, 0, +0.5\}$ dex and using improved nuclear-reaction screening factors (A. Y. Potekhin & G. Chabrier 2012). The self-consistently computed Sonora Bobcat model atmospheres serve as a boundary condition for the evolution models and include updated opacities (see their Table 2) and atmospheric chemistry.

G. Chabrier et al. (2023, CBPD2023) Models. The CBPD2023 evolution models are based on the Lyon stellar evolution code (G. Chabrier & I. Baraffe 1997; I. Baraffe et al. 1998, 2003) and incorporate the updated EOS for H-He mixtures from G. Chabrier & F. Debras

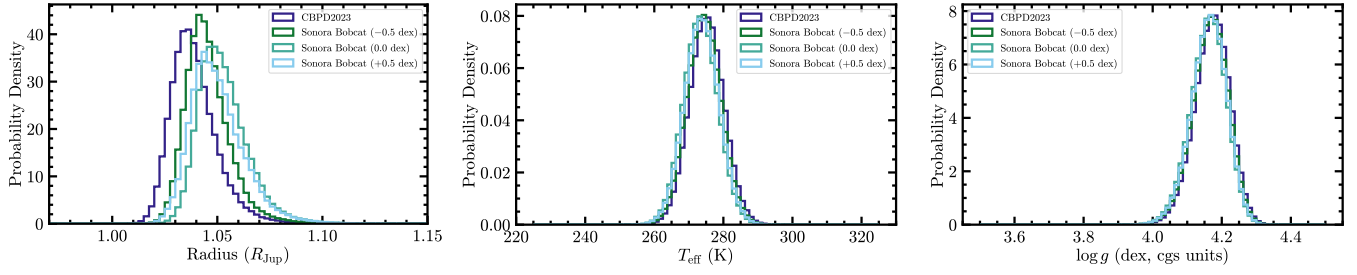


Figure 13. Posterior distributions for ϵ Ind Ab's radius (left), effective temperature (T_{eff} , center) and surface gravity (right) using the ATMO2020 and Sonora Bobcat evolutionary models given the planet's dynamical mass, age, and bolometric luminosity.

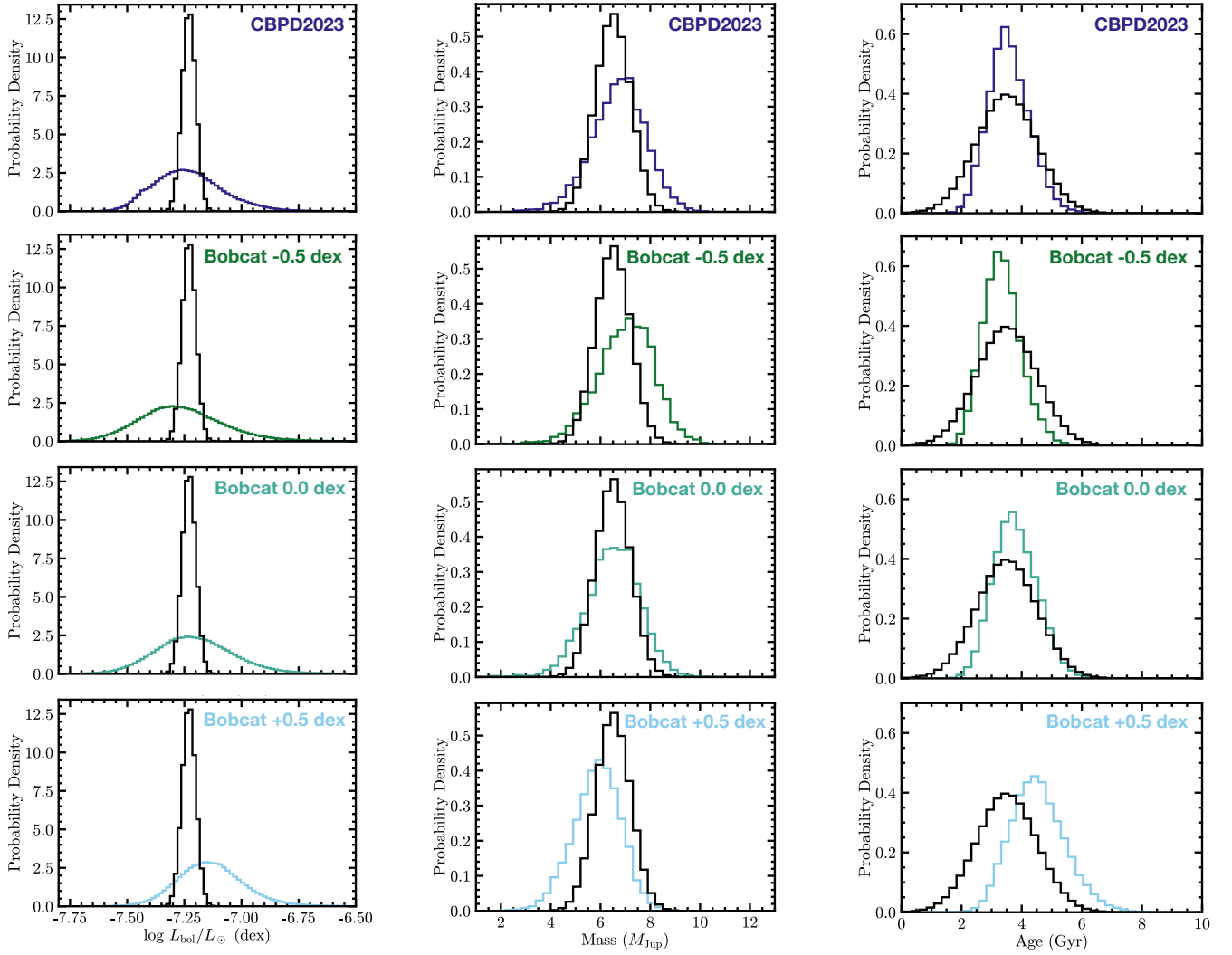


Figure 14. Comparison between ϵ Ind Ab's observed (black) and model-predicted (colored) bolometric luminosity (left), mass (center), and age (right). The observed and model-predicted parameters for ϵ Ind Ab are consistent with each other.

(2021)²⁷. The solar metallicity ATMO 2020 atmosphere models (M. W. Phillips et al. 2020) serve as a boundary condition for the CBPD2023 evolution models and include both expanded opacity (e.g., CH₄ and NH₃ from J. Tennyson & S. N. Yurchenko 2018) and chemistry.

5.1. Effective Temperature and Radius

Evolutionary models predict substellar radii as a function of mass, age, and metallicity. We can combine our empirical measurements of bolometric luminosity (L_{bol}) and mass (M) with evolutionary model-predicted radii to obtain effective temperature $T_{\text{eff}} = (L_{\text{bol}}/4\pi R^2 \sigma_{\text{SB}})^{1/4}$ and surface gravity $\log g = \log(GM/R^2)$. First, to derive the posterior distribution for ϵ Ind Ab’s radius, we draw 10^6 normally distributed random values for mass and age following their observational uncertainties. The evolutionary model grids are bilinearly interpolated at each (mass, age) point to obtain radius. Next, T_{eff} and $\log g$ are calculated using the posterior samples with the above equations. The resulting distributions are shown in Figure 13 and the 68% confidence intervals are reported in Table 7. We find ϵ Ind Ab’s radius is $\sim 1.05 R_{\text{Jup}}$, $T_{\text{eff}} \approx 275$ K, and $\log g \approx 4.17$ dex (cgs units). The T_{eff} is indeed similar to that of WISE0855 as was determined from the mid-infrared color comparison (§4.1).

5.2. Luminosity, Mass, Age Consistency Tests and Goodness-of-Fit

Given independent estimates of a planet’s luminosity, mass, and age, evolutionary models can infer any one of the three properties using the other two. This enables a direct consistency check between the observed and model-derived parameter estimate, testing substellar evolutionary models. To obtain the posterior distribution for luminosity (L_{mod} , expressed as $\log L_{\text{bol}}/L_{\odot}$), we first draw 10^6 normally distributed random values for mass and age following their observational uncertainties. The model grid is bilinearly interpolated at each (mass, age) point to obtain L_{mod} . To infer the posterior distribution for mass M_{mod} (resp. age t_{mod}) given observational measurements of age (resp. mass) and luminosity, we use the Bayesian rejection sampling technique (e.g., T. J. Dupuy & M. C. Liu 2017; A. Sanghi et al. 2023; T. J. Dupuy et al. 2023; S. A. Hurt et al. 2024; Y. Li et al. 2025). We begin by drawing 10^6 uniformly distributed mass (resp. age) samples across the full range available in the model grid and 10^6 normally distributed age (resp. mass) samples following the observational uncertainty. The model grid is bilinearly interpolated at

each (mass, age) point to derive L_{mod} . We compute χ^2 for each sample,

$$\chi^2 = \frac{(L_{\text{obs}} - L_{\text{mod}})^2}{\sigma_{L_{\text{obs}}}^2}. \quad (1)$$

The χ^2 for each sample is converted to a probability p , normalizing by the sample with minimum χ^2 as follows,

$$p = \exp \left[-\frac{1}{2}(\chi^2 - \chi_{\text{min}}^2) \right]. \quad (2)$$

Next, we randomly draw 10^6 uniformly distributed variates (u) in range from 0 to 1 and reject any mass (resp. age) samples where $p < u$. The remaining samples determine M_{mod} (resp. t_{mod}). Figure 14 presents a comparison of the observed and model-predicted posterior distributions for each of the three fundamental parameters. Additionally, Table 7 provides the 68% confidence interval for the parameter bias (observed value – model prediction). Overall, we find excellent agreement between the observed and model-derived luminosity, mass, and age of ϵ Ind Ab. The median bias in each parameter (M , L , t) is within the observed value’s 1σ uncertainty (with the exception of the +0.5 dex Sonora Bobcat model, which has a larger bias in luminosity).

A generalized goodness-of-fit metric that can be calculated between the models and the observation is the Mahalanobis distance D^2 (P. C. Mahalanobis 1930). The evolutionary models are two-dimensional manifolds in the three dimensional parameter space of mass, age, and luminosity. D^2 evaluates how close the observed (mass, age, luminosity) value for ϵ Ind Ab lies to the model manifold and reduces to the χ^2 metric in the absence of correlations between the three quantities. This is a reasonable assumption in our case (e.g., Y. Li et al. 2025) since the parallax uncertainty is negligible. This analysis is distinct from the consistency tests previously discussed as it does not fix the value of any of the three observables. First, we bilinearly interpolate the evolutionary model over a fine grid of $M \in [1, 20] M_{\text{Jup}}$ and $t \in [0.1, 10]$ Gyr to determine luminosity. We compute D^2 between $(M_{\text{obs}}, t_{\text{obs}}, L_{\text{obs}})$ and each interpolated (mass, age, luminosity) point on the model manifold to determine the minimum distance D_{min}^2 . Given $D^2 \sim \chi^2$ (1 degree of freedom; Y. Li et al. 2025), we can calculate the two-sided tail probability p that a random draw from this distribution exceeds D_{min}^2 using the corresponding survival function. Finally, the probability p is converted to an equivalent Gaussian σ using the inverse survival function of a standard normal distribution. The D^2 value for each model is $< 1\sigma$ (Table 7) and supports the conclusion that the evolutionary model predictions are consistent with the ϵ Ind Ab observations.

As the next generation of evolutionary models including a wider array of physical processes are developed (e.g., A. Sur et al. 2025), ϵ Ind Ab will serve as a critical benchmark at cold temperatures and old ages.

²⁷ Note that the CBPD2023 models are distinct from the ATMO 2020 evolution models (M. W. Phillips et al. 2020), which use the G. Chabrier et al. (2019) EOS. The CBPD2023 models are labeled as “ATMO_2020_neweos_update” on <https://noctis.erc-atmo.eu/fsdownload/zyU96xA6o/phillips2020>.

Table 7. Evolutionary Model Analysis for ϵ Ind Ab

Evolutionary Model	Radius (R_{Jup})	T_{eff} (K)	$\log g$ (dex, cgs)	$L_{\text{obs}} - L_{\text{mod}}(M_{\text{obs}}, t_{\text{obs}})$ (dex)	$M_{\text{obs}} - M_{\text{mod}}(L_{\text{obs}}, t_{\text{obs}})$ (M_{Jup})	$t_{\text{obs}} - t_{\text{mod}}(L_{\text{obs}}, M_{\text{obs}})$ (Gyr)	D^2
CBPD2023	$1.038^{+0.012}_{-0.009}$	275 ± 5	4.17 ± 0.05	$0.01^{+0.14}_{-0.16}$	$-0.27^{+1.31}_{-1.29}$	$-0.07^{+1.19}_{-1.21}$	0.08σ
Sonora Bobcat (-0.5 dex)	$1.044^{+0.008}_{-0.011}$	274 ± 5	4.17 ± 0.05	$0.04^{+0.17}_{-0.19}$	$-0.5^{+1.4}_{-1.2}$	0.15 ± 1.18	0.26σ
Sonora Bobcat (0.0 dex)	$1.051^{+0.013}_{-0.009}$	273 ± 5	4.16 ± 0.05	$-0.02^{+0.16}_{-0.18}$	$-0.006^{+1.283}_{-1.246}$	$-0.27^{+1.21}_{-1.24}$	0.10σ
Sonora Bobcat (+0.5 dex)	$1.048^{+0.014}_{-0.010}$	274 ± 5	4.16 ± 0.05	$-0.09^{+0.14}_{-0.15}$	$0.6^{+1.2}_{-1.1}$	$-1.07^{+1.33}_{-1.35}$	0.62σ

NOTE.—The reported parameter estimates correspond to the 68% confidence interval. For the evolutionary model comparisons, we use $L_{\text{obs}} = -7.23 \pm 0.03$ dex (expressed as $\log L_{\text{bol}}/L_{\odot}$), $M_{\text{obs}} = 6.5 \pm 0.7 M_{\text{Jup}}$, $t_{\text{obs}} = 3.5 \pm 1.0$ Gyr. Note that the above estimates do not account for potential systematic uncertainties arising from the treatment of heavy metals, their distribution in the interior, the adopted atmospheric boundary conditions, and the influence of fuzzy cores (e.g., A. Sur et al. 2025).

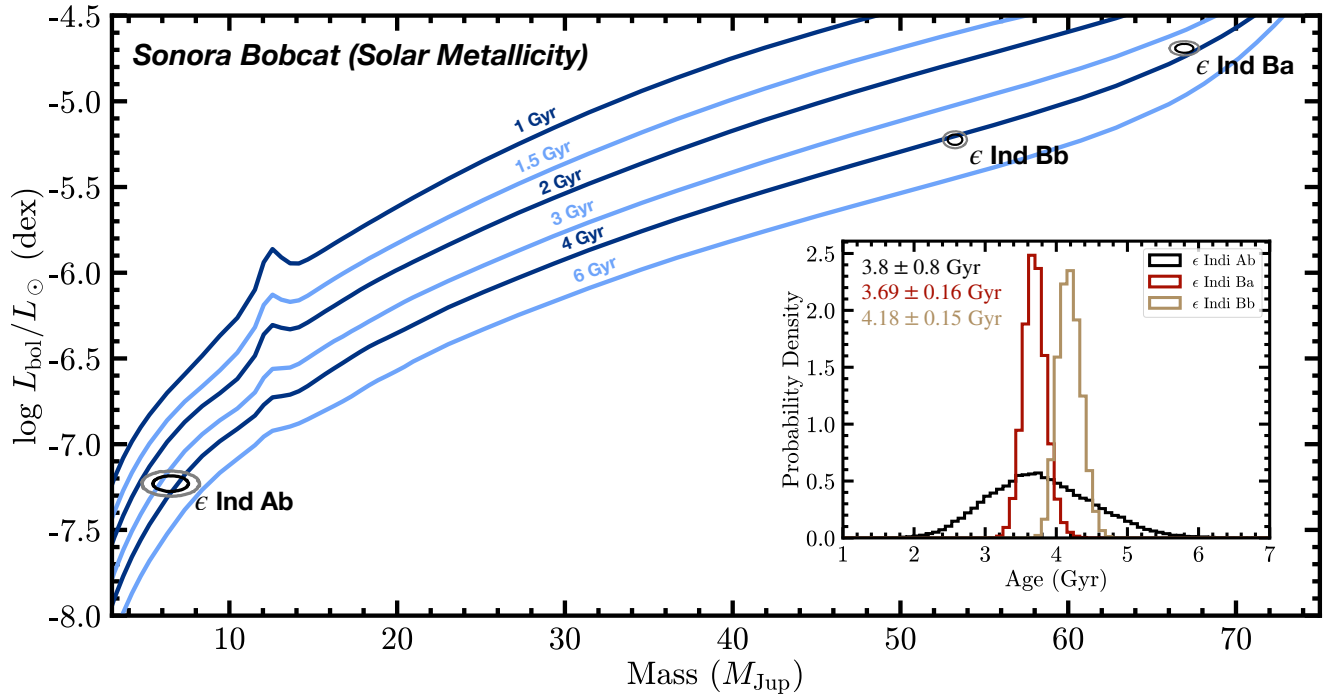


Figure 15. Isochrones (light and dark blue) from the solar metallicity Sonora Bobcat evolutionary models ranging from 1 to 6 Gyr. Black and gray contours show the joint 1σ and 2σ confidence intervals of the masses and luminosities of ϵ Ind Ab, ϵ Ind Ba, and ϵ Ind Bb. All three objects are expected to be coeval and, indeed, remarkably, lie along a single isochrone (4 Gyr). The inset figure shows the posterior distribution for system age derived with the solar metallicity Sonora Bobcat model using the dynamical mass and observed luminosity of each of the three objects.

5.3. Coevality of the ϵ Ind Substellar Objects

The ϵ Ind system additionally hosts the binary brown dwarfs ϵ Ind Ba and ϵ Ind Bb. [M. Chen et al. \(2022\)](#) noted that the ϵ Ind B binary represents a rare case where one can test coevality of the two objects using model isochrones, given their precise dynamical mass and bolometric luminosity measurements. Now, with the addition of the above measurements for ϵ Ind Ab in this work, ϵ Ind is truly unique among benchmark systems, amenable to a coevality test over two orders of magnitude in luminosity and one order of magnitude in mass.

[M. Chen et al. \(2022\)](#) demonstrated that only the [D. Saumon & M. S. Marley \(2008\)](#) “hybrid” evolutionary models yielded consistent cooling ages for the two brown dwarfs (but predict an older age, ~ 5 Gyr, at odds with observational determinations). Analysis of the brown dwarf binary with the CBPD2023 models is presented in [G. Chabrier et al. \(2023\)](#). The CBPD2023 models do not satisfy coevality but the cooling ages inferred for the two brown dwarfs are consistent with the observational age estimate within uncertainties. Here, we consider the Sonora Bobcat models for the coevality test. Overplotting the observed masses and luminosities of the ϵ Ind substellar objects on the Sonora Bobcat solar metallicity model isochrones, we find that all three companions, remarkably, lie approximately along the 4 Gyr isochrone ([Figure 15](#)).

For a quantitative comparison, we derive the age posterior from the observed mass and luminosity measurements of each object following the rejection sampling procedure in [§5.2](#). ϵ Ind Ab’s cooling age is consistent within 1σ with those of the binary brown dwarfs ([Figure 15](#)). The uncertainty in ϵ Ind Ab’s dynamical mass dominates the uncertainty in the cooling age. The median cooling ages for the two brown dwarfs are more broadly consistent at the 3σ level ([Figure 15](#)). The cooling ages of all three objects are consistent with the observational estimate of 3.5 ± 1.0 Gyr for the host star ([M. Chen et al. 2022](#)). Investigating the larger difference between the cooling ages of the two brown dwarfs is beyond the scope of this work (and is the goal of JWST program #5765, PI: E. Matthews), however, we note that improved consistency requires the slope of the M - L relation in Sonora Bobcat to be steeper ([Figure 15](#)). The metal poor and metal rich Sonora Bobcat models result in a larger discrepancy in the cooling ages between the two brown dwarfs (but not ϵ Ind Ab, as shown in the previous section) and are thus not presented here.

6. CONCLUSIONS

In this work, we assembled the first 4–25 μm spectral energy distribution for a cold (< 300 K) exoplanet using new JWST/NIRCam 4–5 μm and JWST/MIRI 18–25 μm imaging of the super-Jupiter ϵ Ind Ab. Our main conclusions are summarized below:

1. ϵ Ind Ab is detected at a separation of $\approx 3.5''$, position angle of $\approx 35^\circ$ East of North, and $S/N = \{17.9, 25.4, 7.7, 14.3, 7.5\}$ in $\{F410M, F430M, F1800W, F2100W, F2550W\}$, respectively. The MIRI detections were obtained without a coronagraph and using archival observations to construct a reference library for PSF subtraction.
2. We performed a comprehensive re-analysis of ϵ Ind Ab’s orbit with the new high-precision NIRCam astrometry. Our joint RV, absolute astrometry, and relative astrometry model used the framework of observable-based priors to reduce biases in fitting the relative astrometry data, mitigated the impact of stellar activity in the RV time series with a Gaussian process, and accounted for non-linear effects such as secular acceleration. We estimated $M_{\text{Ab}} = 6.5_{-0.6}^{+0.7} M_{\text{Jup}}$, $a = 15.8_{-1.4}^{+1.7}$ au, $e = 0.25 \pm 0.09$, and $i = 102.2^\circ \pm 1.7^\circ$. Additionally, we found that the lack of stellar activity modeling for the RV data biased previous orbital solutions for ϵ Ind Ab.
3. An initial comparison between the SED of the coldest Y-dwarf (~ 285 K) WISE 0855 and ϵ Ind Ab yielded similar F1800W–F1550C color, and thus, effective temperature, for the two objects. We confirmed suppression of the 4–5 μm flux, compared to WISE 0855, in ϵ Ind Ab’s atmosphere. This was hinted by non-detection of the planet in ground-based imaging.
4. Fitting self-consistent atmospheric models (both clear and cloudy, across multiple grids) to ϵ Ind Ab’s SED, we found a preference for enhanced atmospheric metallicity, consistent with expectations from the giant planet mass-metallicity relation (which predicted $[M/H] = 0.4 \pm 0.1$ dex, assuming a well-mixed interior). This preference is driven by the measured F410M and F430M photometry, which indicate an elevated CO_2 abundance in the atmosphere compared to expectations from solar metallicity models. No constraint is obtained on the strength of disequilibrium chemistry in the atmosphere since our photometry do not cover the 4.5–4.8 μm CO feature.
5. We did not find definitive evidence for the presence or absence of water ice clouds in ϵ Ind Ab’s atmosphere. The overall best-fit atmospheric model was a clear Sonora Elf Owl model ($\chi_\nu^2 = 1.16$), though a cloudy [B. Lacy & A. Burrows \(2023\)](#) model also agreed well with the photometry ($\chi_\nu^2 = 1.50$). Notably, the F2550W flux (affected by H_2O vapor absorption) was systematically underestimated ($>1\sigma$, but $< 2\sigma$) by all clear and rainout chemistry models. Only a cloudy [B. Lacy & A. Burrows \(2023\)](#) model could explain the F2550W

flux within 1σ . This should be investigated further using ϵ Ind Ab’s MIRI/MRS spectrum.

6. By directly integrating ϵ Ind Ab’s SED, we estimated a bolometric luminosity $\log L_{\text{bol}}/L_{\odot} = -7.23 \pm 0.03$ dex for the planet. The observed photometry accounts for 40% of the bolometric luminosity and the quoted error bar incorporates the model-contributed uncertainty.
7. Using the Sonora Bobcat and G. Chabrier et al. (2023) evolutionary models, we estimated ϵ Ind Ab’s $R \approx 1.05 R_{\text{Jup}}$, $T_{\text{eff}} \approx 275$ K, and $\log g \approx 4.17$ dex. Combining the planet’s dynamical mass, bolometric luminosity, and age (3.5 ± 1.0 Gyr), we conducted the first test of substellar evolution models in a new regime of low masses, low luminosities, and old ages. All three measurements were in excellent agreement ($< 1\sigma$) with model predictions. We also showed that the Sonora Bobcat models agree with ϵ Ind Ab, ϵ Ind Ba, and ϵ Ind Bb being co-eval objects.

The addition of a precise dynamical mass and bolometric luminosity for ϵ Ind Ab establishes the ϵ Ind system as a unique benchmark for substellar evolution studies at temperatures and ages more similar to that of Jupiter in our own Solar System. Upcoming medium-resolution JWST/NIRSpec and MIRI MRS spectroscopy of ϵ Ind Ab will measure elemental and isotopic abundances in its atmosphere and investigate the relative importance of different accretion processes operating during gas giant formation. More broadly, this work sets the stage for the detailed characterization of a rapidly expanding sample of imaged extremely cold worlds ($\lesssim 300$ K): the α Cen Ab candidate (K. Wagner et al. 2021; C. Beichman et al. 2025; A. Sanghi et al. 2025), TWA 7b (A.-M. Lagrange et al. 2025; K. A. Crotts et al. 2025), 14 Her c (D. C. B. Gagliuffi et al. 2025), and the candidate/confirmed planets orbiting white dwarfs (M. A. Limbach et al. 2024, 2025).

ACKNOWLEDGMENTS

The author thanks William Balmer, Jorge Llop-Sayson, and Rodrigo Ferrer-Chavez for discussions on JWST/NIRCam data processing, Rachel Bowens-Rubin and Kevin Stevenson for their guidance on using the MAGIC pipeline for JWST/MIRI data reduction, Helena Kühnle for sharing their reduced MIRI MRS spectrum of WISE 0855, Floor van Leeuwen, Clarissa R. Do Ó, Quang Tran, and Kareem El-Badry for helpful discussions on orbit modeling, and Michael Liu, Trent Dupuy, and Yaguang Li for productive conversations on the evolutionary model analysis. We are grateful for the support of Dean Hines, Julien Girard, and the STScI planning and operations team in scheduling and executing this program. A.S acknowledges support from

the National Science Foundation Graduate Research Fellowship under Grant No. 2139433. J.W.X is grateful for support from the Heising-Simons Foundation 51 Pegasi b Fellowship (grant #2025-5887). J.M. acknowledges support from the National Science Foundation Graduate Research Fellowship Program under Grant No. DGE 2137420.

This publication makes use of The Data & Analysis Center for Exoplanets (DACE), which is a facility based at the University of Geneva (CH) dedicated to extra-solar planets data visualisation, exchange and analysis. DACE is a platform of the Swiss National Centre of Competence in Research (NCCR) PlanetS, federating the Swiss expertise in Exoplanet research. The DACE platform is available at <https://dace.unige.ch>. This publication makes use of VOSA, developed under the Spanish Virtual Observatory (<https://svo.cab.inta-csic.es>) project funded by MCIN/AEI/10.13039/501100011033/through grant PID2020-112949GB-I00. VOSA has been partially updated by using funding from the European Union’s Horizon 2020 Research and Innovation Programme, under grant Agreement #776403 (EXOPLANETS-A). The computations presented here were conducted in the Resnick High Performance Computing Center, a facility supported by Resnick Sustainability Institute at the California Institute of Technology.

AUTHOR CONTRIBUTIONS

A. Sanghi led the overall analysis and writing and submission of this manuscript. A. Sanghi and J. Xuan designed the NIRCam and MIRI imaging observations. J. Xuan led the JWST proposal and facilitated interpretation of the results. W. Thompson conducted an initial investigation of the planet’s orbit and advised A. Sanghi on the orbit fitting. J. Mang generated the Sonora Flame Skimmer and custom PICASO atmospheric models used in this work and contributed to interpreting the model fits. All authors assisted with the preparation of the original JWST proposal and/or provided feedback on the manuscript.

Facilities: JWST(NIRCam), JWST(MIRI), Hipparcos, Gaia

Software: `astropy` (Astropy Collaboration et al. 2013, 2018, 2022), `matplotlib` (J. D. Hunter 2007), `numpy` (C. R. Harris et al. 2020), `pandas` (W. McKinney 2010; T. p. d. team 2025), `python` (G. Van Rossum & F. L. Drake 2009), `scipy` (P. Virtanen et al. 2020; R. Gommers et al. 2023), `astroquery` (A. Ginsburg et al. 2019, 2024), `scikit-image` (S. van der Walt et al. 2014), `STPSF` (M. D. Perrin et al. 2012, 2014), `jwst` (H. Bushouse et al. 2025), `pyKLIP` (J. J. Wang et al. 2015), `vip` (C. A. Gomez Gonzalez et al. 2017; V. Christiaens et al. 2023), `spaceKLIP` (J. Kammerer et al. 2022; A. L. Carter et al. 2023; A. Carter et al. 2025), `emcee` (D.

Foreman-Mackey et al. 2013), `webbpsf_ext` (J. Leisenring 2025), `PICASO` (N. E. Batalha et al. 2019; S. Mukher-

jee et al. 2023), and `Virga` (N. Batalha et al. 2020a; N. E. Batalha et al. 2025; S. E. Moran et al. 2025).

APPENDIX

A. MIRI IMAGING REFERENCE LIBRARY

Table A1 presents the archival observations used to construct a PSF library for MIRI PSF subtraction.

Table A1. MIRI PSF Library

Program	Target Name	Filters	Detector (x, y) ^a	Dithers	Reference
COM 1024	2MASS J05220207-6930388 ^b	F1800W	(734, 827)	4	PI: Glasse, Alistair
COM 1024	2MASS J05220207-6930388 ^b	F1800W	(700, 928)	4	PI: Glasse, Alistair
COM 1024	2MASS J05220207-6930388 ^b	F1800W	(574, 456)	4	PI: Glasse, Alistair
COM 1027	BD+60 1753	F1800W	(806, 580)	4	PI: Garcia Marin, Macarena
GTO 1193	* del Eri	F1800W	(324, 346)	4	PI: Beichman, Charles A.
CAL 1523	HD 2811	F1800W	(70, 62)	4	PI: Law, David R.
CAL 1536	HD 180609	F1800W	(157, 115)	4	PI: Gordon, Karl D.
CAL 1536	HD 163466	F1800W	(60, 52)	4	PI: Gordon, Karl D.
CAL 1536	del UMi	F1800W	(49, 48)	4	PI: Gordon, Karl D.
CAL 1536	HD 163466	F1800W	(60, 52)	4	PI: Gordon, Karl D.
CAL 1538	HD 106252	F1800W	(50, 49)	4	PI: Gordon, Karl D.
CAL 1538	16 Cyg B	F1800W	(60, 52)	4	PI: Gordon, Karl D.
CAL 1538	HD 37962	F1800W	(49, 48)	4	PI: Gordon, Karl D.
COM 1024	2MASS J05220207-6930388 ^b	F2100W	(748, 830)	4	PI: Glasse, Alistair
COM 1024	2MASS J05220207-6930388 ^b	F2100W	(588, 459)	4	PI: Glasse, Alistair
COM 1024	2MASS J05220207-6930388 ^b	F2100W	(714, 931)	4	PI: Glasse, Alistair
COM 1027	BD+60 1753	F2100W	(807, 579)	4	PI: Garcia Marin, Macarena
GTO 1193	* del Eri	F2100W	(325, 346)	4	PI: Beichman, Charles A.
GTO 1194	HD 218261	F2100W	(170, 171)	4	PI: Beichman, Charles A.
GTO 1194	HR8799	F2100W	(197, 221)	4	PI: Beichman, Charles A.
GTO 1237	DIGELC1-A	F2100W	(644, 1005)	4	PI: Ressler, Michael E.
CAL 1523	HD 2811	F2100W	(78, 60)	4	PI: Law, David R.
GO 6122	Ross 154	F2100W	(200, 210)	4	PI: Bowens-Rubin, Rachel
GO 6122	Wolf 359	F2100W	(198, 209)	4	PI: Bowens-Rubin, Rachel
GTO 1193	* alf PsA ^c	F2550W	(324, 348)	4	PI: Beichman, Charles A.
GTO 1193	* alf PsA ^c	F2550W	(324, 346)	4	PI: Beichman, Charles A.
GTO 1193	* alf Lyr ^c	F2550W	(324, 346)	4	PI: Beichman, Charles A.
GTO 1193	* alf Lyr ^c	F2550W	(324, 348)	4	PI: Beichman, Charles A.
GTO 1193	* del Eri	F2550W	(325, 346)	4	PI: Beichman, Charles A.
GTO 1193	* 19 PsA	F2550W	(321, 349)	4	PI: Beichman, Charles A.
GTO 1193	HD 169305	F2550W	(324, 348)	4	PI: Beichman, Charles A.

^a Zero-indexed detector coordinates for the PSF in the stacked image after background subtraction with `MAGIC`.

^b Three distinct source PSFs are extracted from the full detector image.

^c Observations of the same target conducted at different times.

B. REVISITING THE PLANET'S ORIGINAL ORBITAL PREDICTION

The original prediction of ϵ Ind Ab's orbital location (F. Feng et al. 2023) was discrepant by a significant margin compared to the imaging discovery location (E. C. Matthews et al. 2024). Here, we perform a new RV + HGCA orbit fit considering only the data used in F. Feng et al. (2023) (i.e., no relative astrometry from imaging and only RVs captured before the JWST detection) and demonstrate that adopting a conservative circular orbit model would have yielded an accurate prediction of ϵ Ind Ab's location for the JWST direct imaging discovery epoch. For our

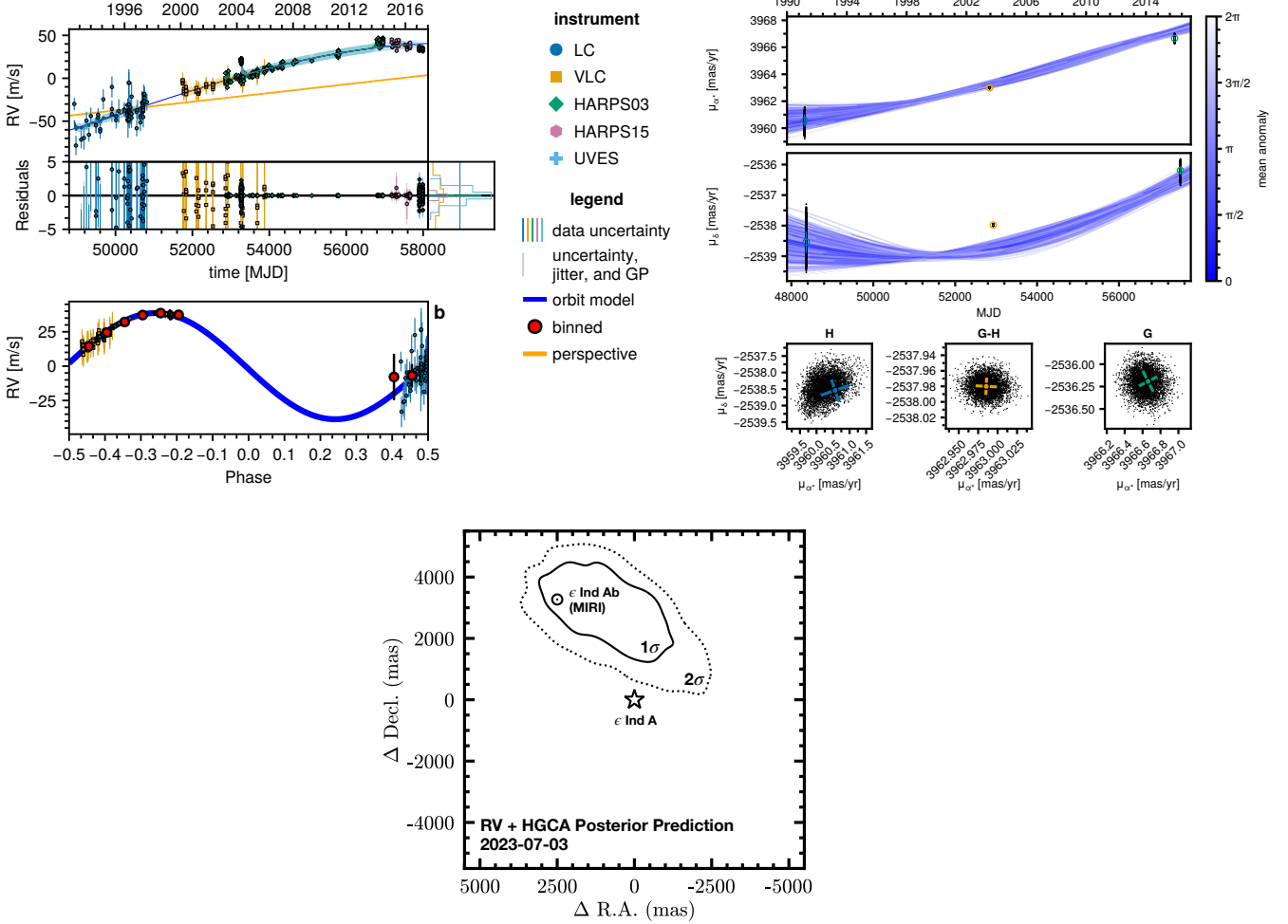


Figure B1. *Top:* Best-fit circular orbit for RV + HGCA model using datasets prior to the JWST imaging detection (i.e., using the exact datasets from F. Feng et al. 2023). The individual panels are identical in format to those presented in Figure 3. *Bottom:* Predicted position of ϵ Ind Ab for the MIRI imaging discovery epoch (2023-07-03) using the best-fit RV + HGCA circular orbit model. The measured position of ϵ Ind Ab (circle, E. C. Matthews et al. 2024) is consistent with the prediction.

orbit fit, we use the LC, VLC, UVES, HARPS03, and HARPS15 RV time series, similar to F. Feng et al. (2023). The implementation of the joint RV and HGCA orbit model is identical to that described in §3.4. The only change is that we fix the eccentricity to zero (circular orbit). Previous studies have shown that the eccentricity of a planet obtained from RV data can be significantly biased by incorrect modeling of the signal, non-Gaussian or correlated noise sources, and/or the presence of additional planets (e.g., N. C. Hara et al. 2019). The ϵ Ind A RV time series does not sample a full planet orbital period and is composed of data from multiple instruments fit by independent offsets. This makes the data particularly susceptible to eccentricity biases and is the motivation to adopt a circular orbit. Indeed, our best-fit RV + HGCA circular orbit model correctly pre-predicts the position of ϵ Ind Ab at the MIRI discovery imaging epoch (2023-07-23, Figure B1). This orbit fit yields $a = 15.2 \pm 1.9$ au, $i = 112_{-9}^{+13} \circ$, and $M_b = 5.0_{-1.4}^{+1.7} M_{\text{Jup}}$, consistent within 1σ – 2σ with our complete relative astrometry + HGCA + RV orbit model. The lesson with ϵ Ind Ab is to exercise caution when applying eccentric orbit models to RV and HGCA data. Using the Bayes Factor to statistically evaluate the significance of eccentric solutions over a circular orbit and performing leave-one-out cross validation are example strategies to mitigate biases in data modeling (see application to ϵ Eridani b in W. Thompson et al. 2025).

C. ORBIT POSTERiors

Table C2 presents the 68% confidence interval and Table C3 presents the 75% highest density interval for all orbital parameters, computed from their respective posterior distributions, for all (converged) orbit models in §3.5.

Table C2. Posterior 68% Credible Intervals

Parameter (Unit)	RA*	RA + HGCA	RA + RV	RA + HGCA + RV	(No NIRCcam)	RA + HGCA + RV	(No GP and No UVES)	A + HGCA + RV	(Unif. Pri.)	RA + HGCA + RV	(Fiducial Model)
M_A (M_\odot)	$0.80^{+0.02}_{-0.02}$	$0.80^{+0.02}_{-0.02}$	$0.80^{+0.02}_{-0.02}$	$0.79^{+0.02}_{-0.02}$	$0.79^{+0.02}_{-0.02}$	$0.79^{+0.02}_{-0.02}$	$0.79^{+0.02}_{-0.02}$	$0.79^{+0.02}_{-0.02}$	$0.79^{+0.02}_{-0.02}$	$0.79^{+0.02}_{-0.02}$	$0.80^{+0.02}_{-0.02}$
M_b (M_{Jup})	...	$5.73^{+0.74}_{-0.60}$	$10.76^{+5.63}_{-5.21}$	$6.10^{+0.55}_{-0.49}$	$6.10^{+0.55}_{-0.49}$	$8.76^{+1.47}_{-1.87}$	$8.76^{+1.47}_{-1.87}$	$7.71^{+1.22}_{-0.94}$	$7.71^{+1.22}_{-0.94}$	$6.50^{+0.72}_{-0.59}$	$6.50^{+0.72}_{-0.59}$
ϖ (mas)	$274.85^{+0.10}_{-0.10}$	$274.85^{+0.09}_{-0.09}$	$274.84^{+0.10}_{-0.10}$	$274.84^{+0.10}_{-0.10}$	$274.84^{+0.10}_{-0.10}$	$274.84^{+0.10}_{-0.10}$	$274.84^{+0.10}_{-0.10}$	$274.85^{+0.10}_{-0.09}$	$274.85^{+0.10}_{-0.09}$	$274.85^{+0.09}_{-0.10}$	$274.85^{+0.09}_{-0.10}$
μ_{α^*} (mas/yr)	$3966.66^{+0.68}_{-0.68}$	$3966.67^{+0.11}_{-0.13}$	$3966.66^{+0.68}_{-0.69}$	$3966.77^{+0.23}_{-0.27}$	$3966.77^{+0.23}_{-0.27}$	$3966.27^{+0.15}_{-0.35}$	$3966.27^{+0.15}_{-0.35}$	$3966.40^{+0.19}_{-0.26}$	$3966.40^{+0.19}_{-0.26}$	$3966.46^{+0.16}_{-0.24}$	$3966.46^{+0.16}_{-0.24}$
μ_δ (mas/yr)	$-2536.20^{+0.68}_{-0.68}$	$-2536.32^{+0.15}_{-0.14}$	$-2536.18^{+0.68}_{-0.68}$	$-2536.07^{+0.22}_{-0.21}$	$-2536.07^{+0.22}_{-0.21}$	$-2536.14^{+0.15}_{-0.23}$	$-2536.14^{+0.15}_{-0.23}$	$-2536.20^{+0.19}_{-0.23}$	$-2536.20^{+0.19}_{-0.23}$	$-2536.34^{+0.24}_{-0.22}$	$-2536.34^{+0.24}_{-0.22}$
γ_* (m/s)	$-40022.29^{+931.80}_{-925.07}$	$-40230.62^{+929.20}_{-908.51}$	$-40033.47^{+939.97}_{-934.21}$	$-40002.85^{+931.11}_{-913.51}$	$-40002.85^{+931.11}_{-913.51}$	$-40478.56^{+929.74}_{-851.92}$	$-40478.56^{+929.74}_{-851.92}$	$-40447.97^{+927.88}_{-855.10}$	$-40447.97^{+927.88}_{-855.10}$	$-40430.15^{+934.66}_{-849.73}$	$-40430.15^{+934.66}_{-849.73}$
a (au)	$21.46^{+3.38}_{-3.66}$	$12.79^{+1.35}_{-0.52}$	$22.42^{+2.82}_{-2.95}$	$16.78^{+1.00}_{-0.79}$	$16.78^{+1.00}_{-0.79}$	$14.87^{+2.70}_{-1.23}$	$14.87^{+2.70}_{-1.23}$	$17.78^{+5.41}_{-3.02}$	$17.78^{+5.41}_{-3.02}$	$15.76^{+1.73}_{-1.39}$	$15.76^{+1.73}_{-1.39}$
P^{\dagger} (yrs)	$111.22^{+26.94}_{-26.83}$	$50.88^{+8.12}_{-2.66}$	$118.08^{+22.42}_{-21.98}$	$77.29^{+7.08}_{-5.50}$	$77.29^{+7.08}_{-5.50}$	$64.48^{+18.16}_{-7.87}$	$64.48^{+18.16}_{-7.87}$	$83.85^{+41.12}_{-20.50}$	$83.85^{+41.12}_{-20.50}$	$69.67^{+12.01}_{-9.04}$	$69.67^{+12.01}_{-9.04}$
e	$0.14^{+0.14}_{-0.11}$	$0.45^{+0.08}_{-0.12}$	$0.11^{+0.13}_{-0.09}$	$0.04^{+0.06}_{-0.03}$	$0.04^{+0.06}_{-0.03}$	$0.56^{+0.06}_{-0.27}$	$0.56^{+0.06}_{-0.27}$	$0.30^{+0.13}_{-0.10}$	$0.30^{+0.13}_{-0.10}$	$0.25^{+0.09}_{-0.09}$	$0.25^{+0.09}_{-0.09}$
i (deg)	$98.46^{+2.17}_{-1.62}$	$103.56^{+1.97}_{-1.86}$	$98.23^{+1.85}_{-1.38}$	$105.50^{+3.27}_{-3.00}$	$105.50^{+3.27}_{-3.00}$	$105.20^{+2.51}_{-3.30}$	$105.20^{+2.51}_{-3.30}$	$101.75^{+2.06}_{-1.83}$	$101.75^{+2.06}_{-1.83}$	$102.18^{+1.72}_{-1.67}$	$102.18^{+1.72}_{-1.67}$
ω (deg)	$1.06^{+163.01}_{-169.83}$	$2.62^{+166.54}_{-25.67}$	$7.32^{+19.81}_{-16.80}$	$16.42^{+40.3}_{-39.17}$	$16.42^{+40.3}_{-39.17}$	$-51.08^{+42.49}_{-10.73}$	$-51.08^{+42.49}_{-10.73}$	$-71.12^{+28.45}_{-50.68}$	$-71.12^{+28.45}_{-50.68}$	$-28.13^{+15.32}_{-17.02}$	$-28.13^{+15.32}_{-17.02}$
Ω (deg)	$51.61^{+176.69}_{-5.67}$	$48.05^{+176.68}_{-5.34}$	$227.62^{+2.39}_{-2.22}$	$226.58^{+3.86}_{-2.67}$	$226.58^{+3.86}_{-2.67}$	$217.98^{+8.83}_{-1.02}$	$217.98^{+8.83}_{-1.02}$	$222.87^{+2.33}_{-1.93}$	$222.87^{+2.33}_{-1.93}$	$224.46^{+2.36}_{-2.12}$	$224.46^{+2.36}_{-2.12}$
t_p^{\dagger} (MJD)	$34483.94^{+5338.17}_{-7817.37}$	$47028.14^{+694.17}_{-2352.93}$	$33095.84^{+4928.88}_{-6448.36}$	$44695.08^{+3057.46}_{-3184.01}$	$44695.08^{+3057.46}_{-3184.01}$	$40785.64^{+2525.93}_{-3832.55}$	$40785.64^{+2525.93}_{-3832.55}$	$36772.43^{+7009.51}_{-13211.06}$	$36772.43^{+7009.51}_{-13211.06}$	$41420.26^{+2675.44}_{-3216.73}$	$41420.26^{+2675.44}_{-3216.73}$
B (m/s)	$26.09^{+5.99}_{-4.34}$	$25.20^{+5.69}_{-4.22}$	$25.20^{+5.69}_{-4.22}$	$25.38^{+5.72}_{-4.20}$	$25.38^{+5.72}_{-4.20}$	$25.83^{+5.93}_{-4.36}$	$25.83^{+5.93}_{-4.36}$
C	$1.37^{+3.55}_{-1.03}$	$1.35^{+3.60}_{-1.02}$	$1.35^{+3.60}_{-1.02}$	$1.29^{+3.53}_{-0.98}$	$1.29^{+3.53}_{-0.98}$	$1.37^{+3.69}_{-1.02}$	$1.37^{+3.69}_{-1.02}$
L (days)	$35.17^{+12.42}_{-10.33}$	$33.46^{+12.09}_{-10.34}$	$33.46^{+12.09}_{-10.34}$	$33.70^{+12.08}_{-10.24}$	$33.70^{+12.08}_{-10.24}$	$34.52^{+12.65}_{-10.45}$	$34.52^{+12.65}_{-10.45}$
P_{rot} (days)	$18.33^{+0.86}_{-1.15}$	$18.30^{+0.89}_{-1.22}$	$18.30^{+0.89}_{-1.22}$	$18.33^{+0.89}_{-1.19}$	$18.33^{+0.89}_{-1.19}$	$18.33^{+0.88}_{-1.19}$	$18.33^{+0.88}_{-1.19}$
m (m/s/yr)	$0.01^{+0.00}_{-0.00}$	$0.00^{+0.00}_{-0.00}$	$0.00^{+0.00}_{-0.00}$	$0.00^{+0.01}_{-0.00}$	$0.00^{+0.01}_{-0.00}$	$0.00^{+0.00}_{-0.00}$	$0.00^{+0.00}_{-0.00}$	$0.00^{+0.00}_{-0.00}$	$0.00^{+0.00}_{-0.00}$
γ_{LC} (m/s)	$-21.06^{+30.41}_{-31.19}$	$37.83^{+9.50}_{-11.04}$	$37.83^{+9.50}_{-11.04}$	$28.34^{+8.94}_{-18.38}$	$28.34^{+8.94}_{-18.38}$	$19.02^{+14.73}_{-15.73}$	$19.02^{+14.73}_{-15.73}$	$27.69^{+9.57}_{-10.98}$	$27.69^{+9.57}_{-10.98}$
γ_{VLC} (m/s)	$-14.10^{+30.02}_{-29.09}$	$25.89^{+5.63}_{-6.53}$	$25.89^{+5.63}_{-6.53}$	$22.05^{+7.72}_{-11.43}$	$22.05^{+7.72}_{-11.43}$	$14.31^{+10.86}_{-12.99}$	$14.31^{+10.86}_{-12.99}$	$21.16^{+6.28}_{-7.29}$	$21.16^{+6.28}_{-7.29}$
γ_{HARPS03} (m/s)	$-25.33^{+27.90}_{-26.51}$	$-0.40^{+3.07}_{-3.32}$	$-0.40^{+3.07}_{-3.32}$	$-1.94^{+7.20}_{-7.87}$	$-1.94^{+7.20}_{-7.87}$	$-9.30^{+9.71}_{-12.18}$	$-9.30^{+9.71}_{-12.18}$	$-1.07^{+5.14}_{-5.27}$	$-1.07^{+5.14}_{-5.27}$
γ_{HARPS15} (m/s)	$1.00^{+23.29}_{-22.03}$	$7.84^{+4.90}_{-5.45}$	$7.84^{+4.90}_{-5.45}$	$2.89^{+11.01}_{-11.79}$	$2.89^{+11.01}_{-11.79}$	$-1.46^{+9.44}_{-13.81}$	$-1.46^{+9.44}_{-13.81}$	$10.68^{+5.15}_{-5.64}$	$10.68^{+5.15}_{-5.64}$
γ_{HARPS20} (m/s)	$19.42^{+18.53}_{-17.65}$	$19.07^{+6.33}_{-7.03}$	$19.07^{+6.33}_{-7.03}$	$3.46^{+22.88}_{-13.50}$	$3.46^{+22.88}_{-13.50}$	$6.98^{+10.36}_{-14.47}$	$6.98^{+10.36}_{-14.47}$	$21.70^{+6.19}_{-7.86}$	$21.70^{+6.19}_{-7.86}$
γ_{ESPR18} (m/s)	$2.74^{+21.27}_{-19.66}$	$5.54^{+5.98}_{-6.71}$	$5.54^{+5.98}_{-6.71}$	$-4.62^{+16.87}_{-12.75}$	$-4.62^{+16.87}_{-12.75}$	$-5.52^{+10.25}_{-14.32}$	$-5.52^{+10.25}_{-14.32}$	$8.32^{+5.84}_{-6.99}$	$8.32^{+5.84}_{-6.99}$
γ_{ESPR19} (m/s)	$8.70^{+19.05}_{-18.18}$	$8.82^{+5.97}_{-6.74}$	$8.82^{+5.97}_{-6.74}$	$-4.63^{+21.41}_{-13.31}$	$-4.63^{+21.41}_{-13.31}$	$-2.86^{+10.05}_{-14.52}$	$-2.86^{+10.05}_{-14.52}$	$11.67^{+5.63}_{-7.37}$	$11.67^{+5.63}_{-7.37}$
γ_{UVES} (m/s)	$-48.84^{+26.26}_{-24.88}$	$-26.46^{+4.25}_{-4.24}$	$-26.46^{+4.25}_{-4.24}$	$-36.87^{+10.02}_{-12.94}$	$-36.87^{+10.02}_{-12.94}$	$-27.38^{+5.88}_{-5.91}$	$-27.38^{+5.88}_{-5.91}$
σ_{LC} (m/s)	$0.17^{+1.08}_{-0.15}$	$0.17^{+1.10}_{-0.15}$	$0.17^{+1.10}_{-0.15}$	$2.28^{+3.25}_{-2.21}$	$2.28^{+3.25}_{-2.21}$	$0.17^{+1.03}_{-0.15}$	$0.17^{+1.03}_{-0.15}$	$0.18^{+1.11}_{-0.15}$	$0.18^{+1.11}_{-0.15}$
σ_{VLC} (m/s)	$0.12^{+0.55}_{-0.09}$	$0.12^{+0.54}_{-0.09}$	$0.12^{+0.54}_{-0.09}$	$0.12^{+0.61}_{-0.10}$	$0.12^{+0.61}_{-0.10}$	$0.12^{+0.55}_{-0.10}$	$0.12^{+0.55}_{-0.10}$	$0.12^{+0.55}_{-0.10}$	$0.12^{+0.55}_{-0.10}$
σ_{HARPS03} (m/s)	$0.05^{+0.14}_{-0.04}$	$0.05^{+0.14}_{-0.04}$	$0.05^{+0.14}_{-0.04}$	$3.29^{+0.24}_{-0.21}$	$3.29^{+0.24}_{-0.21}$	$0.05^{+0.13}_{-0.04}$	$0.05^{+0.13}_{-0.04}$	$0.05^{+0.14}_{-0.04}$	$0.05^{+0.14}_{-0.04}$
σ_{HARPS15} (m/s)	$0.08^{+0.30}_{-0.06}$	$0.08^{+0.30}_{-0.06}$	$0.08^{+0.30}_{-0.06}$	$3.89^{+0.52}_{-0.43}$	$3.89^{+0.52}_{-0.43}$	$0.08^{+0.30}_{-0.06}$	$0.08^{+0.30}_{-0.06}$	$0.08^{+0.30}_{-0.06}$	$0.08^{+0.30}_{-0.06}$
σ_{HARPS20} (m/s)	$2.41^{+0.37}_{-0.32}$	$2.41^{+0.38}_{-0.32}$	$2.41^{+0.38}_{-0.32}$	$3.33^{+0.37}_{-0.32}$	$3.33^{+0.37}_{-0.32}$	$2.41^{+0.37}_{-0.32}$	$2.41^{+0.37}_{-0.32}$	$2.41^{+0.37}_{-0.32}$	$2.41^{+0.37}_{-0.32}$
σ_{ESPR18} (m/s)	$0.15^{+0.04}_{-0.04}$	$0.14^{+0.04}_{-0.04}$	$0.14^{+0.04}_{-0.04}$	$2.16^{+0.24}_{-0.20}$	$2.16^{+0.24}_{-0.20}$	$0.15^{+0.04}_{-0.04}$	$0.15^{+0.04}_{-0.04}$	$0.15^{+0.04}_{-0.04}$	$0.15^{+0.04}_{-0.04}$
σ_{ESPR19} (m/s)	$0.08^{+0.03}_{-0.04}$	$0.08^{+0.03}_{-0.04}$	$0.08^{+0.03}_{-0.04}$	$1.36^{+0.13}_{-0.11}$	$1.36^{+0.13}_{-0.11}$	$0.08^{+0.03}_{-0.04}$	$0.08^{+0.03}_{-0.04}$	$0.08^{+0.03}_{-0.04}$	$0.08^{+0.03}_{-0.04}$
σ_{UVES} (m/s)	$0.57^{+0.09}_{-0.09}$	$0.57^{+0.09}_{-0.09}$	$0.57^{+0.09}_{-0.09}$	$0.57^{+0.09}_{-0.09}$	$0.57^{+0.09}_{-0.09}$	$0.57^{+0.09}_{-0.09}$	$0.57^{+0.09}_{-0.09}$

* Relative astrometry only constrains the total system mass.

† Derived parameter.

Table C3. Posterior 75% Highest Density Intervals

Parameter (Unit)	RA*	RA + HGCA	RA + RV	RA + HGCA + RV	(No NIRCAM)	(No GP and No UVES)	RA + HGCA + RV	(Unif. Pri.)	RA + HGCA + RV	(Fiducial Model)
M_A (M_\odot)	[0.77, 0.82]	[0.77, 0.82]	[0.77, 0.83]	[0.76, 0.81]	[0.76, 0.81]	[0.76, 0.81]	[0.76, 0.82]	[0.76, 0.82]	[0.77, 0.83]	
M_b (M_{Jup})	...	[4.91, 6.42]	[5.13, 17.37]	[5.47, 6.67]	[6.74, 10.52]	[6.74, 10.52]	[6.44, 8.89]	[6.44, 8.89]	[5.73, 7.22]	
ϖ (mas)	[274.73, 274.95]	[274.73, 274.95]	[274.74, 274.95]	$274.84^{+0.10}_{-0.10}$	[274.73, 274.95]	[274.73, 274.95]	[274.74, 274.95]	[274.74, 274.95]	[274.74, 274.96]	
μ_{α^*} (mas/yr)	[3965.76, 3967.25]	[3966.55, 3966.82]	[3966.12, 3967.62]	[274.74, 274.96]	[3966.06, 3966.52]	[3966.06, 3966.52]	[3966.16, 3966.66]	[3966.16, 3966.66]	[3966.24, 3966.69]	
μ_δ (mas/yr)	[-2537.06, -2535.56]	[-2536.48, -2536.15]	[-2536.70, -2535.21]	[-2536.32, -2535.83]	[-2536.32, -2535.87]	[-2536.32, -2535.87]	[-2536.43, -2535.95]	[-2536.43, -2535.95]	[-2536.56, -2536.09]	
γ_* (m/s)	[-41085.58, -38958.21]	[-41323.37, -39218.36]	[-41104.65, -38953.95]	[-41029.87, -38919.29]	[-41592.59, -39579.20]	[-41592.59, -39579.20]	[-41557.32, -39543.90]	[-41557.32, -39543.90]	[-41557.45, -39532.64]	
a (au)	[17.27, 25.40]	[11.96, 13.74]	[19.41, 26.12]	[15.71, 17.81]	[12.86, 16.65]	[12.86, 16.65]	[13.16, 21.24]	[13.16, 21.24]	[13.71, 17.18]	
P^{\dagger} (yrs)	[80.29, 142.42]	[46.20, 55.58]	[93.08, 144.78]	[69.46, 84.15]	[51.83, 76.17]	[51.83, 76.17]	[52.78, 109.20]	[52.78, 109.20]	[56.52, 79.40]	
e	[0.00, 0.23]	[0.35, 0.57]	[0.00, 0.19]	[0.00, 0.08]	[0.48, 0.66]	[0.48, 0.66]	[0.15, 0.40]	[0.15, 0.40]	[0.14, 0.35]	
i (deg)	[96.25, 100.54]	[101.28, 105.67]	[96.21, 99.86]	[101.99, 109.18]	[102.10, 108.78]	[102.10, 108.78]	[99.48, 103.94]	[99.48, 103.94]	[100.21, 104.10]	
ω (deg)	[-179.99, 44.28]	[-16.56, 178.14]	[-17.7, 25.05]	[-28.03, 63.57]	[-70.74, -39.68]	[-70.74, -39.68]	[-109.29, -23.93]	[-109.29, -23.93]	[-45.98, -8.56]	
Ω (deg)	[44.89, 228.20]	[42.30, 225.17]	[224.61, 229.88]	[222.85, 230.05]	[216.01, 219.68]	[216.01, 219.68]	[220.49, 225.45]	[220.49, 225.45]	[221.75, 227.01]	
t_p^{\dagger} (MJD)	[27509.27, 42345.80]	[45718.32, 48183.52]	[26672.87, 39636.71]	[41419.73, 48638.75]	[37372.02, 44393.46]	[37372.02, 44393.46]	[23437.34, 46002.84]	[23437.34, 46002.84]	[38525.03, 45029.21]	
B (m/s)	[19.87, 31.38]	[19.27, 30.32]	[19.40, 30.44]	[19.40, 30.44]	[19.50, 30.95]	
C	[0.00, 3.11]	[0.00, 3.06]	[0.00, 3.04]	[0.00, 3.04]	[0.00, 3.15]	
L (days)	[22.08, 48.33]	[19.71, 45.64]	[20.18, 46.02]	[20.18, 46.02]	[20.59, 47.25]	
P_{rot} (days)	[17.15, 19.57]	[17.03, 19.57]	[17.10, 19.61]	[17.10, 19.61]	[17.13, 19.62]	
m (m/s/yr)	[0.00, 0.01]	[0.00, 0.00]	[0.00, 0.00]	[0.00, 0.00]	[0.00, 0.00]	[0.00, 0.00]	[0.00, 0.00]	
γ_{LC} (m/s)	[-56.59, 12.99]	[26.79, 50.31]	[15.91, 43.37]	[15.91, 43.37]	[3.48, 37.95]	[3.48, 37.95]	[16.61, 40.10]	
γ_{VL} (m/s)	[-49.02, 18.10]	[19.39, 33.29]	[11.65, 32.84]	[11.65, 32.84]	[2.27, 28.88]	[2.27, 28.88]	[14.02, 29.59]	
γ_{HARPS03} (m/s)	[-57.14, 4.57]	[-4.09, 3.30]	[-10.15, 7.22]	[-10.15, 7.22]	[-20.71, 3.86]	[-20.71, 3.86]	[-6.95, 5.04]	
γ_{HARPS15} (m/s)	[-26.10, 25.41]	[1.81, 13.71]	[-8.44, 16.98]	[-8.44, 16.98]	[-14.69, 11.59]	[-14.69, 11.59]	[4.73, 17.29]	
γ_{HARPS20} (m/s)	[-1.52, 39.78]	[11.75, 27.09]	[-20.75, 18.82]	[-20.75, 18.82]	[-6.19, 21.95]	[-6.19, 21.95]	[14.30, 30.27]	
γ_{ESPR18} (m/s)	[-22.06, 24.62]	[-1.76, 12.86]	[-16.56, 16.25]	[-16.56, 16.25]	[-18.95, 8.79]	[-18.95, 8.79]	[1.26, 16.06]	
γ_{ESPR19} (m/s)	[-13.49, 29.06]	[1.83, 16.38]	[-17.26, 20.75]	[-17.26, 20.75]	[-15.62, 12.02]	[-15.62, 12.02]	[4.17, 19.01]	
γ_{UVES} (m/s)	[-80.66, -22.46]	[-31.47, -21.69]	[-49.02, -23.02]	[-49.02, -23.02]	[-33.88, -20.31]	
σ_{LC} (m/s)	[0.01, 0.73]	[0.01, 0.75]	[0.01, 4.72]	[0.01, 4.72]	[0.01, 0.71]	[0.01, 0.71]	[0.01, 0.75]	
σ_{VL} (m/s)	[0.01, 0.41]	[0.01, 0.40]	[0.01, 0.45]	[0.01, 0.45]	[0.01, 0.41]	[0.01, 0.41]	[0.01, 0.41]	
σ_{HARPS03} (m/s)	[0.01, 0.13]	[0.01, 0.13]	[3.03, 3.55]	[3.03, 3.55]	[0.01, 0.13]	[0.01, 0.13]	[0.01, 0.13]	
σ_{HARPS15} (m/s)	[0.01, 0.25]	[0.01, 0.25]	[3.33, 4.41]	[3.33, 4.41]	[0.01, 0.25]	[0.01, 0.25]	[0.01, 0.25]	
σ_{HARPS20} (m/s)	[2.01, 2.79]	[2.01, 2.81]	[2.91, 3.70]	[2.91, 3.70]	[2.00, 2.79]	[2.00, 2.79]	[1.98, 2.77]	
σ_{ESPR18} (m/s)	[0.10, 0.19]	[0.10, 0.19]	[1.89, 2.40]	[1.89, 2.40]	[0.10, 0.19]	[0.10, 0.19]	[0.10, 0.19]	
σ_{ESPR19} (m/s)	[0.04, 0.13]	[0.04, 0.13]	[1.22, 1.50]	[1.22, 1.50]	[0.04, 0.13]	[0.04, 0.13]	[0.04, 0.13]	
σ_{UVES} (m/s)	[0.46, 0.67]	[0.46, 0.67]	[0.46, 0.68]	[0.46, 0.68]	[0.46, 0.67]	

* Relative astrometry only constrains the total system mass.

[†] Derived parameter.

REFERENCES

- Ackerman, A. S., & Marley, M. S. 2001, *The Astrophysical Journal*, 556, 872, doi: [10.1086/321540](https://doi.org/10.1086/321540)
- Antoniadou, K. I., & Libert, A.-S. 2018, *Astronomy and Astrophysics*, 615, A60, doi: [10.1051/0004-6361/201732058](https://doi.org/10.1051/0004-6361/201732058)
- Arregi, J., Rojas, J. F., Sánchez-Lavega, A., & Morgado, A. 2006, *Journal of Geophysical Research: Planets*, 111, doi: [10.1029/2005JE002653](https://doi.org/10.1029/2005JE002653)
- Astropy Collaboration, Robitaille, T. P., Tollerud, E. J., et al. 2013, *âp*, 558, A33, doi: [10.1051/0004-6361/201322068](https://doi.org/10.1051/0004-6361/201322068)
- Astropy Collaboration, Price-Whelan, A. M., Sip\Hocz, B. M., et al. 2018, *\aj*, 156, 123, doi: [10.3847/1538-3881/aabc4f](https://doi.org/10.3847/1538-3881/aabc4f)
- Astropy Collaboration, Price-Whelan, A. M., Lim, P. L., et al. 2022, *\apj*, 935, 167, doi: [10.3847/1538-4357/ac7c74](https://doi.org/10.3847/1538-4357/ac7c74)
- Balmer, W. O., Kammerer, J., Pueyo, L., et al. 2025a, *The Astronomical Journal*, 169, 209, doi: [10.3847/1538-3881/adb1c6](https://doi.org/10.3847/1538-3881/adb1c6)
- Balmer, W. O., Franson, K., Chomez, A., et al. 2025b, *The Astronomical Journal*, 169, 30, doi: [10.3847/1538-3881/ad9265](https://doi.org/10.3847/1538-3881/ad9265)
- Banfield, D., Gierasch, P. J., Bell, M., et al. 1998, *Icarus*, 135, 230, doi: [10.1006/icar.1998.5985](https://doi.org/10.1006/icar.1998.5985)
- Baraffe, I., Chabrier, G., Allard, F., & Hauschildt, P. H. 1998, Evolutionary models for solar metallicity low-mass stars: mass-magnitude relationships and color-magnitude diagrams, arXiv, doi: [10.48550/arXiv.astro-ph/9805009](https://doi.org/10.48550/arXiv.astro-ph/9805009)
- Baraffe, I., Chabrier, G., Barman, T. S., Allard, F., & Hauschildt, P. H. 2003, *Astronomy and Astrophysics*, 402, 701, doi: [10.1051/0004-6361:20030252](https://doi.org/10.1051/0004-6361:20030252)
- Batalha, N., caoimherooney11, & sagnickm. 2020a, natashabatalha/virga: Initial Release, v0.0 Zenodo, doi: [10.5281/zenodo.3759888](https://doi.org/10.5281/zenodo.3759888)
- Batalha, N., Rooney, C., & Mukherjee, S. 2020b, natashabatalha/virga: Initial Release, Zenodo, doi: [10.5281/zenodo.3759888](https://doi.org/10.5281/zenodo.3759888)
- Batalha, N. E., Marley, M. S., Lewis, N. K., & Fortney, J. J. 2019, *The Astrophysical Journal*, 878, 70, doi: [10.3847/1538-4357/ab1b51](https://doi.org/10.3847/1538-4357/ab1b51)
- Batalha, N. E., Rooney, C. M., Visscher, C., et al. 2025, Condensation Clouds in Substellar Atmospheres with Virga, arXiv, doi: [10.48550/arXiv.2508.15102](https://doi.org/10.48550/arXiv.2508.15102)
- Batalha, N. E., Rooney, C. M., Visscher, C., et al. 2025, arXiv e-prints, arXiv:2508.15102, doi: [10.48550/arXiv.2508.15102](https://doi.org/10.48550/arXiv.2508.15102)
- Beichman, C., Sanghi, A., Mawet, D., et al. 2025, *The Astrophysical Journal Letters*, 989, L22, doi: [10.3847/2041-8213/adf53f](https://doi.org/10.3847/2041-8213/adf53f)
- Bezanson, J., Karpinski, S., Shah, V. B., & Edelman, A. 2012, Julia: A Fast Dynamic Language for Technical Computing, arXiv, doi: [10.48550/arXiv.1209.5145](https://doi.org/10.48550/arXiv.1209.5145)
- Bowens-Rubin, R., Mang, J., Limbach, M. A., et al. 2025, NIRCam yells at cloud: JWST MIRI imaging can directly detect exoplanets of the same temperature, mass, age, and orbital separation as Saturn and Jupiter, arXiv, doi: [10.48550/arXiv.2505.15995](https://doi.org/10.48550/arXiv.2505.15995)
- Bowler, B. P. 2016, *Publications of the Astronomical Society of the Pacific*, 128, 102001, doi: [10.1088/1538-3873/128/968/102001](https://doi.org/10.1088/1538-3873/128/968/102001)
- Bowler, B. P., Blunt, S. C., & Nielsen, E. L. 2020, *The Astronomical Journal*, 159, 63, doi: [10.3847/1538-3881/ab5b11](https://doi.org/10.3847/1538-3881/ab5b11)
- Brandt, T. D. 2018, *The Astrophysical Journal Supplement Series*, 239, 31, doi: [10.3847/1538-4365/aaec06](https://doi.org/10.3847/1538-4365/aaec06)
- Brandt, T. D. 2021, *The Astrophysical Journal Supplement Series*, 254, 42, doi: [10.3847/1538-4365/abf93c](https://doi.org/10.3847/1538-4365/abf93c)
- Brandt, T. D. 2024a, *Publications of the Astronomical Society of the Pacific*, 136, 045004, doi: [10.1088/1538-3873/ad38d9](https://doi.org/10.1088/1538-3873/ad38d9)
- Brandt, T. D. 2024b, *Publications of the Astronomical Society of the Pacific*, 136, 045005, doi: [10.1088/1538-3873/ad38da](https://doi.org/10.1088/1538-3873/ad38da)
- Burrows, A., Ibgui, L., & Hubeny, I. 2008, *The Astrophysical Journal*, 682, 1277, doi: [10.1086/589824](https://doi.org/10.1086/589824)
- Burrows, A., & Sharp, C. M. 1999, *The Astrophysical Journal*, 512, 843, doi: [10.1086/306811](https://doi.org/10.1086/306811)
- Burrows, A., Sudarsky, D., & Hubeny, I. 2004, *The Astrophysical Journal*, 609, 407, doi: [10.1086/420974](https://doi.org/10.1086/420974)
- Burrows, A., Sudarsky, D., & Lunine, J. I. 2003, *The Astrophysical Journal*, 596, 587, doi: [10.1086/377709](https://doi.org/10.1086/377709)
- Bushouse, H., Eisenhamer, J., Dencheva, N., et al. 2025, JWST Calibration Pipeline, Zenodo, doi: [10.5281/zenodo.15178003](https://doi.org/10.5281/zenodo.15178003)
- Carlson, B. E., Lacis, A. A., & Rossow, W. B. 1992, *The Astrophysical Journal*, 388, 648, doi: [10.1086/171182](https://doi.org/10.1086/171182)
- Carter, A., Kammerer, J., Leisenring, J., et al. 2025, *Astrophysics Source Code Library*, ascl:2502.014. <https://ui.adsabs.harvard.edu/abs/2025ascl.soft02014C/abstract>
- Carter, A. L., Hinkley, S., Kammerer, J., et al. 2023, *The Astrophysical Journal Letters*
- Chabrier, G., & Baraffe, I. 1997, Structure and evolution of low-mass stars, arXiv, doi: [10.48550/arXiv.astro-ph/9704118](https://doi.org/10.48550/arXiv.astro-ph/9704118)
- Chabrier, G., Baraffe, I., Phillips, M., & Debras, F. 2023, *Astronomy and Astrophysics*, 671, A119, doi: [10.1051/0004-6361/202243832](https://doi.org/10.1051/0004-6361/202243832)

- Chabrier, G., & Debras, F. 2021, *The Astrophysical Journal*, 917, 4, doi: [10.3847/1538-4357/abfc48](https://doi.org/10.3847/1538-4357/abfc48)
- Chabrier, G., Mazevet, S., & Soubiran, F. 2019, *The Astrophysical Journal*, 872, 51, doi: [10.3847/1538-4357/aaf99f](https://doi.org/10.3847/1538-4357/aaf99f)
- Chachan, Y., Fortney, J. J., Ohno, K., Thorngren, D., & Murray-Clay, R. 2025, *The Astrophysical Journal*, 994, 43, doi: [10.3847/1538-4357/ae0cbf](https://doi.org/10.3847/1538-4357/ae0cbf)
- Chen, M., Li, Y., Brandt, T. D., et al. 2022, *The Astronomical Journal*, 163, 288, doi: [10.3847/1538-3881/ac66d2](https://doi.org/10.3847/1538-3881/ac66d2)
- Choquet, E., Perrin, M. D., Chen, C. H., et al. 2016, *The Astrophysical Journal Letters*, 817, L2, doi: [10.3847/2041-8205/817/1/L2](https://doi.org/10.3847/2041-8205/817/1/L2)
- Christiaens, V., Gonzalez, C., Farkas, R., et al. 2023, *The Journal of Open Source Software*, 8, 4774, doi: [10.21105/joss.04774](https://doi.org/10.21105/joss.04774)
- Coulter, D. J., Barnes, J. W., & Fortney, J. J. 2022, *The Astrophysical Journal Supplement Series*, 263, 15, doi: [10.3847/1538-4365/ac886a](https://doi.org/10.3847/1538-4365/ac886a)
- Creevey, O. L., Sordo, R., Pailier, F., et al. 2023, *Astronomy and Astrophysics*, 674, A26, doi: [10.1051/0004-6361/202243688](https://doi.org/10.1051/0004-6361/202243688)
- Crotts, K. A., Carter, A. L., Lawson, K., et al. 2025, *Follow-Up Exploration of the TWA 7 Planet-Disk System with JWST NIRCAM*, arXiv, doi: [10.48550/arXiv.2506.19932](https://doi.org/10.48550/arXiv.2506.19932)
- Currie, T., Biller, B., Lagrange, A., et al. 2023, in *Astronomical Society of the Pacific Conference Series*, Vol. 534, *Protostars and Planets VII*, ed. S. Inutsuka, Y. Aikawa, T. Muto, K. Tomida, & M. Tamura, 799, doi: [10.48550/arXiv.2205.05696](https://doi.org/10.48550/arXiv.2205.05696)
- Do Ó, C. R., O’Neil, K. K., Konopacky, Q. M., et al. 2023, *The Astronomical Journal*, 166, 48, doi: [10.3847/1538-3881/acdc9a](https://doi.org/10.3847/1538-3881/acdc9a)
- Dupuy, T. J., & Liu, M. C. 2017, *The Astrophysical Journal Supplement Series*, 231, 15, doi: [10.3847/1538-4365/aa5e4c](https://doi.org/10.3847/1538-4365/aa5e4c)
- Dupuy, T. J., Liu, M. C., Evans, E. L., et al. 2023, *Monthly Notices of the Royal Astronomical Society*, 519, 1688, doi: [10.1093/mnras/stac3557](https://doi.org/10.1093/mnras/stac3557)
- Endl, M., Kürster, M., Els, S., et al. 2002, *Astronomy and Astrophysics*, 392, 671, doi: [10.1051/0004-6361:20020937](https://doi.org/10.1051/0004-6361:20020937)
- ESA. 1997, *ESA Special Publication*, 1200. <https://ui.adsabs.harvard.edu/abs/1997ESASP1200.....E>
- Fegley, Jr., B., & Prinn, R. G. 1985, *The Astrophysical Journal*, 299, 1067, doi: [10.1086/163775](https://doi.org/10.1086/163775)
- Feinberg, L. D., Sitarski, B. N., McElwain, M. W., et al. 2026, *Habitable Worlds Observatory’s Concept and Technology Maturation: Initial Feasibility and Trade Space Exploration*, arXiv, doi: [10.48550/arXiv.2601.11803](https://doi.org/10.48550/arXiv.2601.11803)
- Feng, F., Anglada-Escudé, G., Tuomi, M., et al. 2019, *Monthly Notices of the Royal Astronomical Society*, 490, 5002, doi: [10.1093/mnras/stz2912](https://doi.org/10.1093/mnras/stz2912)
- Feng, F., Butler, R. P., Vogt, S. S., Holden, B., & Rui, Y. 2023, *Monthly Notices of the Royal Astronomical Society*, 525, 607, doi: [10.1093/mnras/stad2297](https://doi.org/10.1093/mnras/stad2297)
- Feng, F., Xiao, G.-Y., Jones, H. R. A., et al. 2025, *Monthly Notices of the Royal Astronomical Society*, 539, 3180, doi: [10.1093/mnras/staf689](https://doi.org/10.1093/mnras/staf689)
- Filippazzo, J. C., Rice, E. L., Faherty, J., et al. 2015, *The Astrophysical Journal*, 810, 158, doi: [10.1088/0004-637X/810/2/158](https://doi.org/10.1088/0004-637X/810/2/158)
- Foreman-Mackey, D., Agol, E., Ambikasaran, S., & Angus, R. 2017, *The Astronomical Journal*, 154, 220, doi: [10.3847/1538-3881/aa9332](https://doi.org/10.3847/1538-3881/aa9332)
- Foreman-Mackey, D., Hogg, D. W., Lang, D., & Goodman, J. 2013, *Publications of the Astronomical Society of the Pacific*, 125, 306, doi: [10.1086/670067](https://doi.org/10.1086/670067)
- Franson, K., Balmer, W. O., Bowler, B. P., et al. 2024, *The Astrophysical Journal Letters*, 974, L11, doi: [10.3847/2041-8213/ad736a](https://doi.org/10.3847/2041-8213/ad736a)
- Gagliuffi, D. C. B., Balmer, W. O., Pueyo, L., et al. 2025, *JWST Coronagraphic Images of 14 Her c: a Cold Giant Planet in a Dynamically Hot, Multi-planet System*, arXiv, doi: [10.48550/arXiv.2506.09201](https://doi.org/10.48550/arXiv.2506.09201)
- Gaia Collaboration, Vallenari, A., Brown, A. G. A., et al. 2023, *Astronomy and Astrophysics*, 674, A1, doi: [10.1051/0004-6361/202243940](https://doi.org/10.1051/0004-6361/202243940)
- Ge, H., Zhang, X., Fletcher, L. N., et al. 2019, *The Astronomical Journal*, 157, 89, doi: [10.3847/1538-3881/aafba7](https://doi.org/10.3847/1538-3881/aafba7)
- Gelino, C., & Marley, M. 2000, in *From Giant Planets to Cool Stars*, Vol. 212, 322. <https://ui.adsabs.harvard.edu/abs/2000ASPC..212..322G>
- Gelman, A., & Rubin, D. B. 1992, *Statistical Science*, 7, 457, doi: [10.1214/ss/1177011136](https://doi.org/10.1214/ss/1177011136)
- Georgakarakos, N., Eggl, S., & Dobbs-Dixon, I. 2018, *The Astrophysical Journal*, 856, 155, doi: [10.3847/1538-4357/aaaf72](https://doi.org/10.3847/1538-4357/aaaf72)
- Ginsburg, A., Sipőcz, B. M., Brasseur, C. E., et al. 2019, *AJ*, 157, 98, doi: [10.3847/1538-3881/aafc33](https://doi.org/10.3847/1538-3881/aafc33)
- Ginsburg, A., Sipőcz, B., Brasseur, C. E., et al. 2024, *astropy/astroquery: v0.4.7*, Zenodo, doi: [10.5281/zenodo.10799414](https://doi.org/10.5281/zenodo.10799414)

- Girard, J. H., Gennaro, M., Rest, A., et al. 2024, in *Space Telescopes and Instrumentation 2024: Optical, Infrared, and Millimeter Wave*, Vol. 13092 (SPIE), 1309251, doi: [10.1117/12.3020243](https://doi.org/10.1117/12.3020243)
- Gomez Gonzalez, C. A., Wertz, O., Absil, O., et al. 2017, *The Astronomical Journal*, 154, 7, doi: [10.3847/1538-3881/aa73d7](https://doi.org/10.3847/1538-3881/aa73d7)
- Gommers, R., Virtanen, P., Burovski, E., et al. 2023, *scipy/scipy: SciPy 1.11.2*, Zenodo, doi: [10.5281/zenodo.8259693](https://doi.org/10.5281/zenodo.8259693)
- Guillot, T., Santos, N. C., Pont, F., et al. 2006, *Astronomy and Astrophysics*, 453, L21, doi: [10.1051/0004-6361:20065476](https://doi.org/10.1051/0004-6361:20065476)
- Hara, N. C., Boué, G., Laskar, J., Delisle, J.-B., & Unger, N. 2019, *Monthly Notices of the Royal Astronomical Society*, 489, 738, doi: [10.1093/mnras/stz1849](https://doi.org/10.1093/mnras/stz1849)
- Harris, C. R., Millman, K. J., Walt, S. J. v. d., et al. 2020, *Nature*, 585, 357, doi: [10.1038/s41586-020-2649-2](https://doi.org/10.1038/s41586-020-2649-2)
- Hasegawa, Y., Bryden, G., Ikoma, M., Vasisht, G., & Swain, M. 2018, *The Astrophysical Journal*, 865, 32, doi: [10.3847/1538-4357/aad912](https://doi.org/10.3847/1538-4357/aad912)
- Hubeny, I., & Lanz, T. 1995, *The Astrophysical Journal*, 439, 875, doi: [10.1086/175226](https://doi.org/10.1086/175226)
- Hunter, J. D. 2007, *Computing in Science & Engineering*, 9, 90, doi: [10.1109/MCSE.2007.55](https://doi.org/10.1109/MCSE.2007.55)
- Hurt, S. A., Liu, M. C., Zhang, Z., et al. 2024, *The Astrophysical Journal*, 961, 121, doi: [10.3847/1538-4357/ad0b12](https://doi.org/10.3847/1538-4357/ad0b12)
- Ikoma, M., & Kobayashi, H. 2025, *Annual Review of Astronomy and Astrophysics*, 63, 217, doi: [10.1146/annurev-astro-052722-094843](https://doi.org/10.1146/annurev-astro-052722-094843)
- Janson, M., Apai, D., Zechmeister, M., et al. 2009, *Monthly Notices of the Royal Astronomical Society*, 399, 377, doi: [10.1111/j.1365-2966.2009.15285.x](https://doi.org/10.1111/j.1365-2966.2009.15285.x)
- Kammerer, J., Girard, J., Carter, A. L., et al. 2022, in *Space Telescopes and Instrumentation 2022: Optical, Infrared, and Millimeter Wave*, Vol. 12180 (SPIE), 1369–1388, doi: [10.1117/12.2628865](https://doi.org/10.1117/12.2628865)
- Kasper, M., Arsenault, R., Käuffl, H.-U., et al. 2017, *The Messenger*, 169, 16, doi: [10.18727/0722-6691/5033](https://doi.org/10.18727/0722-6691/5033)
- Kasper, M., Arsenault, R., Käuffl, U., et al. 2019, *The Messenger*, 178, 5, doi: [10.18727/0722-6691/5163](https://doi.org/10.18727/0722-6691/5163)
- Kong, Z., Johansen, A., Lambrechts, M., Jiang, J. H., & Zhu, Z.-H. 2024, *Astronomy & Astrophysics*, 687, A121, doi: [10.1051/0004-6361/202349043](https://doi.org/10.1051/0004-6361/202349043)
- Kühnle, H., Patapis, P., Mollière, P., et al. 2025, *Astronomy & Astrophysics*, 695, A224, doi: [10.1051/0004-6361/202452547](https://doi.org/10.1051/0004-6361/202452547)
- Lacy, B., & Burrows, A. 2023, *The Astrophysical Journal*, 950, 8, doi: [10.3847/1538-4357/acc8cb](https://doi.org/10.3847/1538-4357/acc8cb)
- Lagrange, A. M., Bonnefoy, M., Chauvin, G., et al. 2010, *Science*, 329, 57, doi: [10.1126/science.1187187](https://doi.org/10.1126/science.1187187)
- Lagrange, A.-M., Wilkinson, C., Mâlin, M., et al. 2025, *Nature*, 642, 905, doi: [10.1038/s41586-025-09150-4](https://doi.org/10.1038/s41586-025-09150-4)
- Leggett, S. K., Saumon, D., Marley, M. S., et al. 2007, *The Astrophysical Journal*, 655, 1079, doi: [10.1086/510014](https://doi.org/10.1086/510014)
- Leggett, S. K., & Tremblin, P. 2023, *The Astrophysical Journal*, 959, 86, doi: [10.3847/1538-4357/acfdad](https://doi.org/10.3847/1538-4357/acfdad)
- Leggett, S. K., & Tremblin, P. 2024a, *Research Notes of the AAS*, 8, 13, doi: [10.3847/2515-5172/ad1b61](https://doi.org/10.3847/2515-5172/ad1b61)
- Leggett, S. K., & Tremblin, P. 2024b, *Redshifting the Study of Cold Brown Dwarfs and Exoplanets: the Mid-Infrared Wavelength Region as an Indicator of Surface Gravity and Mass*, arXiv. <http://arxiv.org/abs/2411.03549>
- Leggett, S. K., Tremblin, P., Phillips, M. W., et al. 2021, *The Astrophysical Journal*, 918, 11, doi: [10.3847/1538-4357/ac0cfe](https://doi.org/10.3847/1538-4357/ac0cfe)
- Leisenring, J. 2025, *WebbPSF Extensions*, Zenodo, doi: [10.5281/zenodo.15086592](https://doi.org/10.5281/zenodo.15086592)
- Li, Y., Liu, M. C., Dupuy, T. J., et al. 2025, *A Test of Substellar Evolutionary Models with High-Precision Ages from Asteroseismology and Gyrochronology for the Benchmark System HR 7672AB*, arXiv, doi: [10.48550/arXiv.2512.06083](https://doi.org/10.48550/arXiv.2512.06083)
- Limbach, M. A., Vanderburg, A., Venner, A., et al. 2024, *The Astrophysical Journal Letters*, 973, L11, doi: [10.3847/2041-8213/ad74ed](https://doi.org/10.3847/2041-8213/ad74ed)
- Limbach, M. A., Vanderburg, A., MacDonald, R. J., et al. 2025, *The Astrophysical Journal Letters*, 984, L28, doi: [10.3847/2041-8213/adc9ad](https://doi.org/10.3847/2041-8213/adc9ad)
- Lindgren, L., Klioner, S. A., Hernández, J., et al. 2021, *Astronomy and Astrophysics*, 649, A2, doi: [10.1051/0004-6361/202039709](https://doi.org/10.1051/0004-6361/202039709)
- Liu, M. C. 2004, *Science*, 305, 1442, doi: [10.1126/science.1102929](https://doi.org/10.1126/science.1102929)
- Lodders, K., & Fegley, B. 2002, *Icarus*, 155, 393, doi: [10.1006/icar.2001.6740](https://doi.org/10.1006/icar.2001.6740)
- Luhman, K. L. 2014, *The Astrophysical Journal*, 786, L18, doi: [10.1088/2041-8205/786/2/L18](https://doi.org/10.1088/2041-8205/786/2/L18)
- Luhman, K. L., Tremblin, P., Alves de Oliveira, C., et al. 2023, *The Astronomical Journal*, 167, 5, doi: [10.3847/1538-3881/ad0b72](https://doi.org/10.3847/1538-3881/ad0b72)
- Lundkvist, M. S., Kjeldsen, H., Bedding, T. R., et al. 2024, *The Astrophysical Journal*, 964, 110, doi: [10.3847/1538-4357/ad25f2](https://doi.org/10.3847/1538-4357/ad25f2)
- Madhusudhan, N. 2019, *Annual Review of Astronomy and Astrophysics*, 57, 617, doi: [10.1146/annurev-astro-081817-051846](https://doi.org/10.1146/annurev-astro-081817-051846)

- Madurowicz, A., Ruffio, J.-B., Macintosh, B., et al. 2025, Direct Spectroscopy of 51 Eridani b with JWST NIRSpec, doi: [10.3847/1538-3881/ae1028](https://doi.org/10.3847/1538-3881/ae1028)
- Mahalanobis, P. C. 1930, *J. Asiat. Soc. Bengal*, 26, 541
- Mamajek, E., & Stapelfeldt, K. 2024, NASA Exoplanet Exploration Program (ExEP) Mission Star List for the Habitable Worlds Observatory (2023), arXiv, doi: [10.48550/arXiv.2402.12414](https://doi.org/10.48550/arXiv.2402.12414)
- Mamajek, E. E., Prsa, A., Torres, G., et al. 2015, IAU 2015 Resolution B3 on Recommended Nominal Conversion Constants for Selected Solar and Planetary Properties, arXiv, doi: [10.48550/arXiv.1510.07674](https://doi.org/10.48550/arXiv.1510.07674)
- Mang, J., Gao, P., Hood, C. E., et al. 2022, *The Astrophysical Journal*, 927, 184, doi: [10.3847/1538-4357/ac51d3](https://doi.org/10.3847/1538-4357/ac51d3)
- Mang, J., Morley, C. V., Robinson, T. D., & Gao, P. 2024, Microphysical Prescriptions for Parameterized Water Cloud Formation on Ultra-cool Substellar Objects, arXiv, doi: [10.48550/arXiv.2408.08958](https://doi.org/10.48550/arXiv.2408.08958)
- Mang, J., Batalha, N. E., Morley, C. V., et al. 2026, PICASO 4.0: Clouds and Photochemistry in Climate Models of Brown Dwarfs and Exoplanets, arXiv, doi: [10.48550/arXiv.2602.22468](https://doi.org/10.48550/arXiv.2602.22468)
- Marley, M. S., Gelino, C., Stephens, D., Lunine, J. I., & Freedman, R. 1999, *The Astrophysical Journal*, 513, 879, doi: [10.1086/306881](https://doi.org/10.1086/306881)
- Marley, M. S., Saumon, D., Visscher, C., et al. 2021, *The Astrophysical Journal*, 920, 85, doi: [10.3847/1538-4357/ac141d](https://doi.org/10.3847/1538-4357/ac141d)
- Marois, C., Lafrenière, D., Doyon, R., Macintosh, B., & Nadeau, D. 2006, *The Astrophysical Journal*, 641, 556, doi: [10.1086/500401](https://doi.org/10.1086/500401)
- Marois, C., Macintosh, B., & Véran, J.-P. 2010, 7736, 77361J, doi: [10.1117/12.857225](https://doi.org/10.1117/12.857225)
- Matthews, E. C., Carter, A. L., Pathak, P., et al. 2024, *Nature*, 633, 789, doi: [10.1038/s41586-024-07837-8](https://doi.org/10.1038/s41586-024-07837-8)
- Mawet, D., Milli, J., Wahhaj, Z., et al. 2014, *The Astrophysical Journal*, 792, 97, doi: [10.1088/0004-637X/792/2/97](https://doi.org/10.1088/0004-637X/792/2/97)
- McCaughrean, M. J., Close, L. M., Scholz, R.-D., et al. 2004, *Astronomy and Astrophysics*, 413, 1029, doi: [10.1051/0004-6361/20034292](https://doi.org/10.1051/0004-6361/20034292)
- McKinney, W. 2010, in *Proceedings of the 9th Python in Science Conference*, ed. S. v. d. Walt & J. Millman, 56 – 61, doi: [10.25080/Majora-92bf1922-00a](https://doi.org/10.25080/Majora-92bf1922-00a)
- Meisner, A. M., Leggett, S. K., Logsdon, S. E., et al. 2023, *The Astronomical Journal*, 166, 57, doi: [10.3847/1538-3881/acdb68](https://doi.org/10.3847/1538-3881/acdb68)
- Miles, B. E., Skemer, A. J. I., Morley, C. V., et al. 2020, *The Astronomical Journal*, 160, 63, doi: [10.3847/1538-3881/ab9114](https://doi.org/10.3847/1538-3881/ab9114)
- Miller, N., & Fortney, J. J. 2011, *The Astrophysical Journal*, 736, L29, doi: [10.1088/2041-8205/736/2/L29](https://doi.org/10.1088/2041-8205/736/2/L29)
- Moran, S. E., Lodge, M. G., Batalha, N. E., et al. 2025, *The Astrophysical Journal*, 994, 116, doi: [10.3847/1538-4357/ae0583](https://doi.org/10.3847/1538-4357/ae0583)
- Moran, S. E., Lodge, M. G., Batalha, N. E., et al. 2025, *ApJ*, 994, 116, doi: [10.3847/1538-4357/ae0583](https://doi.org/10.3847/1538-4357/ae0583)
- Morley, C. V., Marley, M. S., Fortney, J. J., & Lupu, R. 2014a, *The Astrophysical Journal*, 789, L14, doi: [10.1088/2041-8205/789/1/L14](https://doi.org/10.1088/2041-8205/789/1/L14)
- Morley, C. V., Marley, M. S., Fortney, J. J., et al. 2014b, *The Astrophysical Journal*, 787, 78, doi: [10.1088/0004-637X/787/1/78](https://doi.org/10.1088/0004-637X/787/1/78)
- Mukherjee, S., Batalha, N. E., Fortney, J. J., & Marley, M. S. 2023, *The Astrophysical Journal*, 942, 71, doi: [10.3847/1538-4357/ac9f48](https://doi.org/10.3847/1538-4357/ac9f48)
- Mukherjee, S., Fortney, J. J., Morley, C. V., et al. 2024, *The Astrophysical Journal*, 963, 73, doi: [10.3847/1538-4357/ad18c2](https://doi.org/10.3847/1538-4357/ad18c2)
- Nagpal, V., Blunt, S., Bowler, B. P., et al. 2023, *The Astronomical Journal*, 165, 32, doi: [10.3847/1538-3881/ac9fd2](https://doi.org/10.3847/1538-3881/ac9fd2)
- Nasedkin, E., Mollière, P., Lacour, S., et al. 2024, *Astronomy and Astrophysics*, 687, A298, doi: [10.1051/0004-6361/202449328](https://doi.org/10.1051/0004-6361/202449328)
- Nelder, J. A., & Mead, R. 1965, *The Computer Journal*, 7, 308, doi: [10.1093/comjnl/7.4.308](https://doi.org/10.1093/comjnl/7.4.308)
- Noble, M., Musielak, Z. E., & Cuntz, M. 2002, *The Astrophysical Journal*, 572, 1024, doi: [10.1086/340430](https://doi.org/10.1086/340430)
- Noll, K. S., Geballe, T. R., & Marley, M. S. 1997, *The Astrophysical Journal*, 489, L87, doi: [10.1086/310954](https://doi.org/10.1086/310954)
- O’Neil, K. K., Martinez, G. D., Hees, A., et al. 2019, *The Astronomical Journal*, 158, 4, doi: [10.3847/1538-3881/ab1d66](https://doi.org/10.3847/1538-3881/ab1d66)
- Pace, G. 2013, *Astronomy and Astrophysics*, 551, L8, doi: [10.1051/0004-6361/201220364](https://doi.org/10.1051/0004-6361/201220364)
- Pathak, P., Roche, D. J. M. P. d. d. l., Kasper, M., et al. 2021, *Astronomy & Astrophysics*, 652, A121, doi: [10.1051/0004-6361/202140529](https://doi.org/10.1051/0004-6361/202140529)
- Pepe, F., Cristiani, S., Rebolo, R., et al. 2021, *Astronomy & Astrophysics*, 645, A96, doi: [10.1051/0004-6361/202038306](https://doi.org/10.1051/0004-6361/202038306)

- Perrin, M. D., Sivaramakrishnan, A., Lajoie, C.-P., et al. 2014, in *Society of Photo-Optical Instrumentation Engineers (SPIE) Conference Series*, Vol. 9143, *Space Telescopes and Instrumentation 2014: Optical, Infrared, and Millimeter Wave*, ed. J. Oschmann, Jacobus M., M. Clampin, G. G. Fazio, & H. A. MacEwen, 91433X, doi: [10.1117/12.2056689](https://doi.org/10.1117/12.2056689)
- Perrin, M. D., Soummer, R., Elliott, E. M., Lallo, M. D., & Sivaramakrishnan, A. 2012, in *Society of Photo-Optical Instrumentation Engineers (SPIE) Conference Series*, Vol. 8442, *Space Telescopes and Instrumentation 2012: Optical, Infrared, and Millimeter Wave*, ed. M. C. Clampin, G. G. Fazio, H. A. MacEwen, & J. Oschmann, Jacobus M., 84423D, doi: [10.1117/12.925230](https://doi.org/10.1117/12.925230)
- Philipot, F., Lagrange, A.-M., Rubini, P., Kiefer, F., & Chomez, A. 2023, *Astronomy and Astrophysics*, 670, A65, doi: [10.1051/0004-6361/202245396](https://doi.org/10.1051/0004-6361/202245396)
- Phillips, M. W., Tremblin, P., Baraffe, I., et al. 2020, *Astronomy and Astrophysics*, 637, A38, doi: [10.1051/0004-6361/201937381](https://doi.org/10.1051/0004-6361/201937381)
- Potekhin, A. Y., & Chabrier, G. 2012, *Astronomy and Astrophysics*, 538, A115, doi: [10.1051/0004-6361/201117938](https://doi.org/10.1051/0004-6361/201117938)
- Pueyo, L. 2016, *The Astrophysical Journal*, 824, 117, doi: [10.3847/0004-637X/824/2/117](https://doi.org/10.3847/0004-637X/824/2/117)
- Rains, A. D., Ireland, M. J., White, T. R., Casagrande, L., & Karovicova, I. 2020, *Monthly Notices of the Royal Astronomical Society*, 493, 2377, doi: [10.1093/mnras/staa282](https://doi.org/10.1093/mnras/staa282)
- Raymond, S. N. 2006, *The Astrophysical Journal*, 643, L131, doi: [10.1086/505596](https://doi.org/10.1086/505596)
- Rigby, J., Perrin, M., McElwain, M., et al. 2023, *Publications of the Astronomical Society of the Pacific*, 135, 048001, doi: [10.1088/1538-3873/acb293](https://doi.org/10.1088/1538-3873/acb293)
- Roettenbacher, R. M., Cabot, S. H. C., Fischer, D. A., et al. 2022, *The Astronomical Journal*, 163, 19, doi: [10.3847/1538-3881/ac3235](https://doi.org/10.3847/1538-3881/ac3235)
- Roos-Serote, M., Atreya, S. K., Wong, M. K., & Drossart, P. 2004, *Planetary and Space Science*, 52, 397, doi: [10.1016/j.pss.2003.06.007](https://doi.org/10.1016/j.pss.2003.06.007)
- Ruffio, J.-B., Xuan, J. W., Chachan, Y., et al. 2026, *Nature Astronomy*, 1, doi: [10.1038/s41550-026-02783-z](https://doi.org/10.1038/s41550-026-02783-z)
- Rustamkulov, Z., Sing, D. K., Mukherjee, S., et al. 2023, *Nature*, 614, 659, doi: [10.1038/s41586-022-05677-y](https://doi.org/10.1038/s41586-022-05677-y)
- Sanghi, A., Zhou, Y., & Bowler, B. P. 2022, *The Astronomical Journal*, 163, 119, doi: [10.3847/1538-3881/ac477e](https://doi.org/10.3847/1538-3881/ac477e)
- Sanghi, A., Liu, M. C., Best, W. M. J., et al. 2023, *The Astrophysical Journal*, 959, 63, doi: [10.3847/1538-4357/acff66](https://doi.org/10.3847/1538-4357/acff66)
- Sanghi, A., Xuan, J. W., Wang, J. J., et al. 2024, *The Astronomical Journal*, 168, 215, doi: [10.3847/1538-3881/ad769f](https://doi.org/10.3847/1538-3881/ad769f)
- Sanghi, A., Beichman, C., Mawet, D., et al. 2025, *The Astrophysical Journal Letters*, 989, L23, doi: [10.3847/2041-8213/adf53e](https://doi.org/10.3847/2041-8213/adf53e)
- Sanghi, A., Mang, J., Llop-Sayson, J., et al. 2026, *Worlds Next Door. III. Indirect Evidence for Enhanced Atmospheric Metallicity and/or the Presence of Water Clouds in the Nearest Jupiter-analog ϵ Eri b*, arXiv, doi: [10.48550/arXiv.2602.23423](https://doi.org/10.48550/arXiv.2602.23423)
- Sato, M., & Hansen, J. E. 1979, *Journal of the Atmospheric Sciences*, 36, 1133, doi: [10.1175/1520-0469\(1979\)036\(1133:JACACS\)2.0.CO;2](https://doi.org/10.1175/1520-0469(1979)036(1133:JACACS)2.0.CO;2)
- Saumon, D., & Marley, M. S. 2008, *The Astrophysical Journal*, 689, 1327, doi: [10.1086/592734](https://doi.org/10.1086/592734)
- Saumon, D., Marley, M. S., Cushing, M. C., et al. 2006, *The Astrophysical Journal*, 647, 552, doi: [10.1086/505419](https://doi.org/10.1086/505419)
- Scholz, R.-D., McCaughrean, M. J., Lodieu, N., & Kuhlbrodt, B. 2003, *Astronomy and Astrophysics*, 398, L29, doi: [10.1051/0004-6361:20021847](https://doi.org/10.1051/0004-6361:20021847)
- Skemer, A. J., Morley, C. V., Allers, K. N., et al. 2016, *The Astrophysical Journal*, 826, L17, doi: [10.3847/2041-8205/826/2/L17](https://doi.org/10.3847/2041-8205/826/2/L17)
- Snellen, I. A. G. 2025, *Annual Review of Astronomy and Astrophysics*, 63, 83, doi: [10.1146/annurev-astro-052622-031342](https://doi.org/10.1146/annurev-astro-052622-031342)
- Soummer, R., Pueyo, L., & Larkin, J. 2012, *The Astrophysical Journal*, 755, L28, doi: [10.1088/2041-8205/755/2/L28](https://doi.org/10.1088/2041-8205/755/2/L28)
- Spiegel, D. S., & Burrows, A. 2012, *The Astrophysical Journal*, 745, 174, doi: [10.1088/0004-637X/745/2/174](https://doi.org/10.1088/0004-637X/745/2/174)
- Sudarsky, D., Burrows, A., & Hubeny, I. 2003, *The Astrophysical Journal*, 588, 1121, doi: [10.1086/374331](https://doi.org/10.1086/374331)
- Sudarsky, D., Burrows, A., Hubeny, I., & Li, A. 2005, *The Astrophysical Journal*, 627, 520, doi: [10.1086/430206](https://doi.org/10.1086/430206)
- Sur, A., Arevalo, R. T., Burrows, A., & Chen, Y.-X. 2025, *Next-Generation Improvements in Giant Exoplanet Evolutionary and Structural Models*, arXiv, doi: [10.48550/arXiv.2510.08681](https://doi.org/10.48550/arXiv.2510.08681)
- Surjanovic, N., Biron-Lattes, M., Tiede, P., et al. 2023, *Pigeons.jl: Distributed Sampling From Intractable Distributions*, arXiv, doi: [10.48550/arXiv.2308.09769](https://doi.org/10.48550/arXiv.2308.09769)
- Surjanovic, N., Syed, S., Bouchard-Côté, A., & Campbell, T. 2022, *Parallel Tempering With a Variational Reference*, arXiv, doi: [10.48550/arXiv.2206.00080](https://doi.org/10.48550/arXiv.2206.00080)
- Syed, S., Bouchard-Côté, A., Deligiannidis, G., & Doucet, A. 2022, *Journal of the Royal Statistical Society Series B: Statistical Methodology*, 84, 321, doi: [10.1111/rssb.12464](https://doi.org/10.1111/rssb.12464)

- team, T. p. d. 2025, pandas-dev/pandas: Pandas, Zenodo, doi: [10.5281/zenodo.15597513](https://doi.org/10.5281/zenodo.15597513)
- Tennyson, J., & Yurchenko, S. N. 2018, *Atoms*, 6, 26, doi: [10.3390/atoms6020026](https://doi.org/10.3390/atoms6020026)
- Thompson, W., Nielsen, E., Ruffio, J.-B., Blunt, S., & Marois, C. 2025, Revised Mass and Orbit of ϵ Eridani b: A 1 Jupiter-Mass Planet on a Near-Circular Orbit, arXiv, doi: [10.48550/arXiv.2502.20561](https://doi.org/10.48550/arXiv.2502.20561)
- Thompson, W., Marois, C., Do Ó, C. R., et al. 2023, *The Astronomical Journal*, 165, 29, doi: [10.3847/1538-3881/aca1af](https://doi.org/10.3847/1538-3881/aca1af)
- Thorngren, D., & Fortney, J. J. 2019, *The Astrophysical Journal*, 874, L31, doi: [10.3847/2041-8213/ab1137](https://doi.org/10.3847/2041-8213/ab1137)
- Thorngren, D. P., Fortney, J. J., Murray-Clay, R. A., & Lopez, E. D. 2016, *The Astrophysical Journal*, 831, 64, doi: [10.3847/0004-637X/831/1/64](https://doi.org/10.3847/0004-637X/831/1/64)
- Torres, C. A. O., Quast, G. R., da Silva, L., et al. 2006, *Astronomy and Astrophysics*, 460, 695, doi: [10.1051/0004-6361/20065602](https://doi.org/10.1051/0004-6361/20065602)
- Trifonov, T., Tal-Or, L., Zechmeister, M., et al. 2020, *Astronomy and Astrophysics*, 636, A74, doi: [10.1051/0004-6361/201936686](https://doi.org/10.1051/0004-6361/201936686)
- van der Walt, S., Schönberger, J. L., Nunez-Iglesias, J., et al. 2014, *PeerJ*, 2, e453, doi: [10.7717/peerj.453](https://doi.org/10.7717/peerj.453)
- van Leeuwen, F. 2007, *Hipparcos, the New Reduction of the Raw Data*, Vol. 350, doi: [10.1007/978-1-4020-6342-8](https://doi.org/10.1007/978-1-4020-6342-8)
- Van Rossum, G., & Drake, F. L. 2009, *Python 3 Reference Manual* (Scotts Valley, CA: CreateSpace)
- Vehtari, A., Gelman, A., Simpson, D., Carpenter, B., & Bürkner, P.-C. 2021, *Bayesian Analysis*, 16, 667, doi: [10.1214/20-BA1221](https://doi.org/10.1214/20-BA1221)
- Virtanen, P., Gommers, R., Oliphant, T. E., et al. 2020, *Nature Methods*, 17, 261, doi: [10.1038/s41592-019-0686-2](https://doi.org/10.1038/s41592-019-0686-2)
- Viswanath, G., Janson, M., Dahlqvist, C.-H., et al. 2021, *Astronomy and Astrophysics*, 651, A89, doi: [10.1051/0004-6361/202140730](https://doi.org/10.1051/0004-6361/202140730)
- Wagner, K., Boehle, A., Pathak, P., et al. 2021, *Nature Communications*, 12, 922, doi: [10.1038/s41467-021-21176-6](https://doi.org/10.1038/s41467-021-21176-6)
- Wang, J. J., Ruffio, J.-B., De Rosa, R. J., et al. 2015, *Astrophysics Source Code Library*, ascl:1506.001. <https://ui.adsabs.harvard.edu/abs/2015ascl.soft06001W/abstract>
- Wang, J. J., Graham, J. R., Pueyo, L., et al. 2016, *The Astronomical Journal*, 152, 97, doi: [10.3847/0004-6256/152/4/97](https://doi.org/10.3847/0004-6256/152/4/97)
- Wogan, N. F., Mang, J., Batalha, N. E., et al. 2025, *Research Notes of the AAS*, 9, 108, doi: [10.3847/2515-5172/add407](https://doi.org/10.3847/2515-5172/add407)
- Xie, C., Choquet, E., Vigan, A., et al. 2022, *Astronomy and Astrophysics*, 666, A32, doi: [10.1051/0004-6361/202243379](https://doi.org/10.1051/0004-6361/202243379)
- Xuan, J. W., Ruffio, J.-B., Chachan, Y., et al. 2026, The compositions of the HR 8799 planets reflect accretion of both solids and metal-enriched gas, arXiv, doi: [10.48550/arXiv.2602.09422](https://doi.org/10.48550/arXiv.2602.09422)
- Xuan, W. J., Mawet, D., Ngo, H., et al. 2018, *The Astronomical Journal*, 156, 156, doi: [10.3847/1538-3881/aadae6](https://doi.org/10.3847/1538-3881/aadae6)
- Zahnle, K., Marley, M. S., Freedman, R. S., Lodders, K., & Fortney, J. J. 2009, *The Astrophysical Journal*, 701, L20, doi: [10.1088/0004-637X/701/1/L20](https://doi.org/10.1088/0004-637X/701/1/L20)
- Zechmeister, M., Kürster, M., Endl, M., et al. 2013, *Astronomy and Astrophysics*, 552, A78, doi: [10.1051/0004-6361/201116551](https://doi.org/10.1051/0004-6361/201116551)
- Zhou, Y., Bowler, B. P., Wagner, K. R., et al. 2021, *The Astronomical Journal*, 161, 244, doi: [10.3847/1538-3881/abeb7a](https://doi.org/10.3847/1538-3881/abeb7a)